Doctor of Philosophy

Tailoring Morphology and Composition of Intermetallic and High Entropy Alloy Nanoparticles for Enhanced Electrocatalysis

The Graduate School of the University of Ulsan
Department of Nano Energy Chemistry
Dian Tri Lestarini

Tailoring Morphology and Composition of Intermetallic and High Entropy Alloy Nanoparticles for Enhanced Electrocatalysis

Supervisor: Professor Jong Wook Hong

A Dissertation

Submitted to
The Graduate School of the University of Ulsan
In partial Fulfillment of the Requirements
for the Degree of

Doctor of Philosophy in Department of Nano Energy Chemistry
by
Dian Tri Lestarini

Department of Nano Energy Chemistry

University of Ulsan, Republic of Korea

August 2024

Tailoring Morphology and Composition of Intermetallic and High Entropy Alloy Nanoparticles for Enhanced Electrocatalysis

This certifies the dissertation of Dian Tri Lestarini is approved.

Committee Chair: Professor Min Hyung Lee (이민형)

Committee Member: Professor Jong Wook Hong (홍종욱)

Committee Member: Professor Jaehoon Jung (정재훈)

Committee Member: Professor Dongho Lee (이동호)

Committee Member: Professor Seok Min Yoon (윤석민)

Department of Nano Energy Chemistry

University of Ulsan, Rep. of Korea

August 2024

Dedication

Dedicated to my beloved parents, my brother, and my husband.

Table of Contents

Abstract

This dissertation focuses on the development of methods to control the morphologies and compositions of Pd-based nanoparticles for their application in electrocatalytic reactions. It explores their synthesis methods, as well as their physical, electronic, and electrochemical properties. The first chapter offers an overview of advancements in renewable energy related to Pd-based catalysts, strategies to enhance the catalytic performance of Pd-based materials, surface modifications of Pd-based catalysts, and research on nanomaterials and their utilization in electrocatalytic applications.

Chapter two describes Pd based bimetallic nanocrystals (NCs) with low-coordinated surface atoms endow a tremendous ability to modify electronic properties and have the synergistic effect to improve electrocatalytic performance. Among various bimetallic NCs with different compositions, intermetallic Pd-Pb NCs can improve the poisoning tolerance of surface-active sites during electrocatalytic reactions. In addition, Pb can provide abundant oxygen-containing species (OH_{ads}) and has the ability to cleavage the C–C bond during electrocatalysis that can hinder the production of CO_{ads} intermediate species, thereby improving ethanol oxidation reaction (EOR) performance. Herein, we report a wet-chemical method for synthesizing highly uniform Pd_3Pb nanobranches (NBs). The growth process of Pd_3Pb NBs was controlled using ascorbic acid as a reductant, oleylamine as a solvent, 1-octadecene as a surfactant, and ammonium bromide as a shape-directing agent. Their unique NB morphology makes them suitable as electrocatalysts, attributed to the effective adsorption of ethanol and $(OH)_{ads}$ and enhanced removal capability of intermediates adsorbed on the active site of Pd_3Pb NBs due to the intermetallic Pd–Pb composition and high density of low-coordinated surface atoms in Pd_3Pb branches that can enhance EOR in alkaline media. The prepared Pd_3Pb NBs exhibited significantly higher mass activity than Pd_3Pb nanocubes and commercial Pd/C catalysts.

Chapter three deeply studies the cost-effective catalysts for the HER by substituting Pt to Ru in Pd-based catalyst. In this study, we investigate the size-dependent catalytic performance of Ru on intermetallic Pd_3Pb NWs for HER, focusing on the role of single atoms, clusters, and nanoparticles. The synthesized Pd_3Pb-Ru_X NWs (X: S, C, and N) exhibit distinct morphologies, with Ru atoms

anchored on the NW surface. Through a facile synthetic method, the incorporation of Ru in various concentrations, producing Ru single atoms, clusters, and nanoparticles on Pd_3Pb NWs. The electrocatalytic HER performance of these catalysts is evaluated, revealing that $Pd_3Pb\text{-}Ru_S$ NWs, with Ru single atom, exhibit superior activity, with a lower overpotential (13 mV) at 10 mA cm^{-2} compared to Pt/C (45 mV) and a lower Tafel slope (31 mV dec^{-1}) than Pt/C (50 mV dec^{-1}). The presence of Ru single atom on Pd_3Pb NWs significantly enhances stability, with $Pd_3Pb\text{-}Ru_S$ NWs displaying minimal potential loss (5 mV) after 10,000 cycles. Detailed characterization elucidates the structural modifications induced by Ru decoration, highlighting the precise control achievable over nanoscale features. XRD, XPS, and XANES reveal the structural alterations and bonding environments resulting from Ru incorporation. Electrochemical impedance spectroscopy demonstrates enhanced charge transfer rates in Ru-decorated Pd_3Pb NWs, contributing to improving HER activity. This study underscores the potential of size-dependent Ru modifications on intermetallic NWs as efficient electrocatalysts for HER, offering insights into catalyst design for sustainable energy applications.

Chapter four focuses on Direct Alcohol Fuel Cells (DAFCs), which present a promising avenue for sustainable energy conversion, with ethanol emerging as a key fuel due to its high energy density and low toxicity. However, challenges persist in developing efficient electrocatalysts for ethanol oxidation, particularly in alkaline media. Intermetallic Pd_3Pb nanocrystals have shown potential as electrocatalysts, with lead (Pb) enhancing catalytic activity. This study explores the impact of boron doping on Pd_3Pb NWs, focusing on strain and ligand effects on ethanol oxidation. Boron incorporation induces tensile strain and alters surface electronic states, affecting the adsorption of reaction intermediates and influencing p-d orbital hybridization. The synthesized $Pd_3Pb\text{-}B$ NWs exhibit enhanced catalytic activity and selectivity for C1 products with a significant decrease in CO poisoning compared to Pd_3Pb nanocubes and Pd/C. Mechanistic insights reveal a downshift in the d-band center, favoring C1 pathway selectivity by more than 50%. The superior performance and stability of $Pd_3Pb\text{-}B$ NWs underscores the potential of tailored strain and ligand effects in designing efficient electrocatalysts for ethanol oxidation in DAFCs and other energy systems.

Chapter five discusses the controlling morphologies of high-entropy alloys (HEAs) for their potential applications in nanotechnology, particularly in catalysis for HER. This chapter explores the synthesis and characterization of PdPtFeCoNi HEA nanostructures, including NSs, NWs, and NPs, using a one-pot synthetic approach. The influence of various chemical reagents on the morphological evolution of these nanostructures is investigated, revealing insights into the tailored synthesis of HEA materials. The electrochemical performance of these nanostructures is evaluated for HER, demonstrating that PdPtFeCoNi HEA NSs and PdPtFeCoNi HEA NWs exhibit superior catalytic activity compared to PdPtFeCoNi HEA NPs, attributed to their increased active surface area, optimized hydrogen adsorption-desorption dynamics, enhanced mass transport, and structural stability. This study underscores the importance of nanoengineering strategies in developing efficient and durable electrocatalysts for sustainable energy applications.

List of Figures and Tables

Chapter 1

Chapter 2

Chapter 3

Chapter 4

Chapter 5

Figure 7. SEM images of PdPtFeCoNi HEA NSs produced in different concentration of D-glucose a) 0, b) 33, c) 66, d) 133, e) 266, and f) 555 mM.

Figure 8. SEM images of PdPtFeCoNi HEA NSs produced in reaction mixture with a) 0, b) 1, c) 3, and d) 5 mM of $Pd(acac)_2$, e) 0, f) 1, g) 3, and h) 5 mM of $Pt(acac)_2$.

Figure 9. SEM images of elemental composition in HEA NSs with a) PdPtFe, b) PdPtCo, c) PdPtNi, d) PdPtFeCo, e) PdPtFeNi, and f) PdPtCoNi.

Figure 10. SEM images of PdPtFeCoNi HEA NWs produced in reaction mixture with a) acetic acid, b) propionic acid, c) hexanoic acid, and similar pH of ~2.07 from different type of acid d) acetic acid, e) propionic acid, and f) hexanoic acid.

Figure 11. SEM images of PdPtFeCoNi HEA NSs produced in reaction mixture with a) 0, b) 211, c) 422, and d) 845 mM of $NaBH_4$, e) 0, f) 134, g) 268, and h) 1340 mM of propionic acid.

Figure 12. SEM images of PdPtFeCoNi HEA NWs produced in different concentration of D-glucose a) 0, b) 33, c) 66, d) 133, e) 266, and f) 555 mM.

Figure 13. a) HER polarization curve of PdPtFeCoNi HEA NSs with different D-glucose concentrations in 1 M KOH, and b) Tafel plots of all catalysts.

Figure 14. a) HER polarization curve of PdPtFeCoNi HEA NWs with different D-glucose concentrations in 1 M KOH, and b) Tafel plots of all catalysts**.**

Figure 15. a) HER polarization curve of all catalysts in 1 M KOH, b) Tafel plots of all catalysts, c) CV of all catalysts, and d) Nyquist plots for various catalysts in 1.0 M KOH at 0.02 V vs RHE.

Figure 16. a-d) HER polarization curve of all catalysts in 1 M KOH at 50 mA cm^{-2} initial and after 10.000 cycles of PdPtFeCoNi HEA NSs, PdPtFeCoNi HEA NWs, PdPtFeCoNi HEA NPs, and Pt/C.

Table 1. Atomic percentage of Pd, Pt, Fe, Co, and Ni elements of PdPtFeCoNi HEA NSs, NWs, and NPs measured by HR-TEM-EDS.

Table 2. Average diameter of PdPtFeCoNi HEA NSs with different concentration of D-glucose.

Table 3. Average diameter of PdPtFeCoNi HEA NWs with different concentration of D-glucose.

Table 4. HER performance of PdPtFeCoNi HEA NSs with different concentration of D-glucose.

Table 5. HER performance of PdPtFeCoNi HEA NWs with different concentration of D-glucose.

Table 5. HER performance of PdPtFeCoNi HEA NWs with different concentration of D-glucose.

Table 6. HER performance of PdPtFeCoNi HEA nanostructures.

Chapter 1. General Introduction

1.1 Advancements in Renewable Energy through Pd-Based Catalysts

Advancing towards sustainable and eco-friendly alternatives that do not rely on fossil fuels and aim to mitigate the greenhouse effect is pivotal in curbing global warming and reducing carbon dioxide emissions.[1-4] For decades, the role of heterogeneous metal catalysts has been foundational in chemical conversions across energy, environmental, fine chemicals, and petrochemical sectors. Among the platinum group metals, palladium (Pd) distinguishes itself with a unique electron configuration of $4d^{10}5s^0$, setting it apart from other metals like Ru, Rh, Os, Ir, and Pt, and showcasing remarkable efficacy in a myriad of reactions.[5-8] The Nobel Prize in Chemistry awarded to Suzuki, Heck, and Negishi in 2010 highlights the significance of Pd catalysts in facilitating C−C coupling reactions in organic synthesis.[9] Beyond this, Pd catalysts have found extensive applications in processes such as petroleum cracking, catalytic combustion of methane, CO oxidation, alcohol oxidation, selective hydrogenation of unsaturated hydrocarbons, and alkane dehydrogenation.[10-11] Furthermore, Pd-based catalysts play a crucial role in environmental protection, assisting in the purification of automobile exhaust and transforming chlorohydrocarbons into less toxic substances through hydrodechlorination. These diverse applications underscore the indispensable role of Pd catalysts in contemporary industrial practices.

Recent advancements in nanomaterial technology have notably integrated palladium (Pd)-based catalysts into renewable energy conversion applications. These applications in water splitting processes, including the hydrogen evolution reaction (HER) and the oxygen evolution reaction (OER), as well as fuel cell operations such as the ethanol oxidation reaction, the oxygen reduction reaction, and the CO_2 reduction reaction.[5,12,13] Pd-based catalysts have attracted attention as heterogeneous catalysts for their straightforward preparation and facile morphology modification, which play a crucial role in enhancing catalytic performance.

Generally, the efficiency of catalytic reactions is governed by the intrinsic activity and the number of active sites. These two critical parameters can be optimized simultaneously to enhance the performance of Pd-based catalysts.[1,14] To increase intrinsic activity, consideration is given to how the surface properties of bimetallic Pd-based catalysts influence the adsorption configurations and strengths of reactant/product molecules, affecting the rate and pathway of catalyzed reactions. There are three effects that are associated with surface properties, such as ligand effect, strain effect, and ensemble effect.[15,16] The ligand effect arises from the electronic modification of the Pd surface by adjacent atoms in bimetallic catalysts, altering the electronic density at the Pd active sites and thus the adsorption strength of reactants and intermediates. The strain effect, induced by lattice mismatches between the Pd and the secondary metal, can cause changes in the surface atomic arrangement, thereby affecting the activation energy of the reaction. The ensemble effect refers to the spatial arrangement and size of the Pd clusters on the surface, which can dictate the types of chemical reactions that the surface catalyzes effectively, by providing specific active site configurations needed for different reactions.

Another approach is to increase the number of active sites, which can be achieved by modifying the morphology of Pd-based catalysts, enhancing the surface-to-bulk ratio, and reducing the size of nanoparticles. This adjustment in morphology not only increases the number of accessible active sites but also can introduce a variety of surface structures conducive to specific reactions. Together, these strategies including the understanding and utilization of ligand, strain, and ensemble effects form a comprehensive approach to enhancing the catalytic activity and selectivity of Pd-based catalysts for a wide range of applications in renewable energy conversion.

1.2 Nanoengineering Strategies for Enhanced Catalytic Performance of Pd-Based Materials

In recent years, the demand for nanotechnology has surged across various applications, particularly in the development of non-fossil fuel resources such as solar, wind, geothermal energy, and fuel cells. Metal nanoparticles play a crucial role in advancing heterogeneous catalysts and have garnered significant attention, especially those with precise structures, due to their superior electrocatalytic performance. The activity and selectivity of these catalysts are crucially dependent on the atomic arrangement at their surfaces. However, challenges such as the broad size distribution and lack of detailed structural characterization have hindered understanding of their structure-dependent catalytic activity and selectivity. Consequently, adopting a shape-control strategy to synthesize metal nanoparticles has become crucial to improve their intrinsic properties and enhance their catalytic performance.[17-20]

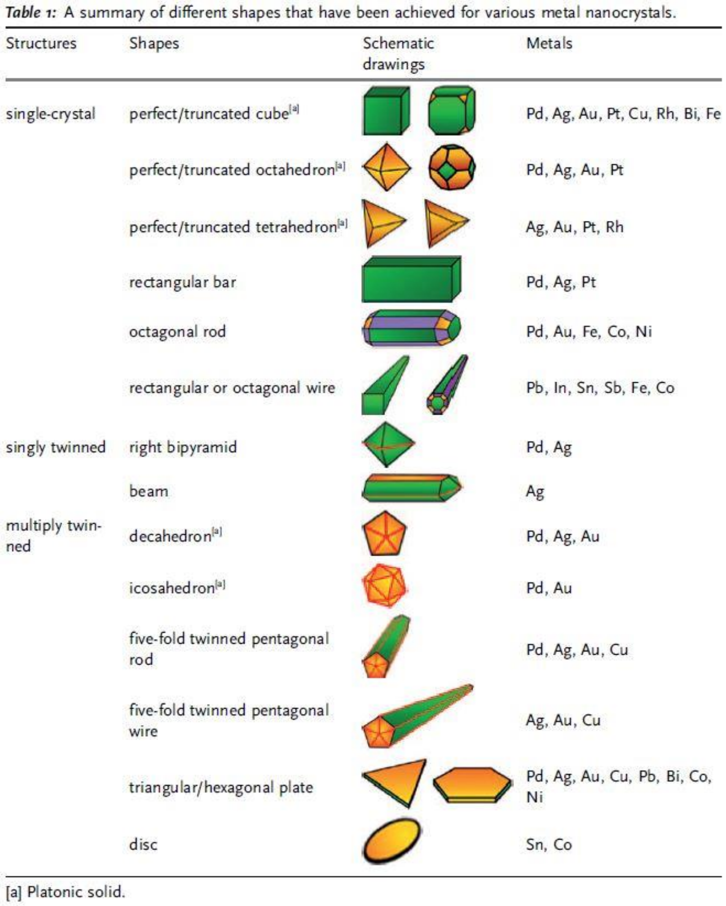

Table 1: A summary of different shapes that have been achieved for various metal nanocrystals.

Structures	Shapes	Schematic drawings	Metals
single-crystal	perfect/truncated cube[a]		Pd, Ag, Au, Pt, Cu, Rh, Bi, Fe
	perfect/truncated octahedron[a]		Pd, Ag, Au, Pt
	perfect/truncated tetrahedron[a]		Ag, Au, Pt, Rh
	rectangular bar		Pd, Ag, Pt
	octagonal rod		Pd, Au, Fe, Co, Ni
	rectangular or octagonal wire		Pb, In, Sn, Sb, Fe, Co
singly twinned	right bipyramid		Pd, Ag
	beam		Ag
multiply twinned	decahedron[a]		Pd, Ag, Au
	icosahedron[a]		Pd, Au
	five-fold twinned pentagonal rod		Pd, Ag, Au, Cu
	five-fold twinned pentagonal wire		Ag, Au, Cu
	triangular/hexagonal plate		Pd, Ag, Au, Cu, Pb, Bi, Co, Ni
	disc		Sn, Co

[a] Platonic solid.

Figure 1. Different shapes of metal nanocrystals

A wide array of metal nanocrystal shapes has been achieved, ranging from simple geometries like spheres, cubes, tetrahedrons, octahedrons, decahedrons, and icosahedrons to 1- or 2-dimensional forms such as rods, wires, plates, discs, and triangular- and hexagonal plates, as well as more complex structures like bi-pyramids, tetrapods, and hyper-branched shapes (Figure 1).[19,20] Nanoparticles with extensive surface areas offer an abundance of active sites, which can reduce the activation energy required for catalytic reactions. Additionally, distinctive surface features, including steps, kinks, and terraces, can significantly influence reaction pathways, thereby affecting product selectivity. Several methods have been employed to generate diverse morphologies of metal nanoparticles. Using the colloidal synthesis method, specific morphologies can be obtained by controlling the concentration of metal precursors, the presence of reductants and shape controllers, as well as the solvent. Since surface atoms play crucial roles in catalytic reactions, controlling shape and composition can achieve targeted outcomes in electrocatalytic development.

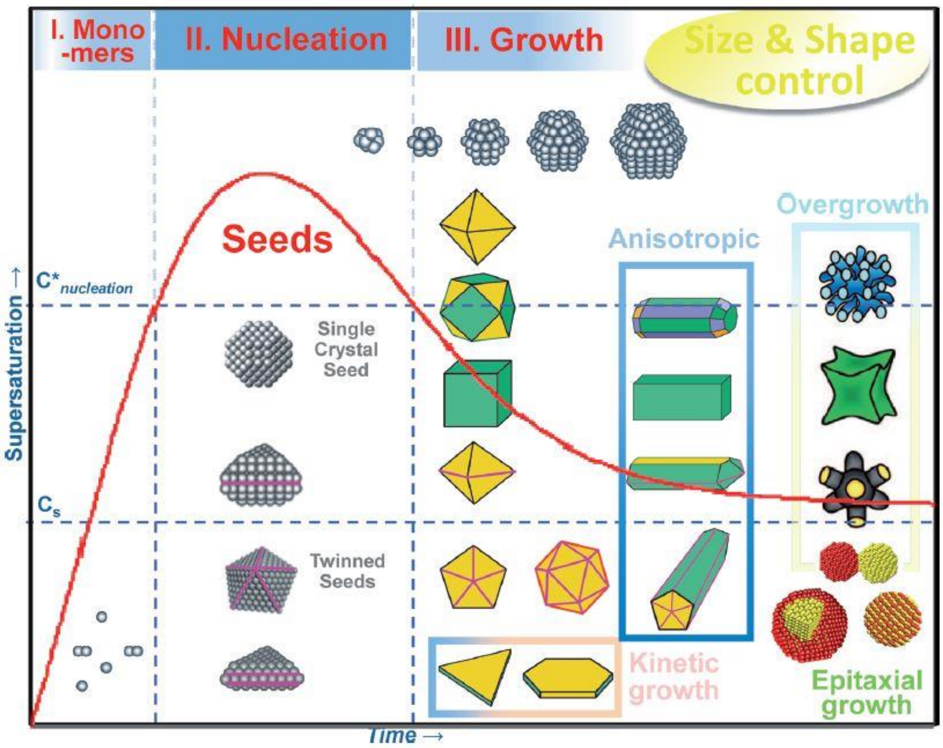

Figure 2. An illustration of general synthetic strategies for size and shape control of metal nanoparticles combining with the LaMer diagram

The colloidal synthesis method often employs the LaMer model to elucidate the mechanism behind colloidal nanoparticle formation, which unfolds in three distinct phases: monomer supersaturation, rapid nucleation, and controlled growth leading to uniform size distribution (Figure 2).[17] Initially, monomers, formed from precursors and stabilized by surfactants, gradually increase in concentration within the solution. Upon exceeding a critical supersaturation threshold, small clusters spontaneously form, diminishing the monomer concentration through nucleation. When the monomer concentration drops below this critical level, nucleation ceases, directing monomers solely towards particle growth. To minimize particle size variability, a short nucleation phase coupled with slow growth kinetics is crucial. The residual precursors form more stable complexes, facilitating slow growth by methodically integrating into the existing nuclei. Essential equipment for colloidal reactions includes a magnetic stir bar, a stirring plate, a heating mantle or oil bath for precise temperature control, a three-necked flask, a thermocouple for monitoring temperature, and a reflux condenser attached to an inert gas line with a bubbler, ensuring consistent and even reactions in high-temperature solutions.

Recent advancements in the development of metal nanocrystals have embraced the incorporation of multiple elements, leading to the formation of bimetallic, trimetallic, and high-entropy alloy compositions (Figure 3). In particular, Pd-based bimetallic nanocrystals have made significant inroads into the domain of renewable energy conversion, utilizing both noble and non-noble metal elements as pairing components. For instance, bimetallic PdPt nanoparticles have been employed to minimize Pt usage while simultaneously enhancing the electronic properties of Pd, thereby boosting catalytic performance.[21-23] Additionally, the inclusion of non-noble transition metals such as Co, Fe, Ni, Mo, and W has been demonstrated to improve the intrinsic properties and, as a result, increase the catalytic activity of Pd.[24-26] The use of Pd-based catalysts also alters the synergistic effects between strain and ligand influences following the addition of foreign elements. The strain effect, driven by lattice mismatches, can modify the electronic structure of active sites, with strain categorized into tensile and compressive types. Compressive strain results in an overlap and widening of the d-band, moving the d-band center away from the Fermi level, while tensile strain brings the d-band center closer.[27,28] Differences in atomic spacing, owing to varied morphologies and phase structures in alloys or core-shell arrangements, can induce strain effects to varying degrees, influencing the adsorption strength of intermediates differently. Ligand effects, apparent in alloy compositions, facilitate significant electron transfer between Pd and other metals, allowing for the facile tuning electronic structure of Pd. Metals such as Rh, Ir, and others with higher electronegativity can induce an electron-deficient state in Pd, reducing the affinity of oxygen-containing species to the Pd surface.

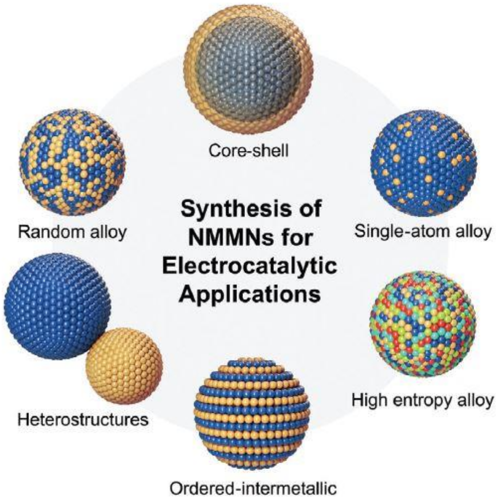

Figure 3. Categorization of NMMNs for electrocatalytic applications based on their structural characteristics.

1.3 Electrocatalysis with Surface-Modified Pd-Based Catalysts

The formation of intermetallic compounds represents a fascinating aspect of materials science, particularly within the realm of nanoengineering. Through this process, it is possible to significantly alter the local atomic configuration and symmetry, including the space group, by introducing foreign atoms or additives. Such modifications can lead to changes in crystallinity and induce various forms of disorder.[29-31] This is crucial because the introduction of structural and electronic imperfections can profoundly affect both the long-range and short-range order of atoms, influencing their distribution within the material. Furthermore, these alterations have significant implications for crystal morphology and secondary structural features. They can affect behaviors related to sintering and agglomeration, as well as the distribution of supports, which are critical factors in the performance of nanomaterials, especially in catalysis. From a thermodynamic perspective, the formation of solid-solution alloys or intermetallic compounds can be described by the equation (Figure 4):

$$\Delta G_f = \Delta H_f - T\Delta S_f$$

Where ΔG_f is the change in Gibbs free energy for the formation of the alloy, ΔH_f is the formation enthalpy, and ΔS_f is the formation entropy from pure metals, with T representing the absolute temperature. When the properties of the constituent elements are closely matched, ΔH_f tends to be close to zero or slightly negative, facilitating the formation of these compounds.

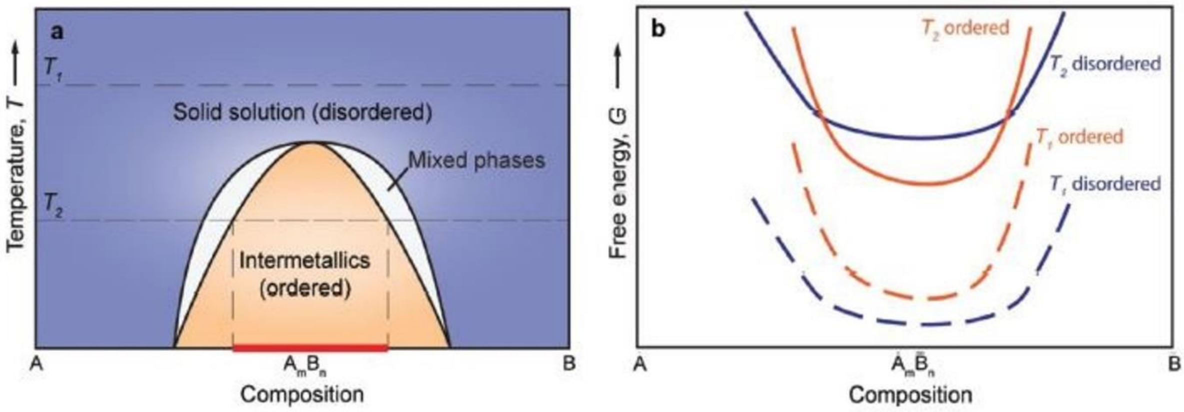

Figure 4. Schematic illustration of thermodynamic-equilibrium conditions for the formation of an intermetallic phase (A_mB_n) in the A.B binary system.

Intermetallic structures offer several advantages for electrocatalytic activity, making them highly desirable in various applications, including renewable energy conversion and storage.[29,32,33] Firstly, intermetallic compounds often exhibit unique electronic properties due to their distinct atomic arrangements and electronic structures. These properties can lead to enhanced catalytic performance, including improved activity, selectivity, and stability, compared to their pure metal counterparts. The ordered arrangements within intermetallic compounds can also create uniform and well-defined active sites, which are crucial for achieving high catalytic efficiency. Moreover, intermetallic compounds tend to possess high structural stability under catalytic operation conditions. This stability is beneficial for maintaining the integrity of the active sites and preventing degradation over time, thus ensuring long-term durability of the catalyst. The ability to tailor the electronic and structural properties of intermetallic compounds through nanoengineering techniques further enhances their attractiveness for use in advanced catalytic systems**.**

Integrating non-metal dopants into intermetallic compounds is a strategy to adjust the electronic characteristics of catalysts, drawing considerable attention in the realm of materials science. The infusion of non-metallic and metalloid elements into Pd-based nanostructures (NCs) is particularly noteworthy. Elements such as hydrogen, boron, phosphorus, carbon, sulfur, and nitrogen are capable of altering the electronic and geometric structure of metal catalysts, thus improving their performance and specificity in a range of chemical reactions.[10,34-38] Specifically, boron, with its comparatively smaller atomic radius (87 pm) versus palladium (137 pm), can be doped into the spaces within the Pd lattice.

This process of boron doping into Pd-based NCs not only expands the lattice spacing but also introduces tensile strain and increases the availability of surface electron sites. These sites are crucial for the adsorption of intermediates in electrocatalytic processes. The introduction of tensile strain is known to shift the d-band center upwards, which can enhance the adsorption of certain intermediate species.[37] Such an enhancement might increase the likelihood of CO poisoning on the catalyst surface by strengthening the CO adsorption. On the other hand, lowering the d-band center reduces the binding energy of these intermediates, mitigating the CO poisoning effect and promoting selectivity towards the C1 pathway.11 Nonetheless, this adjustment might also reduce the catalyst's ability to facilitate carbonaceous intermediates, thereby potentially decreasing the overall catalytic efficiency. This presents a nuanced challenge in designing EOR catalysts that are both highly selective and active. A previous study by Zhang et al. successfully introduced hydrogen into a PdGa single atom alloy metallene. This incorporation was achieved through strong p-d orbital hybridization interactions and a tensile strain effect, which resulted in an optimal C1 pathway selectivity of 54.7%. The enhancement in EOR performance and the increased yield of the C1 product can be attributed to the insertion of hydrogen, which induces a tensile strain. Moreover, the p-d hybridization interaction between Ga and Pd is significantly enhanced by hydrogen implementation, seamlessly connecting this advancement with the broader context of tuning electronic properties in catalysts through non-metal doping.[37] This approach underscores the effectiveness of altering the electronic and geometric landscape of metal catalysts to improve their catalytic activity and selectivity in various reactions.

In conclusion, the combination of intermetallic formation and boron doping emerges as a potent strategy for surface modification, offering new avenues for the development of highly efficient electrocatalysts. This approach not only enhances catalytic activity and selectivity but also contributes to the fundamental understanding of material science and catalysis, paving the way for the design of next-generation catalysts for energy conversion technologies.

1.4 References

1. Seh, Z. W.; Kibsgaard, J.; Dickens, C. F.; Chorkendorff, I.; Norskov, J. K.; Jaramillo, T. F. *Science* **2017,** 355, (6321).

2. Cui, Z.; Jiao, W.; Huang, Z.; Chen, G.; Zhang, B.; Han, Y.; Huang, W. *Small* **2023,** 19, (35), e2301465.

3. Nakaya, Y.; Furukawa, S. *Chem Rev* **2023,** 123, (9), 5859-5947.

4. Zaera, F. *Chem Rev* **2022,** 122, (9), 8594-8757.

5. Li, H.; Li, G. *Journal of Materials Chemistry A* **2023,** 11, (17), 9383-9400.

6. Chen, A.; Ostrom, C. *Chem Rev* **2015,** 115, (21), 11999-2044.

7. Shen, T.; Zhang, J.; Chen, K.; Deng, S.; Wang, D. *Energy & Fuels* **2020,** 34, (8), 9137-9153.

8. Xu, B.; Zhang, Y.; Li, L.; Shao, Q.; Huang, X. *Coordination Chemistry Reviews* **2022,** 459, 214388.

9. Chen, Z.; Vorobyeva, E.; Mitchell, S.; Fako, E.; Ortuno, M. A.; Lopez, N.; Collins, S. M.; Midgley, P. A.; Richard, S.; Vile, G.; Perez-Ramirez, J. *Nat Nanotechnol* **2018,** 13, (8), 702-707.

10. Sun, L.; Lv, H.; Wang, Y.; Xu, D.; Liu, B. *J Phys Chem Lett* **2020,** 11, (16), 6632-6639.

11. Lestarini, D. T.; Hong, J. W. *Applied Surface Science* **2023,** 610, 155311-155319.

12. Zhao, X.; Chang, Y.; Chen, W. J.; Wu, Q.; Pan, X.; Chen, K.; Weng, B. *ACS Omega* **2022,** 7, (1), 17-31.

13. Zhang, G.; Qin, X.; Deng, C.; Cai, W.-B.; Jiang, K. *Advanced Sensor and Energy Materials* **2022,** 1, (2), 100007.

14. Fan, J.; Du, H.; Zhao, Y.; Wang, Q.; Liu, Y.; Li, D.; Feng, J. *ACS Catalysis* **2020,** 10, (22), 13560-13583.

15. Back, S.; Jung, Y. *ChemCatChem* **2017,** 9, (16), 3173-3179.

16. Cui, M.; Johnson, G.; Zhang, Z.; Li, S.; Hwang, S.; Zhang, X.; Zhang, S. *Nanoscale* **2020,** 12, (26), 14068-14075.

17. An, K.; Somorjai, G. A. *ChemCatChem* **2012,** 4, (10), 1512-1524.

18. Li, S.; Jin, H.; Wang, Y. *Nanoscale* **2023,** 15, (6), 2488-2515.

19. Guo, J.; Liu, W.; Fu, X.; Jiao, S. *Nanoscale* **2023,** 15, (19), 8508-8531.

20. Hui Zhang, M. J., Yujie Xiong, Byungkwon Lim, Younan Xia. *Accounts of Chemical Research* **2013,** 46, (8), 1783-1794.

21. Tang, J.-X.; Chen, Q.-S.; You, L.-X.; Liao, H.-G.; Sun, S.-G.; Zhou, S.-G.; Xu, Z.-N.; Chen, Y.-M.; Guo, G.-C. *Journal of Materials Chemistry A* **2018,** 6, (5), 2327-2336.

22. Shi, L.; Wang, Q.; Ren, Q.; Yang, Q.; Zhao, D.; Feng, Y.; Chen, H.; Wang, Y. *Small* **2022,** 18, (3), e2103665.

23. Sun, Y.; Huang, L.; Shan, Q.; Li, G.; Zheng, Z.; Jiang, Q.; Jiang, Y.; Xie, Z. *ACS Applied Energy Materials* **2022,** 5, (9), 10907-10914.

24. Hu, Z.; Chen, K.; Zhu, Y.; Liu, B.; Shen, J. *Small* **2024**, e2309819.

25. Zhao, X.; Cheng, H.; Chen, X.; Zhang, Q.; Li, C.; Xie, J.; Marinkovic, N.; Ma, L.; Zheng, J. C.; Sasaki, K. *J Am Chem Soc* **2024,** 146, (5), 3010-3022.

26. Kwon, J.; Sun, S.; Choi, S.; Lee, K.; Jo, S.; Park, K.; Kim, Y. K.; Park, H. B.; Park, H. Y.; Jang, J. H.; Han, H.; Paik, U.; Song, T. *Adv Mater* **2023,** 35, (26), e2300091.

27. Jiao, L.; Liu, E.; Hwang, S.; Mukerjee, S.; Jia, Q. *ACS Catalysis* **2021,** 11, (13), 8165-8173.

28. Wu, C.; Li, H.; He, H.; Song, Y.; Bi, C.; Du, W.; Xia, H. *ACS Appl Mater Interfaces* **2019,** 11, (50), 46902-46911.

29. Yan, Y.; Du, J. S.; Gilroy, K. D.; Yang, D.; Xia, Y.; Zhang, H. *Adv Mater* **2017,** 29, (14), 1605997.

30. Guo, J.; Jiao, S.; Ya, X.; Zheng, H.; Wang, R.; Yu, J.; Wang, H.; Zhang, Z.; Liu, W.; He, C.; Fu, X. *Chemistry* **2022,** 28, (69), e202202221.

31. Liu, J.; Lee, C.; Hu, Y.; Liang, Z.; Ji, R.; Soo, X. Y. D.; Zhu, Q.; Yan, Q. *SmartMat* **2023,** 4, (4), a1210.

32. Kim, H. Y.; Jun, M.; Joo, S. H.; Lee, K. *ACS Nanosci Au* **2023,** 3, (1), 28-36.

33. Han, S.; Sun, H.; Ma, C.; Yun, Q.; He, C.; Ma, X.; Zhang, H.; Feng, F.; Meng, X.; Xia, J.; Wang, A. L.; Cao, W.; Lu, Q. *Advanced Functional Materials* **2024,** 2403023.

34. Jiang, R.; Tran, D. T.; McClure, J. P.; Chu, D. *ACS Catalysis* **2014,** 4, (8), 2577-2586.

35. Lv, H.; Xu, D.; Sun, L.; Henzie, J.; Suib, S. L.; Yamauchi, Y.; Liu, B. *ACS Nano* **2019,** 13, (10), 12052-12061.

36. Wang, H.; Li, Y.; Liu, S.; Yu, H.; Deng, K.; Wang, Z.; Xu, Y.; Wang, L. *Inorg Chem* **2023,** 62, (37), 15157-15163.

37. Zhang, G.; Hui, C.; Yang, Z.; Wang, Q.; Cheng, S.; Zhang, D.; Cui, P.; Shui, J. *Applied Catalysis B: Environmental* **2024,** 342, 123377.

38. Liu, J.; Jia, J.; Li, S.; Chang, Y.; Guo, S.; Yue, T.; Jia, M. *Journal of Alloys and Compounds* **2023,** 948, 169779.

Chapter 2. Intermetallic Pd_3Pb Nanobranches with Low-coordinated Surface Atoms for Highly Efficient Ethanol Oxidation Reaction

2.1 Introduction

Fuel cell systems based on the electrochemical oxidation of liquid fuels have been receiving significant attention in recent years due to the advantages of not only facile storage and transportability but also the high energy density of liquid fuels [1-4]. Of various liquid fuel cells, direct ethanol fuel cells (DEFCs) have piqued enormous interest because of the large scalable productivity and low toxicity of ethanol [5-7]. However, despite their great potential, insufficiently active and stable catalysts for electrochemical ethanol oxidation at the anode have hindered the advancement of DEFCs for practical applications [8-11]. In the past decades, metal nanocrystals (NCs) with controlled shapes are receiving enormous attention as promising candidates for the ethanol oxidation reaction (EOR) in DEFCs [12-19]. Among the various morphologies of metal NCs, nanobranches (NBs) have recently attracted tremendous attention attributed to their high porosity, large surface area, and efficient mass transport [20-23]. Furthermore, several low-coordinated surface atoms such as step, ledges, and kink atoms in branches of NBs can improve various fuel electrochemical oxidation reactions [24-26]. Owing to the advantages of NBs, various synthetic strategies for metal NBs such as kinetically controlled overgrowth, aggregation-based growth, heterogeneous seeded growth, selective etching, and template-directed methods have been developed, enhancing various electrocatalytic reactions [27-29].

Besides tunning the morphology of NCs, an effective strategy to ameliorate the catalytic function of NCs is to prepare bimetallic NCs. Bimetallic NCs can modify electronic properties to increase the rate of catalytic reaction [30-34]. Furthermore, incorporating auxiliary metals into bimetallic NCs can provide additional catalytic functions, which cannot only increase the reaction rate by accelerating the formation rate of products but also improve the removal of surface poisoning adsorbates [35-37]. Recently, among various bimetallic NCs with different atomic distributions, intermetallic NCs have exhibited interesting electrocatalytic properties because of their long periodic atomic arrangement [38-42]. This unique atomic distribution of intermetallic NCs alleviates the formation of surface poisoning adsorbates and improves electrocatalytic activity and stability [43-45]. Based on these facts, although intermetallic NBs with low-coordinated surface atoms can be considered promising candidates as EOR catalysts, great difficulties in synthesizing intermetallic NBs have impeded the synthesis and investigation of their electrocatalytic properties.

In this study, the successful synthesis of intermetallic Pd_3Pb NBs with a high density of low-coordinated surface atoms via wet-chemical synthesis was reported. The formation of Pd_3Pb NBs was sensitive to not only the growth rate control by the reducing agent (ascorbic acid, AA) but also surface stabilization by the capping agent (ammonium bromide, NH_4Br). The mass activity of Pd_3Pb NBs for the EOR in an alkaline electrolyte was 2.1 and 3.0 times higher than those of Pd_3Pb nanocubes and commercial Pd/C catalysts, respectively. The excellent performance of Pd_3Pb NBs for the EOR is attributed to effective adsorption of ethanol and $(OH)_{ads}$ and improved removal capability of carbonaceous intermediates adsorbed on the active sites of Pd_3Pb NBs due to the intermetallic Pd–Pb composition and high density of low-coordinated surface atoms in their branches. This study presents a facile strategy for the efficient synthesis of intermetallic electrocatalysts with low-coordinated surface atoms and provides an insight into the fuel oxidation reaction mechanism in alkaline electrolytes.

2.2 Experimental Section

2.2.1 Chemical and Materials

Palladium(II) acetylacetonate ($Pd(acac)_2$, 99%), 1-octadecene (ODE, 90.0%), ammonium bromide (NH_4Br, 99.0%), isopropanol (99%), and Nafion perfluorinated resin solution (5 wt%) were obtained from Sigma-Aldrich. Oleylamine (OAm, 50%) was obtained from TCI chemical. Lead(II) 2,4-pentanedionate ($Pb(acac)_2$, 99%) and commercial Pd/C (30 wt%) were obtained from Alfa aesar. Potassium hydroxide (KOH, 95.0%) was obtained from Samchun. L-ascorbic acid (AA, 99.5%) and ethanol absolute (99%) were obtained from Daejung. Other chemicals were of reagent grade, and deionized water with resistivity greater than 18.3 MΩ·cm was used in preparing the reaction solutions. Hexane and tetrahydrofuran were of technical grade.

2.2.2 Synthesis of Pd_3Pb NBs and Pd_3Pb nanocubes

For the synthesis of Pd_3Pb NBs, 7.6 mg of $Pd(acac)_2$, 17.8 mg of AA, and 2.5 mL of ODE were mixed in a 30-mL vial. The mixture was sonicated until it dissolved and then transferred into an oil bath. The mixture was heated from room temperature to 100°C for 50 min (first growth solution). In another vial, 10.13 mg of $Pb(acac)_2$, 50 mg of NH_4Br, and 2.5 mL of OAm were mixed and heated in a water bath at 85°C for 50 min (second growth solution). After 50 min, the second growth solution was injected into the first growth solution and heated at 100°C, and the reaction was maintained for 12 h.

For the synthesis of Pd_3Pb nanocubes, 7.6 mg of $Pd(acac)_2$, 8 mg of $Pb(acac)_2$, 10 mg of NH_4Br, 3 mL of OAm, and 3 mL of ODE were mixed in a 20-mL vial. The mixture was sonicated for 15 min and then heated at 200°C for 12 h.

2.2.3 Electrochemical Measurements

Electrochemical measurements were conducted in a three-electrode cell using Bio-Logic EC-Lab SP-300. Pt mesh and Hg/HgO (1 M NaOH) were used as the counter and reference electrodes, respectively. All electrochemical data were obtained at room temperature. The working electrode was a 5-mm diameter glassy carbon electrode (GCE) with 3 µL of drop-casted catalyst ink (1 µg of total Pd). The precise amount of Pd loaded on the GCE was determined by inductively coupled plasma-optical emission spectroscopy (ICP-OES). The electrolyte solutions were purged with N_2 gas for 30 min before conducting electrochemical experiments. The dried GCE was electrochemically cleaned by 30 potential cycles between –0.944 and 0.356 V vs. Hg/HgO at a scan rate of 50 mV s^{-1} in 0.5-M KOH. The cyclic voltammograms (CVs) of all catalysts were obtained between –0.844 and 0.356 V vs. Hg/HgO at a scan rate of 50 mV s^{-1}. For CO-stripping experiments, the surface of the catalysts loaded on the GCE was saturated with CO by purging with CO gas in 0.5-M KOH while holding the working electrode at –0.3 V vs. Hg/HgO for 15 min, and then CO dissolved in the electrolyte was removed by purging with N_2 gas for 30 min.

2.2.4 Characterization

Transmission electron microscopy (TEM) and scanning electron microscopy (SEM) images of the prepared catalysts were obtained by using a JEOL JEM-2100F and a JEOL JEM-7210F, respectively. ICP-OES measurement was conducted using a Spectrouble-ICP-OES (Ametek). X-ray diffraction (XRD) measurement was conducted on a Rigaku D/MAX2500V/PC. X-ray photoelectron spectroscopy (XPS) measurements were conducted using a Thermo VG Scientific Sigma Probe spectrometer with Al Kα X-ray (1486.6 eV) as a light source. XPS data were calibrated using the C 1s peak at 284.5 eV. The d-band center positions relative to the Fermi level of Pd_3Pb NBs and Pd_3Pb nanocubes were calculated from XPS spectra of the valence region using the following equation:

$$d - band\ center = -\frac{\int_{0eV}^{10\ eV}[Binding\ energy\ (E)\ x\ Intensity\ (E)]dE}{\int_{0eV}^{10\ eV} Intensity\ (E)dE}.$$

2.3 Result and Discussions

2.3.1 Characterization of Pd_3Pb NBs

Intermetallic Pd_3Pb NBs were prepared using a two-sequence synthetic method via wet-chemical synthesis (Scheme 1), with AA as a reductant, OAm as a surfactant, and NH_4Br as a shape controller. Fig. 1a shows a representative TEM image of the products with the uniformity of the branched nanostructure, revealing the successful formation of NBs. The high-resolution TEM (HRTEM) image shows that several branches, similar to a nanorod, are radially extended from the core part in the NBs (Fig. 1b). The average total diameter is 146.13 ± 5.22 nm, determined from the tips of opposite branches in the NBs, and the average thickness of the branches is 49.84 ± 1.04 nm. The elemental mapping of an NB obtained by high-angle annular dark-field scanning TEM combined with energy-dispersive X-ray spectroscopy (HAADF-STEM–EDS) demonstrates that the prepared NBs have Pd–Pb bimetallic alloy structure (Fig. 1c). The Pd/Pb atomic ratio of the NBs was determined to be 75.4/24.6 and 73.4/26.6 by ICP-OES and EDS elemental analysis, respectively, confirming the formation of Pd_3Pb NBs. The d-spacing of adjacent lattice fringes of the Pd–Pb NBs was 2.34 Å (inset of Fig. 1b), which matches well with the previously reported value of the (111) planes of a Pd–Pb alloy. The XRD pattern of the NBs exhibits an intermetallic primitive cubic phase (JCPDS No. 50-1631), with no typical peaks indexed to pure Pb and Pd crystal phases (Fig. 1d). XPS measurements of the Pd–Pb NBs show that Pd and Pb are in the metallic state (Fig. 1e,f). These experimental results verify the successful formation of intermetallic Pd_3Pb alloy NBs.

Given that the thickness of the tip of the branch in the Pd_3Pb NBs is thinner than that of the opposite side of the branch attached to the core part in the NBs, it can be expected that low-coordinated atoms such as step atoms exist on the surface of branches. To reveal the surface atomic structure of branches in the NBs, the surface atomic structure of Pd_3Pb NBs was characterized using TEM measurements, which show the low-coordinated step atoms on the surface of branches (Fig. 2). Since these step atoms on the surface of Pd_3Pb NBs are capable of sufficiently adsorbing $(COCH_3)_{ads}$ and $(OH)_{ads}$ species, Pd_3Pb NBs can provide more active catalytic sites for various electrocatalytic reactions, including the EOR. [46]

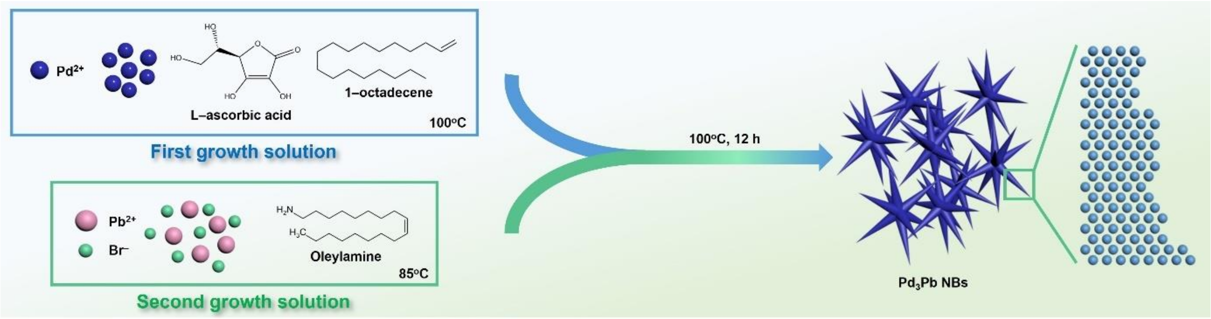

Scheme 1. Schematic illustration of the proposed formation mechanism of Pd_3Pb NBs.

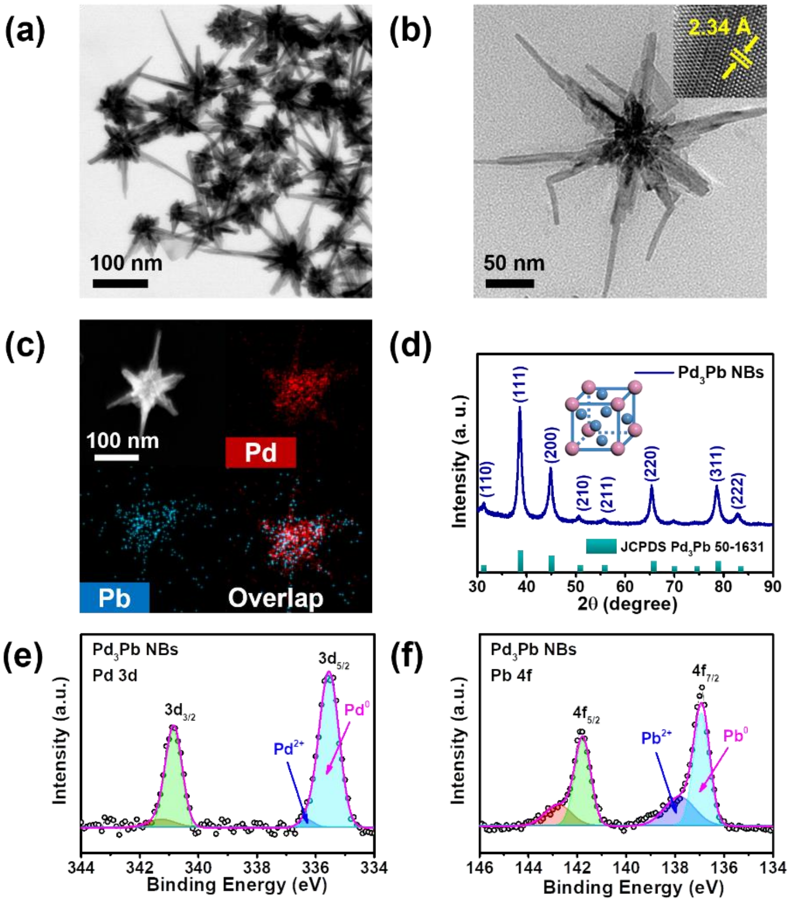

Figure. 1. (a) Low- and (b) high-magnification TEM images of Pd_3Pb NBs. The insets in (Fig. 1b) show the visible lattice fringes obtained from an arm of the branch in Pd_3Pb NBs. (c) HAADF-STEM and corresponding HAADF-STEM-EDS elemental mapping images of Pd_3Pb NBs. (d) XRD pattern of Pd_3Pb NBs, (e and f) XPS spectra of Pd_3Pb NBs of Pd 3d and Pb 4f.

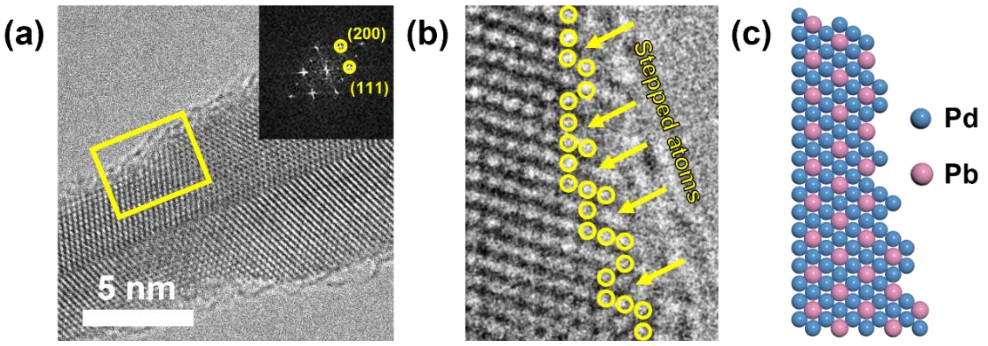

Figure. 2. (a) HRTEM images of a single branch, (b) High-magnification HRTEM image of the region inside the yellow rectangle in 2a shows the step atoms on NBs (c) Schematic illustration of intermetallic Pd_3Pb NBs.

2.3.2 Growth mechanism of Pd_3Pb NBs

A time-lapse study was conducted to observe the morphological evolution from the initial stage of fabrication of Pd_3Pb NBs. Fig. 2 depicts SEM images of the products obtained from different reaction times of 1, 2, 4, and 6 h measured after the injection of the Pb precursor into the reaction mixture, including the Pd precursor. When the reaction was performed for 1 h, small nanoparticles in irregular shapes with an average size of ~20 nm were yielded (Fig. 3a). As the reaction continued to 2 h, NBs composed of shorter lengths of branches were observed (Fig. 3b). When the reaction time was extended to 4 and 6 h, NBs with fully formed branches were observed, exhibiting morphology and sizes similar to typical Pd_3Pb NBs (Fig. 3c,d): the standard reaction time for typical Pd_3Pb NBs was 12 h. These observations signify that the small spherical seed NCs were formed at the initial stage of the reaction, and the subsequent reduction in the amount of the Pd and Pb precursors produces several branches, resulting in the formation of typical Pd_3Pb NBs.

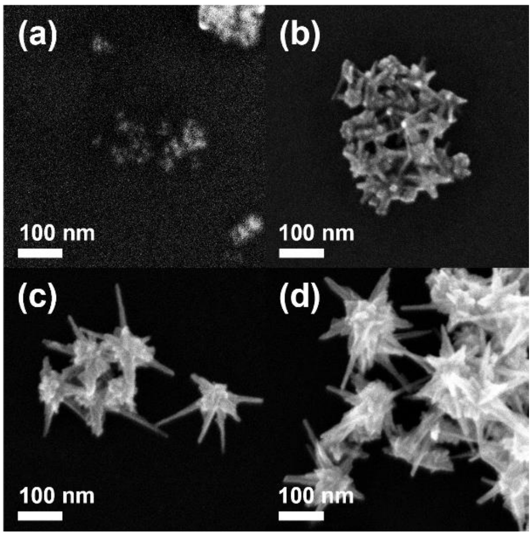

Figure. 3. SEM images of the samples taken at different reaction stages of Pd_3Pb NBs: (a) 1 h, (b) 2 h, (c) 4 h, and (d) 6 h.

For the successful synthesis of Pd_3Pb NBs, introducing the optimal growth kinetics of nanostructure and an effective capping agent is significant. First, to investigate the influence of growth kinetics of Pd–Pb nanostructures depending on the concentration of AA for the final morphology of Pd–Pb nanostructures, different concentrations of AA, ranging from 0 to 100 mM, were used in synthesizing Pd_3Pb NBs, while other reaction conditions were maintained (Fig. 4). In absence of AA, nanocubes were produced instead of NBs (Fig. 4a). When 5 mM AA was used (20 mM AA was used in the standard synthesis), irregular polyhedral nanostructures were observed (Fig. 4b). As the concentration of AA was increased to 50 and 100 mM, NBs were produced (Fig. 4c,d) even though they had unmatured branches with smaller branch lengths and diameters (~40 nm) than those of standard NBs prepared using 20 mM AA. These results indicate that a fast growth rate facilitates the formation of NBs and that the optimal growth rate by employing the appropriate AA concentration is critical to the formation of Pd_3Pb NBs with well-established branches.

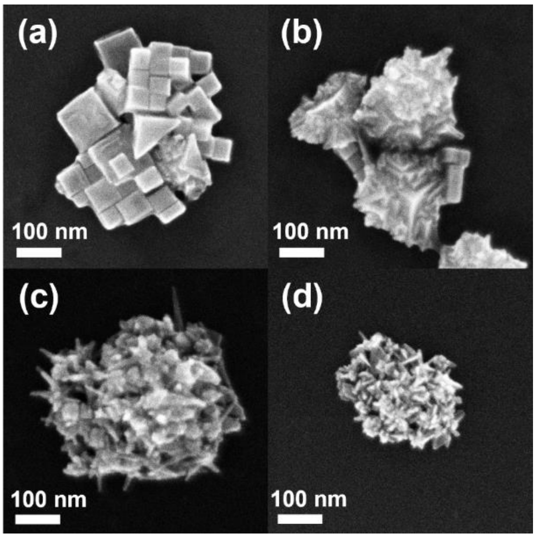

Figure. 4. SEM images of NCs produced in reaction mixtures with (a) 0, (b) 5, (c) 50, and (d) 100 mM of AA.

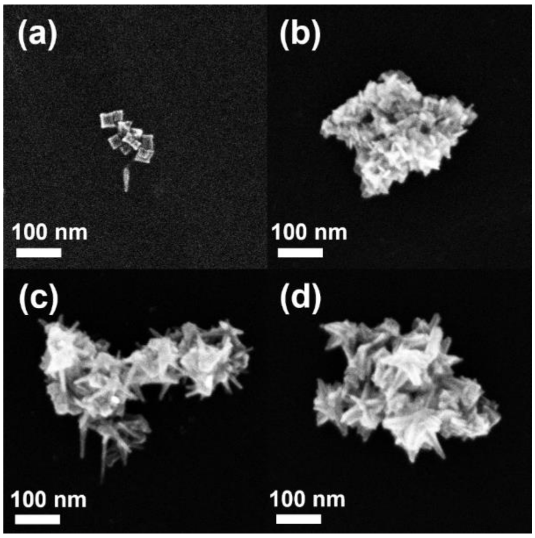

Figure. 5. SEM images of NCs produced in reaction mixtures with (a) 0, (b) 10, (c) 51, and (d) 204 mM of NH_4Br.

The introduction of NH_4Br is also crucial to the formation of well-constructed branches in Pd_3Pb NBs. A control experiment with different concentrations of NH_4Br was conducted to observe the morphological changes in the formation of NBs (Fig. 5). In the absence of NH_4Br, nanoparticles in cubic shapes with ~30 nm were formed, whereas the introduction of NH_4Br led to the formation of branches (Fig. 5a). When 10 mM NH_4Br was used, star-shaped nanoparticles were observed (Fig. 5b) (102 mM NH_4Br was used in the standard synthesis). As the amount of NH_4Br increased (51 mM), the stabilization of the surface of branches improved, which led to the complete formation of Pd_3Pb NBs (Fig. 5c). Excessive concentrations of NH_4Br (204 mM) hindered the growth of branches, thereby resulting in the formation of the short arms of NBs (Fig. 5d). These results signify that the presence of sufficient concentrations of NH_4Br facilitates the formation and stabilization of low-coordinated atomic surfaces on the branches of Pd_3Pb NBs. Overall, the findings from this series of control experiments collectively demonstrate that the successful formation of Pd_3Pb NBs with well-established branches can be realized by controlling the growth rate of nanostructure and the amount of an effective capping agent.

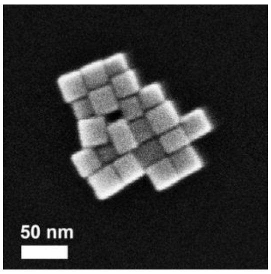

Figure. 6. SEM images of Pd_3Pb nanocubes.

2.3.3 Electrochemical measurements

The electrocatalytic performance of intermetallic Pd_3Pb NBs was evaluated in an anodic EOR to explore the influence of the intermetallic Pd–Pb alloy and morphological effects on the catalytic activity. Pd_3Pb nanocubes with an edge size of ~25 nm (Fig. 6) and commercial Pd/C were prepared as reference catalysts for comparison. Before the electrochemical tests, Pd_3Pb NBs and Pd_3Pb nanocubes were anchored on carbon black (Vulcan XC72R carbon, C). CVs of the catalysts are displayed in Fig. 6a, which are performed in a N_2-saturated 0.5-M KOH solution at a sweep rate of 50 mV s^{-1}. Based on the integration of the Coulombic charge for the reduction of oxygen species in CVs of the catalysts (Fig. 7a), the electrochemically active surface areas (ECSAs) of Pd_3Pb NBs, Pd_3Pb nanocubes, and Pd/C were estimated to be 34.74, 27.16, and 37.97 m^2 g^{-1}, respectively (Fig. 8): the ECSA of Pd_3Pb NBs was 1.3 times larger than that of Pd_3Pb nanocubes, which can be attributed to their morphological benefits. Fig. 3b shows the CVs of the different catalysts in a N_2-saturated 0.5 M KOH + 1.0 M ethanol solution at room temperature. Pd_3Pb NBs exhibited a lower onset potential and larger current density than Pd_3Pb nanocubes and Pd/C catalysts, indicating their superior EOR performance over Pd_3Pb nanocubes and Pd/C catalysts. The onset potential of Pd_3Pb NBs appeared at −0.44 V, whereas that of Pd_3Pb nanocubes and Pd/C catalysts appeared at −0.40 and −0.38 V, respectively (Fig. 7c). The mass activity of Pd_3Pb NBs was 5240 mA $mg^{-1}{}_{Pd}$, which was 2.2 and 3.0 times higher than those of Pd_3Pb nanocubes (2423 mA $mg^{-1}{}_{Pd}$) and Pd/C (1711 mA $mg^{-1}{}_{Pd}$) catalysts, respectively (Fig. 7b,e). The analogous trend was also observed in the specific activity (Fig. 7d,e). The electrochemical impedance spectroscopy (EIS) spectra of the catalysts were obtained in N_2-saturated 0.5 M KOH (Fig. 7f). The charge transfer resistance of Pd_3Pb NBs was significantly lower than that of Pd_3Pb nanocubes and Pd/C catalysts, indicating that Pd_3Pb NBs have faster charge transfer rate than Pd_3Pb nanocubes and Pd/C catalysts, resulting in the enhancement of EOR activity. Compared to previously reported electrocatalysts, the Pd_3Pb NBs in this study exhibit excellent electrocatalytic EOR performances in mass activity (Fig. 7g and Table 1).

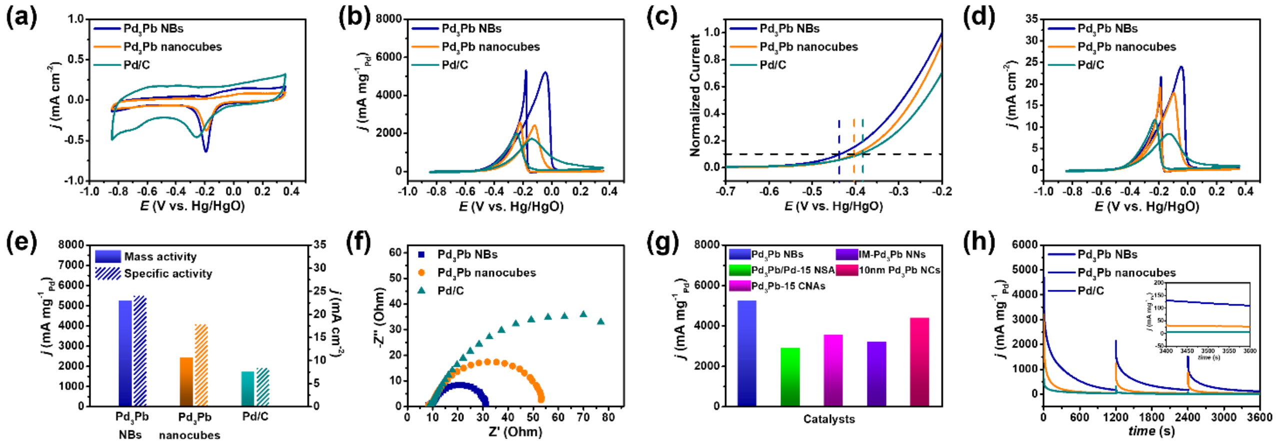

Figure. 7. CVs of various catalysts on GCE (a) in 0.5 M KOH, (b) in 0.5 M KOH and 1.0 M EtOH solution, (c) onset potential of all catalysts, (d) specific activity of all catalysts, (e) mass and specific activity of all catalysts, (f) EIS curves of all catalysts in 0.5 M KOH and 1.0 M EtOH, (g) comparison of catalysts in terms of mass activity, and (h) chronoamperometric curve of all catalysts in 0.5 M KOH and 1.0 M ethanol at –0.12 V and the inset figure in part (h) is CA from 3400 to 3600 s.

Table 1. Comparison of the mass activity of intermetallic Pd_3Pb NBs for EOR.

Catalysts	Mass activity	Electrolyte	Reference
Pd_3Pb NBs	5240 mA $mg^{-1}{}_{Pd}$	0.5-M KOH + 1.0-M EtOH	*This work*
Pd_3Pb/Pd-15 NSA	2886 mA $mg^{-1}{}_{Pd}$	1.0-M KOH + 1.0-M EtOH	[53]
Pd_3Pb-15 CNAs	3543 mA $mg^{-1}{}_{Pd}$	1.0-M KOH + 1.0-M EtOH	[54]
IM-Pd_3Pb NNs	3200 mA $mg^{-1}{}_{Pd}$	1.0-M KOH + 1.0-M EtOH	[55]
10 nm Pd_3Pb NCs	4400 mA $mg^{-1}{}_{Pd}$	0.5-M KOH + 0.5-M EtOH	[41]

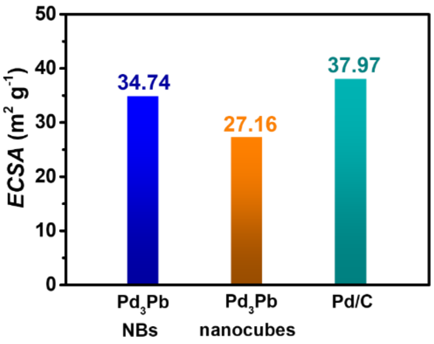

Figure. 8. ECSA of Pd_3Pb NBs, Pd_3Pb nanocubes, and Pd/C.

The electrochemical stabilities of Pd_3Pb NBs/C were estimated through chronoamperometry (CA) measurements and compared with those of Pd_3Pb nanocubes and commercial Pd/C catalysts. The CA test was conducted by repeating the cycle every 1200 s at −0.120 V vs. Hg/HgO in a N_2-saturated 0.5-M KOH + 1.0-M ethanol solution. Fig. 7h shows that Pd_3Pb NBs have a higher current density during long-term operations than Pd_3Pb nanocubes and Pd/C catalysts. Notably, after the third cycle, the residual current density of Pd_3Pb NBs is 4.5 and 19.9 times larger than those of Pd_3Pb nanocubes and

Pd/C catalysts (inset of Fig. 7h). In addition, the residual current density of Pd_3Pb NBs after three cycles was approximately 64.7% of that obtained after the first cycle, which was larger than those of Pd_3Pb nanocubes (56.8 %) and commercial Pd/C (17.5%), respectively.

It has been generally accepted that electrochemical ethanol oxidation can proceed by the C1 and C2 pathways, which form the $(CO)_{ads}$ and $(COCH_3)_{ads}$ carbonaceous intermediates, respectively. Then, electrochemical oxidation of $(CO)_{ads}$ and $(COCH_3)_{ads}$ by reacting with $(OH)_{ads}$ terminates the EOR cycle, which is generally accepted as rate-determining steps for each C1 and C2 EOR process, respectively.

C1:

$\mathrm{CH_3CH_2OH + 12OH^-} \rightarrow \mathrm{2CO_2 + 9H_2O + 12e^-}$ (Total reaction)

$\mathrm{Pd + CH_3CH_2OH} \rightarrow \mathrm{Pd{-}(CH_3CH_2OH)_{ads}}$ (Eq. 1)

$\mathrm{Pd{-}(CH_3CH_2OH)_{ads} + OH^-} \rightarrow \mathrm{Pd{-}(CH_3CHOH)_{ads} + H_2O + e^-}$ (Eq. 2)

$\mathrm{Pd{-}(CH_3CHOH)_{ads} + OH^-} \rightarrow \mathrm{Pd{-}(CH_3CHO)_{ads} + H_2O + e^-}$ (Eq. 3)

$\mathrm{Pd{-}(CH_3CHO)_{ads} + OH^-} \rightarrow \mathrm{Pd{-}(CH_3CO)_{ads} + H_2O + e^-}$ (Eq. 4)

$\mathrm{Pd{-}(CH_3CO)_{ads} + Pd} \rightarrow \mathrm{Pd{-}(CH_3)_{ads} + Pd{-}(CO)_{ads}}$ (Eq. 5)

$\mathrm{Pd{-}(CH_3)_{ads} + 5OH^-} \rightarrow \mathrm{Pd{-}(CO)_{ads} + 4H_2O + 5e^-}$ (Eq. 6)

$\mathrm{Pd{-}(2CO)_{ads} + 4OH^-} \rightarrow \mathrm{2CO_2 + 2H_2O + Pd + 4e^-}$ (Eq. 7)

C2:

$\mathrm{CH_3CH_2OH + 5OH^-} \rightarrow \mathrm{CH_3COO^- + 4H_2O + 4e^-}$ (Total reaction)

$\mathrm{Pd + CH_3CH_2OH} \rightarrow \mathrm{Pd{-}(CH_3CH_2OH)_{ads}}$ (Eq. 8)

$\mathrm{Pd{-}(CH_3CH_2OH)_{ads} + 3OH^-} \rightarrow \mathrm{Pd{-}(CH_3CO)_{ads} + 3H_2O + 3e^-}$ (Eq. 9)

$\mathrm{Pd{-}(CH_3CH_2OH)_{ads} + OH^-} \rightarrow \mathrm{Pd{-}(CH_3CHOH)_{ads} + H_2O + e^-}$ (Eq. 9-1)

$\mathrm{Pd{-}(CH_3CHOH)_{ads} + OH^-} \rightarrow \mathrm{Pd{-}(CH_3CHO)_{ads} + H_2O + e^-}$ (Eq. 9-2)

$\mathrm{Pd{-}(CH_3CHO)_{ads} + OH^-} \rightarrow \mathrm{Pd{-}(CH_3CO)_{ads} + H_2O + e^-}$ (Eq. 9-3)

$\mathrm{Pd + OH^-} \rightarrow \mathrm{Pd{-}(OH)_{ads} + e^-}$ (Eq. 10)

$\mathrm{Pd{-}(CH_3CO)_{ads} + Pd{-}(OH)_{ads}} \rightarrow \mathrm{Pd{-}CH_3COOH + Pd}$ (Eq. 11)

$\mathrm{Pd{-}CH_3COOH + OH^-} \rightarrow \mathrm{Pd + CH_3COO^- + H_2O}$ (Eq. 12)

Therefore, investigation of adsorption and desorption behaviors of the $(COCH_3)_{ads}$, $(CO)_{ads}$, and $(OH)_{ads}$ intermediates is significant for understanding the different catalytic performances of Pd_3Pb NBs, Pd_3Pb nanocubes, and Pt/C catalysts. Given the superior electrocatalytic activity and stability of Pd_3Pb NBs compared with those of Pd_3Pb nanocubes and commercial Pd/C catalysts, it can be speculated that Pd_3Pb NBs cause more optimal adsorption and desorption properties of the intermediates for electrooxidation than the Pd_3Pb nanocubes and commercial Pd/C catalysts due to the coexistence of the intermetallic Pd_3Pb composition and low-coordinated surface atoms on the branches of Pd_3Pb NBs. To confirm our assumption, further evaluation of the EOR for Pd_3Pb NBs, Pd_3Pb nanocubes, and Pd/C was performed with different concentrations of KOH and ethanol with respect to the I_f/I_b. First, to estimate the effects of $(OH)_{ads}$, CVs of the catalysts were obtained in various KOH concentrations while maintaining other conditions (Fig. 9a–c). The CVs of all catalysts show that their current peaks gradually shifted to negative potential with an increase in KOH concentration, which can be attributed to a larger coverage of the reactive Pd–$(OH)_{ads}$ in a higher KOH concentration.[28] It is generally accepted that $(OH)_{ads}$ can facilitate the electrochemical oxidation of both $(CO)_{ads}$ and $(COCH_3)_{ads}$ intermediates, which improves the EOR activity of electrocatalysts.[29, 47] The EOR catalytic activities of all catalysts were gradually improved with an increase in KOH concentration from 0.2 to 1.0 M due to the more efficient formation of $(OH)_{ads}$. In particular, Pd_3Pb NBs exhibit higher mass activity than Pd_3Pb nanocubes and Pd/C catalysts in all KOH concentrations, which is attributed to the more efficient formation of $(OH)_{ads}$ on the branches of NBs. In addition, we evaluated the mass activity of different catalysts in various ethanol concentrations to estimate the tendency in ethanol adsorption and transformation of ethanol to $(CH_3CO)_{ads}$ during the EOR (Fig. 9e–g). Similarly, the mass activity of the catalysts for the EOR was also enhanced with an increase in ethanol concentration due to the fast adsorption of ethanol and efficient formation of $(COCH_3)_{ads}$ in a high concentration of ethanol. The mass activity of Pd_3Pb NBs was higher than that of Pd_3Pb nanocubes and Pd/C catalysts in all ethanol concentrations. Based on Equation (9), this indicates that effective adsorption of ethanol and conversion of ethanol to $(COCH_3)_{ads}$ proceed more on Pd_3Pb NBs compared with on Pd_3Pb nanocubes and Pd/C catalysts. Notably, as shown in Tables 2 and 3, Pd_3Pb NBs have higher I_f/I_b ratios than Pd_3Pb nanocubes and commercial Pd/C catalysts in both KOH and ethanol control experiments: the I_f/I_b ratio order of the catalysts follows this sequence: Pd_3Pb NBs > Pd_3Pb nanocubes > commercial Pd/C (Fig. 9d,h). Because a higher I_f/I_b ratio generally indicates more effective electrochemical oxidation of the adsorbed carbonaceous intermediates, these results imply that, compared with Pd_3Pb nanocubes and Pd/C catalysts, Pd_3Pb NBs can efficiently promote the adsorption of $(OH)_{ads}$ and $(CH_3CO)_{ads}$, which can promote electrochemical oxidation between $(OH)_{ads}$ and carbonaceous intermediates ($(CH_3CO)_{ads}$ and $(CO)_{ads}$), enhancing EOR performance.[28] For too excessive a concentration of KOH (2.0 M) and ethanol (3.0 M), all catalysts showed a decrease in EOR activities than those in a lower concentration of KOH (1.0 M) and ethanol (2.0 M). Since the adsorption of hydroxide and ethanol is the competitive reaction in alkaline EOR, an excessively high concentration of one type of molecule can disturb the adsorption of the other molecule. Therefore, excessive concentration of KOH (2.0 M) or ethanol (3.0 M) reduces the EOR activity of the catalysts.

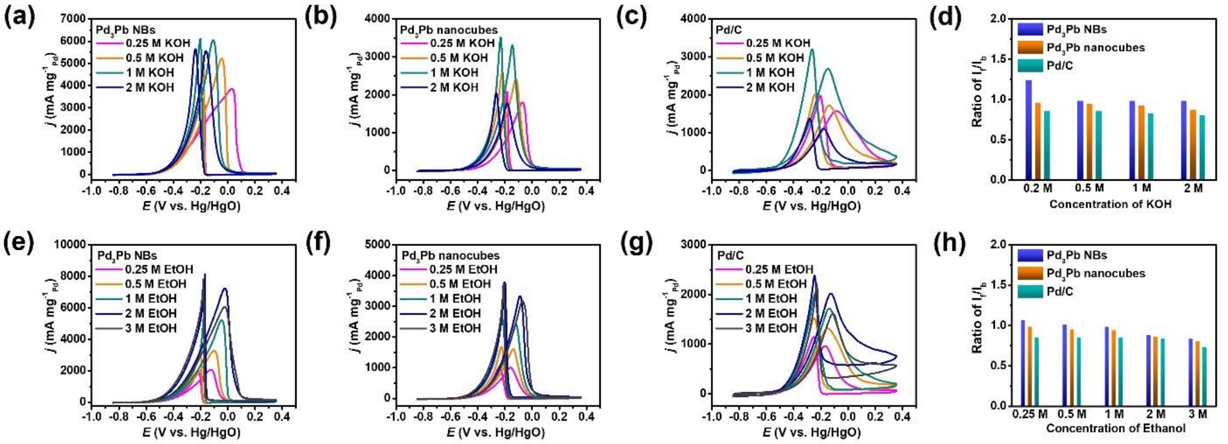

Figure. 9. CVs of catalysts on GCE (a–c) in different KOH concentrations and 1.0 M EtOH, (e–g) in different EtOH concentrations and 0.5 M KOH, and (d, h) the If/Ib ratio of catalysts in different concentrations of KOH and EtOH, respectively.

The (CO)ads formed through the C1 pathway are strongly adsorbed on the surface of catalysts, which disturbs the EOR by blocking the active sites of the catalysts. Therefore, CO removal ability by electrochemical oxidation with $(OH)_{ads}$ is also an important factor that affects the EOR performance of catalysts. To investigate the $(CO)_{ads}$ removal capability of the catalysts, CO-stripping voltammograms of the catalysts were obtained. Fig. 10 shows the obtained CO-stripping curves of the catalysts. There are two CO oxidation peaks for both Pd_3Pb NBs and nanocubes, which can be attributed to the different interaction of Pd and Pb surface atoms with CO.[48, 49] The main peak potentials of CO-stripping on Pd_3Pb NBs, Pd_3Pb nanocubes, and Pd/C were measured to be –0.131, –0.116, and –0.091 V vs Hg/HgO, respectively: additional negative shift of the main peak potentials on intermetallic Pd_3Pb NBs and Pd_3Pb nanocubes. In addition, the onset potentials on Pd_3Pb NBs and Pd_3Pb nanocubes also appeared at more negative potentials than that of Pd/C catalysts, indicating that the intermetallic Pd–Pb composition is more beneficial to remove the $(CO)_{ads}$ than pure Pd surfaces. According to the third-body effect, a chemically strong bond between the CO and Pt or Pd surfaces is formed on the two or three neighboring atoms [50-52]. Because intermetallic Pd_3Pb NBs and Pd_3Pb nanocubes have a low density of two or three neighboring Pd atoms because of the periodic Pd–Pb atomic sequences, they can form a weaker bond strength with CO, which can account for their superb CO removal ability of compared to Pd/C catalysts. Furthermore, the exposed exophilic Pb sites can provide abundant $(OH)_{ads}$ to the surface of Pd atoms, thereby enhancing the CO removal ability of Pd_3Pb NBs and nanocubes. Compared with Pd_3Pb nanocubes, Pd_3Pb NBs showed superior CO removal ability, which can be attributed to the modification of the electronic structure originating from their distinct surface containing low-coordinated atoms.

Table 2. Mass activity and I_f/I_b ratio of Pd_3Pb NBs, Pd_3Pb nanocubes, and Pd/C catalysts in various KOH concentrations and 1.0-M EtOH.

Concentration of KOH	Pd_3Pb NBs		Pd_3Pb nanocubes		Pd/C	
	Mass activity	I_f/I_b	Mass activity	I_f/I_b	Mass activity	I_f/I_b
0.2 M	3884 mA mg^{-1}_{Pd}	1.24	1818 mA mg^{-1}_{Pd}	0.95	1596 mA mg^{-1}_{Pd}	0.85
0.5 M	5240 mA mg^{-1}_{Pd}	0.98	2423 mA mg^{-1}_{Pd}	0.94	1711 mA mg^{-1}_{Pd}	0.85
1 M	6038 mA mg^{-1}_{Pd}	0.98	3275 mA mg^{-1}_{Pd}	0.92	2664 mA mg^{-1}_{Pd}	0.82
2 M	5568 mA mg^{-1}_{Pd}	0.98	1792 mA mg^{-1}_{Pd}	0.87	1118 mA mg^{-1}_{Pd}	0.80

Table 3. Mass activity and I_f/I_b ratio of Pd_3Pb NBs, Pd_3Pb nanocubes, and Pd/C catalysts in various EtOH concentrations and 0.5-M KOH.

Concentration of EtOH	Pd_3Pb NBs		Pd_3Pb nanocubes		Pd/C	
	Mass activity	I_f/I_b	Mass activity	I_f/I_b	Mass activity	I_f/I_b
0.25 M	2077 mA mg^{-1}_{Pd}	1.06	1001 mA mg^{-1}_{Pd}	0.98	968 mA mg^{-1}_{Pd}	0.85
0.5 M	3287 mA mg^{-1}_{Pd}	1.01	1603 mA mg^{-1}_{Pd}	0.95	1320 mA mg^{-1}_{Pd}	0.85
1 M	5240 mA mg^{-1}_{Pd}	0.98	2423 mA mg^{-1}_{Pd}	0.94	1711 mA mg^{-1}_{Pd}	0.85
2 M	7235 mA mg^{-1}_{Pd}	0.88	3328 mA mg^{-1}_{Pd}	0.86	2020 mA mg^{-1}_{Pd}	0.84
3 M	6078 mA mg^{-1}_{Pd}	0.83	3172 mA mg^{-1}_{Pd}	0.80	1614 mA mg^{-1}_{Pd}	0.73

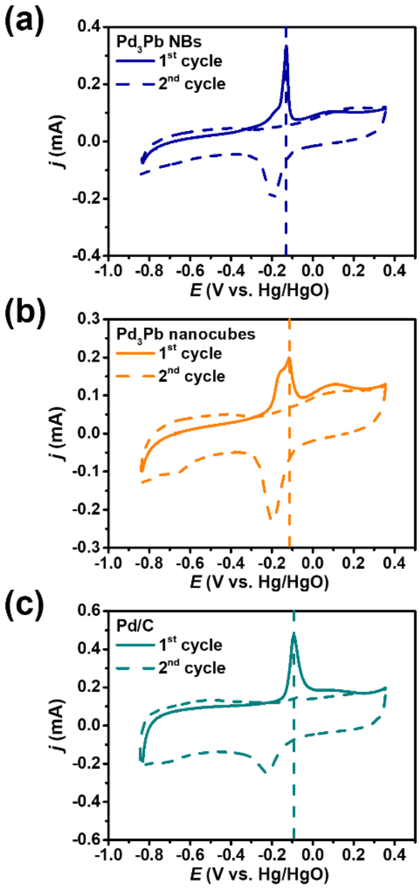

Figure. 10. (a–c) CO-stripping voltammograms of Pd_3Pb NBs, Pd_3Pb nanocubes, and Pd/C in 0.5 M KOH at a scan rate of 20 mV s^{-1}.

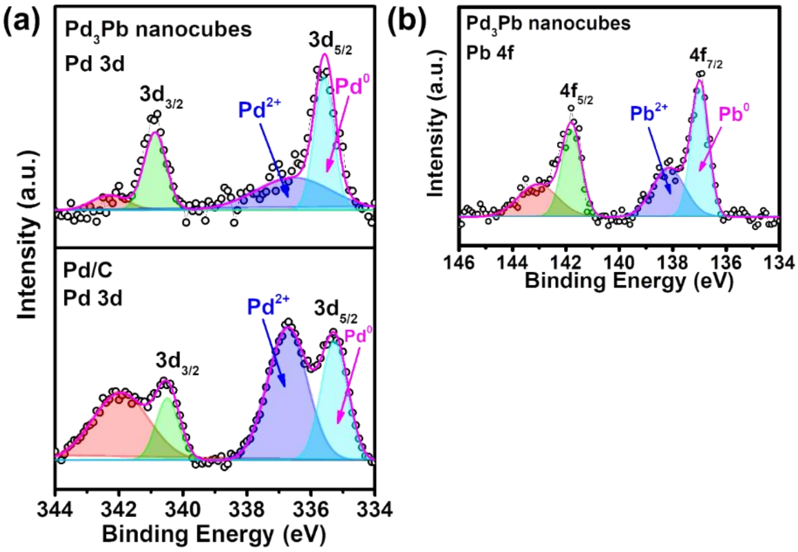

Figure. 11. (a) Pd 3, (b) Pb 4f XPS spectra of the Pd_3Pb nanocubes, and Pd/C, respectively.

To verify the modification of the surface electronic structure of Pd_3Pb NBs, XPS spectra on the Pd 3d and Pb 4f core levels of Pd_3Pb NBs, Pd_3Pb nanocubes, and Pd/C catalysts were additionally obtained

(Fig. 11). XPS spectra of Pd_3Pb NBs and Pd_3Pb nanocubes showed higher Pd 3d binding energies than commercial Pd/C catalysts. The binding energy shifts for Pd demonstrate a change in the Pd electronic structure, which was consistent with the presence of more electronegative Pb than Pd.[39, 50] Furthermore, for a more precise estimation of the d-band shift, valence band regions were obtained, and corresponding d-band center positions relative to the Fermi level were calculated. The d-band center position of Pd_3Pb NBs (–3.807 eV) was lower than those of Pd_3Pb nanocubes (–3.697 eV) and Pd/C catalysts (–3.188 eV), indicating that the binding strength of $(CO)_{ads}$ with the surface of Pd_3Pb NBs is weaker than those of Pd_3Pb nanocubes and Pd/C catalysts, which can account for the more efficient CO removal ability of Pd_3Pb NBs than Pd_3Pb nanocubes and Pd/C catalysts (Fig. 12). In addition, the down-shifted d-band center of Pd_3Pb NBs can accelerate the transformation of $COCH_3$ to CH_3COOH on the catalysts and the rate-determining step of the C2 pathway, thereby boosting the EOR activity.[8, 53, 54] This optimal interaction between intermediates and the surface of Pd_3Pb NBs compared with the surfaces of Pd_3Pb nanocubes and Pd/C catalysts can be attributed to the coexistence of the intermetallic Pd–Pb alloy and low-coordinated surface atoms in Pd_3Pb NBs.[30, 41, 55]

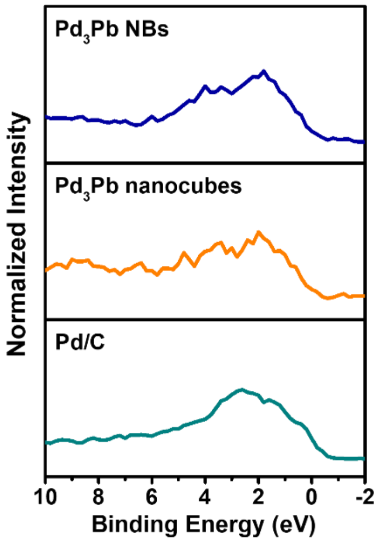

Figure. 12. The valence band spectra of Pd_3Pb NBs, Pd_3Pb nanocubes, and Pd/C.

2.4 Conclusion

In conclusion, a wet-chemical synthesis approach to produce intermetallic Pd_3Pb NBs with multi-branches composed of low-coordinated surface atoms was reported. The control of the growth rate by AA and surface stabilization by NH_4Br is critical for the formation of Pd_3Pb NBs. The prepared Pd_3Pb NBs exhibited excellent electrocatalytic performance toward EOR compared with Pd_3Pb nanocubes and commercial Pd/C catalysts, which can be attributed to their unique morphological properties and intermetallic Pd–Pb compositional structure. This work presents a new design of nanostructures by modifying the morphology and composition for highly active and durable catalysts for fuel cells and beyond.

2.5 References

1. Seh, Z. W.; Kibsgaard, J.; Dickens, C. F.; Chorkendorff, I.; Norskov, J. K.; Jaramillo, T. F. *Science* 2017, 355, (6321), 146-157.

2. Kim, H. C.; Pramadewandaru, R. K.; Lee, S. U.; Hong, J. W. *Bulletin of the Korean Chemical Society* **2020,** 41, (2), 237-240.

3. Guo, S.; Wang, E. *Nano Today* **2011,** 6, (3), 240-264.

4. An, L.; Zhao, T. S.; Chen, R.; Wu, Q. X. *Journal of Power Sources* **2011,** 196, (15), 6219-6222.

5. Huang, W.; Ma, X. Y.; Wang, H.; Feng, R.; Zhou, J.; Duchesne, P. N.; Zhang, P.; Chen, F.; Han, N.; Zhao, F.; Zhou, J.; Cai, W. B.; Li, Y. *Adv Mater* **2017,** 29, (37), 1703057.

6. Zheng, Y.; Wan, X.; Cheng, X.; Cheng, K.; Dai, Z.; Liu, Z. *Catalysts* **2020,** 10, (2), 166-187.

7. Yaqoob, L.; Noor, T.; Iqbal, N. *RSC Adv* **2021,** 11, (27), 16768-16804.

8. Wang, L.; Lavacchi, A.; Bevilacqua, M.; Bellini, M.; Fornasiero, P.; Filippi, J.; Innocenti, M.; Marchionni, A.; Miller, H. A.; Vizza, F. *ChemCatChem* **2015,** 7, (14), 2214-2221.

9. Shen, S.; Guo, Y.; Luo, L.; Li, F.; Li, L.; Wei, G.; Yin, J.; Ke, C.; Zhang, J. *The Journal of Physical Chemistry C* **2018,** 122, (3), 1604-1611.

10. Rizo, R.; Aran-Ais, R. M.; Padgett, E.; Muller, D. A.; Lazaro, M. J.; Solla-Gullon, J.; Feliu, J. M.; Pastor, E.; Abruna, H. D. *J Am Chem Soc* **2018,** 140, (10), 3791-3797.

11. Hien, H. V.; Thanh, T. D.; Chuong, N. D.; Hui, D.; Kim, N. H.; Lee, J. H. *Composites Part B: Engineering* **2018,** 143, 96-104.

12. Kim, H. C.; Kim, Y.; Bando, Y.; Yamauchi, Y.; Hong, J. W. *Journal of Materials Chemistry A* **2019,** 7, (38), 22029-22035.

13. Lee, S.; Cho, H.; Kim, H. J.; Hong, J. W.; Lee, Y. W. *Materials (Basel)* **2021,** 14, (11), 2970.

14. Akhairi, M. A. F.; Kamarudin, S. K. *International Journal of Hydrogen Energy* **2016,** 41, (7), 4214-4228.

15. Karuppasamy, L.; Lee, G.-J.; Anandan, S.; Wu, J. J. *Applied Surface Science* **2020,** 519, 146266.

16. Liu, M.; Xie, M.; Jiang, Y.; Liu, Z.; Lu, Y.; Zhang, S.; Zhang, Z.; Wang, X.; Liu, K.; Zhang, Q.; Cheng, T.; Gao, C. *Journal of Materials Chemistry A* **2021,** 9, (27), 15373-15380.

17. Xie, S.; Choi, S.-I.; Xia, X.; Xia, Y. *Current Opinion in Chemical Engineering* **2013,** 2, (2), 142-150.

18. Kabiraz, M. K.; Kim, J.; Choi, S. I. *Bulletin of the Korean Chemical Society* **2020,** 42, (5), 802-805.

19. Kabiraz, M. K.; Kim, H. J.; Hong, Y.; Chang, Q.; Choi, S. I. *Bulletin of the Korean Chemical Society* **2022,** 43, (9), 1093-1097.

20. John Watt, S. C., Michael F. Toney, Bridget Ingham, James Cookson, Peter T. Bishop, and Richard D. Tilley. *ACS Nano* **2009,** 4, (1), 396-402.

21. Hu, T.; Wang, Y.; Xiao, H.; Chen, W.; Zhao, M.; Jia, J. *Chem Commun (Camb)* **2018,** 54, (95), 13363-13366.

22. Zhang, J.; Ye, J.; Fan, Q.; Jiang, Y.; Zhu, Y.; Li, H.; Cao, Z.; Kuang, Q.; Cheng, J.; Zheng, J.; Xie, Z. *J Am Chem Soc* **2018,** 140, (36), 11232-11240.

23. Poerwoprajitno, A. R.; Gloag, L.; Benedetti, T. M.; Cheong, S.; Watt, J.; Huber, D. L.; Gooding, J. J.; Tilley, R. D. *Small* **2019,** 15, (17), e1804577.

24. Cai, Y.; Ma, C.; Zhu, Y.; Wang, J. X.; Adzic, R. R. *Langmuir* **2011,** 27, (13), 8540-8547.

25. Peng, H.; Ren, J.; Wang, Y.; Xiong, Y.; Wang, Q.; Li, Q.; Zhao, X.; Zhan, L.; Zheng, L.; Tang, Y.; Lei, Y. *Nano Energy* **2021,** 88, 106307.

26. Wu, T.; Sun, M.; Huang, B. *Angew Chem Int Ed Engl* **2021,** 60, (42), 22996-23001.

27. Lim, B.; Xia, Y. *Angew Chem Int Ed Engl* **2011,** 50, (1), 76-85.

28. Graham, L.; Collins, G.; Holmes, J. D.; Tilley, R. D. *Nanoscale* **2016,** 8, (5), 2867-74.

29. Poerwoprajitno, A. R.; Cheong, S.; Gloag, L.; Gooding, J. J.; Tilley, R. D. *Acc Chem Res* **2022,** 55, (12), 1693-1702.

30. Wang, Y.; Nguyen, T. S.; Liu, X.; Wang, X. *Journal of Power Sources* **2010,** 195, (9), 2619-2622.

31. Lao, X.; Yang, M.; Chen, J.; Zhang, L. Y.; Guo, P. *Electrochimica Acta* **2021,** 374, 137912.

32. Hong, Y.; Kim, H. J.; Lee, H. J.; Kim, J.; Choi, S. I. *Front Chem* **2019,** 7, 608.

33. Liu, D.; Zeng, Q.; Liu, H.; Hu, C.; Chen, D.; Xu, L.; Yang, J. *Cell Reports Physical Science* **2021,** 2, (3), 100357.

34. Han, Y.; Kim, J.; Lee, S. U.; Choi, S. I.; Hong, J. W. *Chem Asian J* **2020,** 15, (8), 1324-1329.

35. Luo, M.; Sun, Y.; Wang, L.; Guo, S. *Advanced Energy Materials* **2017,** 7, (11), 160273.

36. Kim, K. S.; Hong, Y.; Kim, H. C.; Choi, S. I.; Hong, J. W. *Chemistry* **2019,** 25, (29), 7185-7190.

37. Kim, H. J.; Ahn, Y.-D.; Kim, J.; Kim, K.-S.; Jeong, Y. U.; Hong, J. W.; Choi, S.-I. *Chinese Journal of Catalysis* **2020,** 41, (5), 813-819.

38. Furukawa, S.; Komatsu, T. *ACS Catalysis* **2016,** 7, (1), 735-765.

39. Li, J.; Sun, S. *Acc Chem Res* **2019,** 52, (7), 2015-2025.

40. Gamler, J. T. L.; Ashberry, H. M.; Skrabalak, S. E.; Koczkur, K. M. *Adv Mater* **2018**, e1801563.

41. Guo, J.; Gao, L.; Tan, X.; Yuan, Y.; Kim, J.; Wang, Y.; Wang, H.; Zeng, Y. J.; Choi, S. I.; Smith, S. C.; Huang, H. *Angew Chem Int Ed Engl* **2021,** 60, (19), 10942-10949.

42. Kim, H. Y.; Kim, J. Y.; Joo, S. H. *Bulletin of the Korean Chemical Society* **2021,** 42, (5), 724-736.

43. Yu, X.; Luo, Z.; Zhang, T.; Tang, P.; Li, J.; Wang, X.; Llorca, J.; Arbiol, J.; Liu, J.; Cabot, A. *Chemistry of Materials* **2020,** 32, (5), 2044-2052.

44. Du, W.; Mackenzie, K. E.; Milano, D. F.; Deskins, N. A.; Su, D.; Teng, X. *ACS Catalysis* **2012,** 2, (2), 287-297.

45. Wu, P.; Huang, Y.; Zhou, L.; Wang, Y.; Bu, Y.; Yao, J. *Electrochimica Acta* **2015,** 152, 68-74.

46. Zhao, Y.; Tao, L.; Dang, W.; Wang, L.; Xia, M.; Wang, B.; Liu, M.; Gao, F.; Zhang, J.; Zhao, Y. *Small* **2019,** 15, (17), e1900288.

47. Wahidah, H.; Hong, J. W. *Bulletin of the Korean Chemical Society* **2022,** 43, (9), 1111-1117.

48. Li, R.; Hao, H.; Cai, W.-B.; Huang, T.; Yu, A. *Electrochemistry Communications* **2010,** 12, (7), 901-904.

49. Gunji, T.; Noh, S. H.; Tanabe, T.; Han, B.; Nien, C. Y.; Ohsaka, T.; Matsumoto, F. *Chemistry of Materials* **2017,** 29, (7), 2906-2913.

50. Michèle Besson, P. G. *Catalysis Today* **2000,** 57, 127-141.

51. Bhalothia, D.; Huang, T. H.; Chou, P. H.; Wang, K. W.; Chen, T. Y. *RSC Adv* **2020,** 10, (29), 17302-17310.

52. Garcia, A. C.; Birdja, Y. Y.; Tremiliosi-Filho, G.; Koper, M. T. M. *Journal of Catalysis* **2017,** 346, 117-124.

53. Yang, Y.-Y.; Ren, J.; Li, Q.-X.; Zhou, Z.-Y.; Sun, S.-G.; Cai, W.-B. *ACS Catalysis* **2014,** 4, (3), 798-803.

54. Zhang, Z.; Xin, L.; Sun, K.; Li, W. *International Journal of Hydrogen Energy* **2011,** 36, (20), 12686-12697.

55. Greeley, J.; Nørskov, J. K. *Surface Science* **2005,** 592, (1-3), 104-111.

Chapter 3. Size-Dependent Catalytic Performance of Ruthenium on Pd_3Pb Nanowires: Unveiling the Role of Single Atoms, Clusters, and Nanoparticles in the Hydrogen Evolution Reaction

3.1 Introduction

The production of alternative energy, which is environmentally benign, has been widely pursued in an effort to reduce the energy scarcity generated by the continuous use of fossil fuels. Among these alternatives, the development and utilization of hydrogen energy are promising due to its inherent qualities, such as cleanliness, high energy density, affordability, and sustainability.[1-3] The hydrogen evolution reaction (HER) in an alkaline medium is one of the practical techniques for hydrogen generation due to the significant amount of water electrolysis it produces.[4-6] Since the electrocatalytic HER has drawbacks of sluggish reaction kinetics and large overpotential, it is crucial to develop ideal catalysts to accelerate hydrogen evolution and reduce overpotential.

Platinum-based catalysts are generally regarded as the best catalysts for HER and provide sufficient reaction rates due to the optimum adsorption energy between the catalysts' surface and H_{ads}. However, the general application of Pt is severely constrained by its restricted availability, high material cost, and poor electrochemical stability under severe redox conditions.[7-9] In particular, Ru-based electrocatalysts have drawn a lot of attention as a benchmark for HER because of their low cost, similar properties to Pt, ability to decrease the reaction barrier of the rate-determining step by weakening the hydrogen-binding energy, and promotion of OH adsorption during HER.[10-13]

The atomic utilization efficiency offered by Ru single-atom catalysts and Ru nanoparticles has recently received considerable attention as cost-effective catalysts.[12-15] Additionally, Ru atoms can offer an inherent advantage through strong interaction with their support, modifying the electronic structure and contributing to enhanced electrocatalytic activity and stability. An ideal support material for highly dispersed Ru atoms is needed since surface atoms are crucial to the catalytic process. To this end, various supports have been extensively reported for anchoring Ru atom in single atom and nanopartilces structures, such as transition metal chalcogenides (TMCs), transition metal phosphides (TMPs), carbon materials, MXenes, metal-organic frameworks (MOFs), and transition metal-based layered metal hydroxides (LMHs).[16-18] To the best of our knowledge, intermetallic nanocrystals (NCs) have yet to be studied as supports among the different options. Intermetallic NCs have demonstrated interesting properties due to their ordered atomic arrangement, which is generally more stable and prevents etching during electrocatalytic reactions.[19-21] In general, intermetallic NCs with well-defined morphologies are highly desirable as efficient supports for anchoring Ru atoms. Among the several intermetallic NC topologies, one-dimensional (NW) nanowires are regarded as one of the most promising Ru atoms support materials due to their composition of low-coordinated surface atoms such as ledges, steps, and kink atoms on the edges of NWs.[22-25] These atoms can increase the number of active catalytic sites and accelerate the adsorption and desorption of reagents and intermediates during HER.

In this study, the incorporation of a Ru atoms with different concentration can produced in different structures including, Ru single atom, Ru clusters, and Ru nanoparticles was successfully anchored on intermetallic Pd_3Pb NWs (denoted as Pd_3Pb-Ru_X NWs (X: S, C, and N)) via a facile synthetic method. The intermetallic Pd_3Pb NWs were selected as the substrate because of their atomic configuration and possession of low-coordinated surface atoms, which are favorable for HER activity. The Ru single atom delivered a lower overpotential of 13 mV at 10 mA cm^{-2} compared to Pt/C (45 mV) and possessed a lower Tafel slope of 31 mV dec^{-1} to Pt/C (50 mV dec^{-1}). Furthermore, the long-term stability test after 10,000 cycles of Pd_3Pb-Ru_S NWs exhibited slight potential losses (5 mV) without significant change, confirming highly stable catalysts for HER. This study paves the way for the development of novel electrocatalysts with enhanced activity and stability by shedding light on the function of size-dependent Ru atoms anchoring on intermetallic Pd_3Pb NWs.

3.2 Experimental Section

3.2.1 Chemical and Materials

Palladium(II) acetylacetonate ($Pd(acac)_2$, 99%), ammonium bromide (NH_4Br, 99.0%), Benzyl ether (98%), cetyltrimethylammonium chloride solution (CTAC, 25 wt% in H2O), hydrazine hydrate (50-60%), sodium borohydride ($NaBH_4$, 99%), isopropanol (9.9%) and Nafion perfluorinated resin solution (5 wt%) were obtained from Sigma-Aldrich. Oleylamine (OAm, 50%) was obtained from TCI chemical.

Lead(II) 2,4-pentanedionate (Pb(acac)$_2$, 99%), (1-Hexadecyl)trimethylammonium bromide (CTAB, 98%) and commercial Pd/C (30 wt%) were obtained from Alfa aesar. Chloroform ($CHCl_3$) was obtained from Daejung chemical. Potassium hydroxide (KOH, 95.0%) was obtained from Samchun. Other chemicals were reagent grade, and deionized water with a resistivity of greater than 18.3 MΩ·cm was used in the preparation of reaction solutions. Hexane was of technical grade.

3.2.2 Synthesis of Pd_3Pb NWs

15 mL of OAm was preheated from RT to 100^{o}C for 30 min (as solution A). In another vial, 0.3 mmol of Pd(acac)$_2$, 0.1 mmol of Pb(acac)$_2$, 125 mg of NH_4Br, and 5 mL of OAm were mixed in a 30 mL vial. The mixture was sonicated until it dissolved, then the glass vial was transferred into the water bath and heated at 80^{o}C for 30 min (as solution B). After 30 min, solution B was rapidly injected into solution A. Temperature was increased from 100^{o}C to 150^{o}C for 30 min and kept reaction at 150^{o}C for 6 h. The solution was washed with a mixture of hexane and ethanol (1:1) several times.

3.2.3 Synthesis of Ru decorations on Pd_3Pb NWs

As prepared 30 mg of Pd_3Pb NWs, 15 mL of OAm, and 15 mL of benzyl ether were added to a round bottom flask with a magnetic bar. The mixture was heated to 250^{o}C under an N_2 atmosphere. After the temperature reached 250^{o}C, different concentration of Ru(acac)$_3$ dissolved in 5 mL of benzyl ether was injected into the reaction mixture. The concentrations were 0.18 mM for Ru single atom, 0.35 mM for Ru clusters, and 1.075 mM for Ru nanoparticles. Then, the reaction mixture was maintained at 250^{o}C for 1 h. The final product was cooled down to room temperature and then washed with toluene and ethanol (1:1) three times.

3.2.4 Transfer Hydrophobic Pd_3Pb NWs to Hydrophilic Solution

As prepared Pd3Pb NWs, the product was dispersed in 5 mL of $CHCl_3$ to form a homogeneous colloidal dispersion. The aforementioned Pd_3Pb NWs colloid solution was added to 50 mL of CTAB (100 mM). The mixture was ultrasonicated to form a stable white or grey emulsion. After that, the stable emulsion was placed in an oil bath at 80^{o}C with vigorous stirring for 30 min. The solution was collected in a 70 mL vial and left undisturbed overnight. Remove the supernatant and re-disperse the product with 15 mL of CTAC (100 mM).

3.2.5 Separation Method of Pd_3Pb NWs and nanocubes

15 mL of $NaBH_4$ (250 mM) was added into the re-dispersed Pd_3Pb NWs and nanocubes in CTAC solution in an ice bath and left undisturbed for 30 min. Remove the supernatant and re-disperse the product with 15 mL of CTAC (100 mM). 15 mL of hydrazine hydrate (100 mM) was added into the aforementioned solution and then placed in an oven at 60^{o}C for 12 h. Then, remove the supernatant and wash with DIW several times.

3.2.6 Electrochemical Measurements

Electrochemical measurements were carried out using EC-Lab Biologic Model SP-300 electrochemical workstation in a standard three-electrode system. Graphite was employed as the counter electrode and a Hg/HgO (1 M KOH) electrode served as the reference electrode. The Pd_3Pb NWs and $Pd_3Pb\text{-}Ru_X$ NWs were loaded onto a carbon support (Vulcan XC 72R) before estimating their electrocatalytic properties. Catalyst ink was prepared by dispersing certain amounts of catalysts in a mixture of 2-propanol, deionized water (DIW), and Nafion (5 wt.%) with a ratio of 4:1: 0.025 to make a catalyst ink of 4 μg_{metal} μL^{-1}. For the preparation of the working electrode, 10 μL of catalyst ink was applied to carbon electrode (1 cm^2) and allowed to dry naturally at room temperature. The precise amount of metal loaded on the carbon plate elecrode was determined by inductively coupled plasma-optical emission spectroscopy (ICP-OES). All potentials were converted with respect to a reversible hydrogen electrode (RHE) in Ar-saturated 1.0 MKOH. Prior to recording LSV curves, CV was conducted at scan rates of 50 mVs^{-1}, ranging from 0.1 to 1.3 V (vs. RHE) until CV curves were stabilized. For HER experiments, LSV curves were obtained at a scan rate of 5 mVs^{-1}. EIS measurements were conducted at –200 mV (vs. RHE) over a frequency range from 1 to 10 MHz.

3.2.7 Characterization

Transmission electron microscopy (TEM) and scanning electron microscopy (SEM) images of the prepared catalysts were obtained by using a JEOL JEM-2100F and a JEOL JEM-7210F, respectively. SEM analysis was done by using (used instrument) at total-period analysis center for Ulsan chemical industry of Korea Basic Science Institute (KBSI). ICP-OES measurement was conducted using a Spectrouble-ICP-OES (Ametek). X-ray diffraction (XRD) measurement was conducted on a Rigaku D/MAX2500V/PC. X-ray photoelectron spectroscopy (XPS) measurements were conducted using a Thermo VG Scientific Sigma Probe spectrometer with Al Kα X-ray (1486.6 eV) as a light source. XPS data were calibrated using the C 1 s peak at 284.5 eV.

3.3 Result and Discussion

3.3.1 Synthesis mechanism and characterization of Ru decorations on Pd_3Pb NWs

The synthetic procedure for Pd_3Pb-Ru_X NWs is illustrated in Figure 1. First, the intermetallic Pd_3Pb NWs were synthesized through a facile route using Palladium(II) acetylacetonate and Lead(II) acetylacetonate as the metal precursors, oleylamine (OAm) as a surfactant, and NH_4Br as a shape controller. The formation of NWs depends on the reduction rate of the precursors. Thus, OAm also acts as a reductant to maintain a slow reduction rate during the reaction. During the synthesis of intermetallic Pd_3Pb NWs, nanocubes were also produced, presenting an obstacle (Figure 2a). To increase the yield of nanowires, a separation method was employed. Based on their morphology, NWs are larger than nanocubes, indicating that NWs are heavier. Therefore, the removal of nanocubes was based on the weight of the nanoparticles. The initial step involved a change in the solution phase from hydrophobic to hydrophilic. The hydrophilic phase was then functionalized using a cationic surfactant (CTAC) and strong reducing agents ($NaBH_4$ and hydrazine hydrate) to separate the NWs from the nanocubes.[26] As a result, the NWs precipitated, while the solution contained the nanocubes (Figure 2b-c). Subsequently, the aforementioned solution was discarded, and the precipitate, which contained a high yield of nanowires, was redispersed in a CTAC solution to prevent nanoparticle aggregation. After the separation process, the different concentration of Ruthenium(III) acetylacetonate were added to the organic mixture containing Pd_3Pb NWs to generate the Pd_3Pb-Ru_X NWs.[27] There are three types of Ru decoration on Pd_3Pb NWs: with low concentration, denoted as Ru single atom (Pd_3Pb-Ru_S NWs); at medium concentration, denoted as Ru clusters (Pd_3Pb-Ru_C NWs); and at high concentration, denoted as Ru nanoparticles (Pd_3Pb-Ru_N NWs).

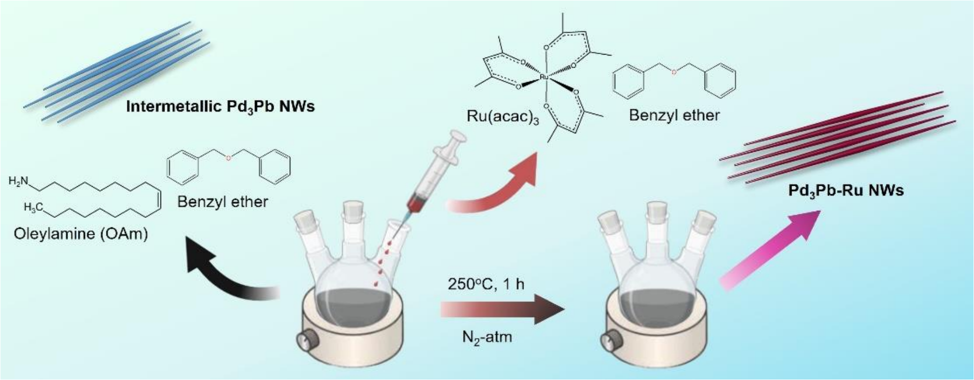

Figure 1. Schematic illustration of the fabrication of Pd_3Pb-Ru NWs

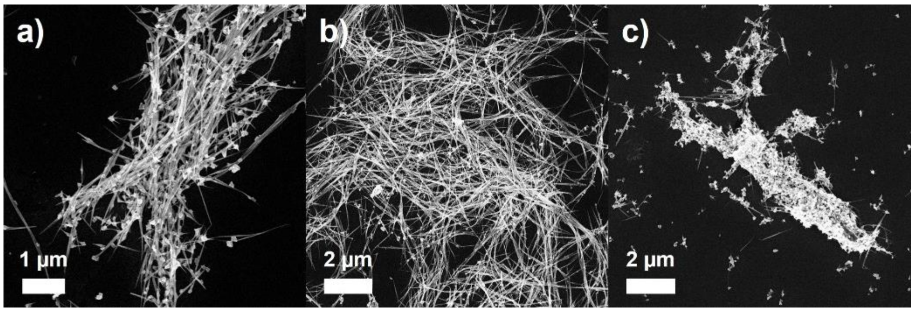

Figure 2. SEM images of Pd_3Pb NWs a) before and b-c) after separation method.

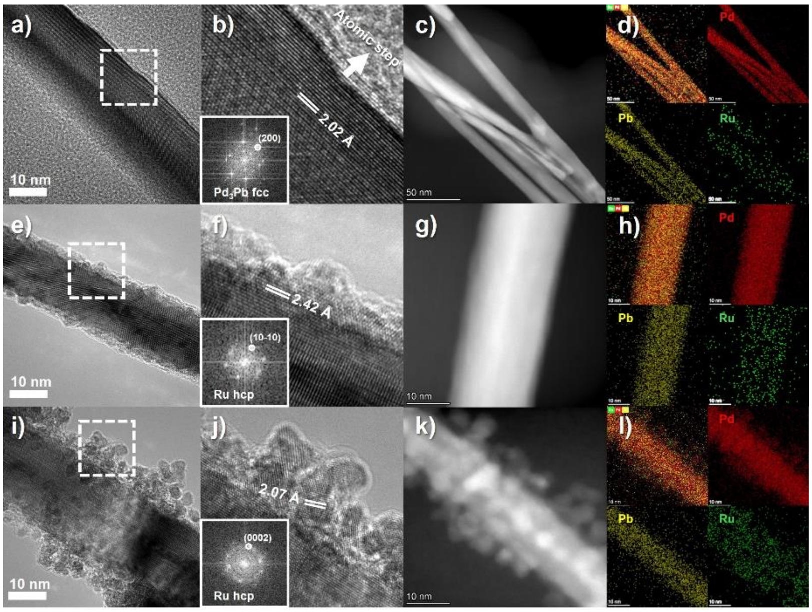

Figure 3. HAADF-STEM images of a-b) Pd_3Pb-Ru_S NWs, e-g) Pd_3Pb-Ru_C NWs, i-j) Pd_3Pb-Ru_N NWs, HAADF-STEM images of c) Pd_3Pb-Ru_S NWs, g) Pd_3Pb-Ru_C NWs, k) Pd_3Pb-Ru_N NWs, EDS elemental mapping images of Pd, Pb, Ru in d) Pd_3Pb-Ru_S NWs, h) Pd_3Pb-Ru_C NWs, and l) Pd_3Pb-Ru_N NWs.

The high-resolution transmission electron microscopy (HR-TEM) images of various Ru decorations on Pd_3Pb NWs are shown in Figure 3. These confirm that varying concentrations of Ru can alter the morphology of Ru anchoring on Pd_3Pb NWs. Figure 3a-b displays a TEM image of Ru single atoms anchored on Pd_3Pb NWs, showing a smooth surface on the NWs. Additionally, increasing the concentration of Ru to 0.35 mM leads to the formation of clusters on the surface of Pd_3Pb NWs. Meanwhile, increasing the concentration to 1.075 mM results in the production of Ru nanoparticles, with sizes around 3.18 ± 0.47 nm, on the surface of Pd_3Pb NWs. Furthermore, the elemental mapping of Ru decorations on Pd_3Pb NWs, obtained through high-angle annular dark-field scanning TEM combined with energy-dispersive X-ray spectroscopy (HAADF-STEM-EDS), demonstrates that the Ru atoms are distributed and show an increasing atomic ratio with increased Ru concentrations (Figure 3d,h,l and Table 1). The observed variations in the morphological and atomic distribution characteristics of Ru-decorated Pd_3Pb NWs, as evidenced by TEM imaging and elemental mapping, underscore the precise control achievable over the nanoscale structural features through the careful adjustment of Ru precursor concentrations. This control over structural attributes not only highlights the versatile nature of the synthesis approach but also suggests potential pathways for tuning the catalytic properties of the resulting nanomaterials for targeted applications.

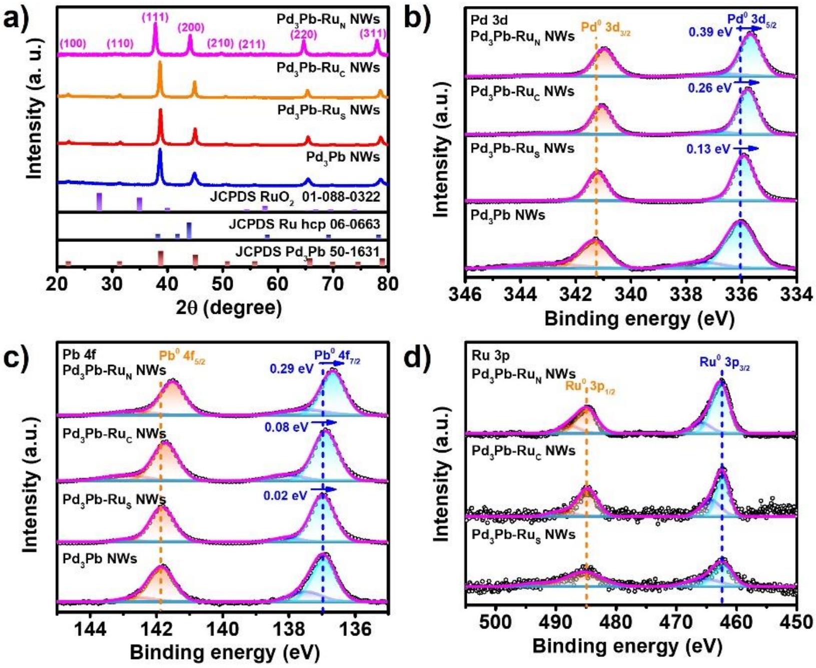

Figure 4. a) XRD of all catalysts, XPS peaks of b) Pd 3d, c) Pb 4f, and d) Ru 3p of all catalysts.

The crystal structure of Ru decorations on Pd_3Pb NWs, as well as the structure of Pd_3Pb NWs alone, was analyzed using X-ray diffraction (XRD). The XRD pattern, shown in Figure 4a, displays a series of peaks corresponding to the (100), (110), (210), (211), (221), and (310) planes, validating the presence of the intermetallic Pd_3Pb phase (Pm^{-}3m, a = 4.035 Å, JCPDS No. 50-1631). The absence of diffraction peaks associated with Ru species in Pd_3Pb-RuS NWs and Pd_3Pb-Ru_C NWs suggests that Ru is present in low quantities and is anchored on the surface of the intermetallic Pd_3Pb NWs. Additionally, the XRD pattern of Pd_3Pb-Ru_N NWs is slightly shifted to a lower degree, indicating that the presence of Ru nanoparticles might enlarge the Pd-Pb crystal lattice. Thus, XRD analysis confirms the successful incorporation and impact of Ru decorations on the crystalline structure of Pd_3Pb NWs, with variations in Ru content leading to distinct structural modifications.

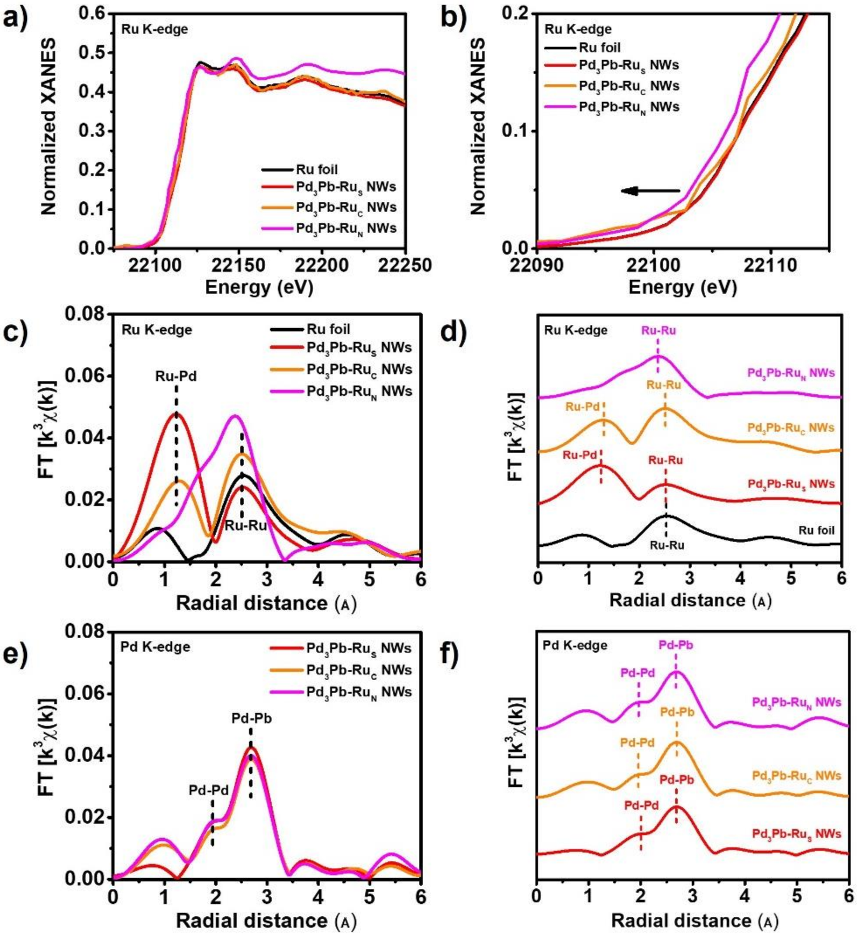

Figure 5. a) Ru K-edge XANES spectra of Ru foil, Pd_3Pb-Ru_S NWs, Pd_3Pb-Ru_C NWs, and Pd_3Pb-Ru_N NWs, b) high-resolution of Ru K-edge XANES spectra, c-d) Fourier-transformed Ru k-edge EXAFS spectra of Ru foil, Pd_3Pb-Ru_S NWs, Pd_3Pb-Ru_C NWs, and Pd_3Pb-Ru_N NWs, and e-f) Fourier-transformed Pd k-edge EXAFS spectra of Ru foil, Pd_3Pb-Ru_S NWs, Pd_3Pb-Ru_C NWs, and Pd_3Pb-Ru_N NWs.

X-ray photoelectron spectroscopy (XPS) was employed to examine the surface electronic states and chemical valence of the catalysts. As illustrated in Figure 4b, the Pd 3d peaks of Pd_3Pb-Ru_S NWs, Pd_3Pb-Ru_C NWs, Pd_3Pb-Ru_N NWs, and Pd_3Pb NWs were observed, with the main peaks of Pd 3d in Ru-decorated samples shifting to lower binding energies compared to those in Pd_3Pb NWs. A similar trend was seen for the Pb 4f peak of Ru-decorated Pd_3Pb NWs, which also shifted to lower binding energies relative to Pd_3Pb NWs. Conversely, the Ru 3p peak in Figure 3d for Ru-decorated Pd_3Pb NWs shifted to a higher binding energy compared to Ru reference, suggesting electron transfer from the Ru atoms to the Pd_3Pb support.[28-30] The observed shifts in binding energy for Pd 3d and Pb 4f peaks signify modifications in the surface electronic structure and chemical valence of the catalysts due to Ru decoration, indicative of an interplay between the Pd_3Pb matrix and Ru atoms that facilitates electron redistribution.

Table 1. EDS ratio of Pd_3Pb-Ru_S NWs, Pd_3Pb-Ru_C NWs, and Pd_3Pb-Ru_N NWs.

Catalyts	**Atomic %**			**Ratio**		
	Pd	**Pb**	**Ru**	**Pd**	**Pb**	**Ru**
Pd_3Pb-Ru_S NWs	72.22	23.55	4.23	3.5	1	0.10
Pd_3Pb-Ru_C NWs	71.96	20.49	7.55	3.5	1	0.36
Pd_3Pb-Ru_N NWs	61.29	19.72	18.98	3.1	1	0.95

To explore the influence of surface structure and the bonding environment arising from size-dependent Ru modifications on Pd_3Pb NWs, we employed the X-ray absorption near edge structure (XANES) technique. The Ru K-edge XANES spectra of Ru-decorated Pd_3Pb NWs, displayed in Figure 5a, when compared to Ru foil, indicates that the pre-edge spectra of the Pd_3Pb-Ru catalysts possess binding energies akin to those of Ru foil. This similarity suggests the formation of an oxidation state comparable to metallic Ru.[15, 31, 32] A further investigation into the bonding environment of Ru, Pd, and Pb using Fourier transform extended X-ray absorption fine structure (FT-EXAFS) at the Ru K-edge and Pd K-edge revealed insightful details. The FT-EXAFS of the Ru K-edge for the Pd_3Pb-Ru catalysts highlighted peaks corresponding to Ru-Pd interactions at approximately 1.37 Å and a Ru-Ru bond at about 2.5 Å. The Pd_3Pb-Ru_S NWs demonstrated a higher intensity for the Ru-Pd bond, whereas the

Pd_3Pb-Ru_C NWs exhibited a more pronounced Ru-Ru peak than Ru-Pd. This suggests that an increase in Ru size modifies Ru cluster formation. Furthermore, the Pd_3Pb-Ru_N NWs exclusively showed the Ru-Ru peak, indicating robust interactions between Ru metal and the Pd_3Pb support. The FT-EXAFS of the Pd K-edge for the Pd_3Pb-Ru catalysts revealed two peaks, corresponding to the Pd-Pd bond at approximately 2.0 Å and the Pd-Pb bond at about 2.67 Å. These findings suggest that Ru incorporation does not disrupt the lattice structure of Pd_3Pb nor alter the local Pd environment, positing that Ru atoms are likely located on the surface of the Pd_3Pb support with strong interactions with Pd atoms rather than with Pb atoms. The similarity in properties between Ru and Pd, such as electronegativity and atomic size, likely facilitates the high dispersion of Ru on the Pd surface. In this study provides a detailed analysis of the surface structure and bonding environments of size-modified Ru on Pd_3Pb NWs, highlighting the crucial role of Ru modifications in influencing the catalytic properties and interactions within the alloy. The insights gained from the XANES and FT-EXAFS characterizations underline the potential of tailoring the nanostructure features of bimetallic for enhanced catalytic performance, especially in applications like hydrogen evolution reactions.

3.3.2 Electrocatalytic properties for efficient HER in alkaline medium

The electrocatalytic HER performances of the catalysts were evaluated in a typical three-electrode system with N_2-saturated 1.0 M KOH as the electrolyte. The HER performances of Pd_3Pb-Ru_S NWs, Pd_3Pb-Ru_C NWs, Pd_3Pb-Ru_N NWs, Pd_3Pb NWs, and Pt/C, were investigated using linear sweep voltammetry (LSV) at a scan rate of 5 mV s^{-1}, as demonstrated in Figure 6a. The comparison of overpotential at 10 and 100 mA cm^{-2} of all catalysts is displayed in Figure 6b. The overpotential of Pd_3Pb-Ru_S NWs is substantially lower (13 mV) than that of Pd_3Pb-Ru_C NWs (31 mV), Pd_3Pb-Ru_N NWs (75 mV), Pd_3Pb NWs (80 mV), and Pt/C (45 mV) at 10 mA cm^{-2}. The Tafel slopes (Figure 6c) of Pd_3Pb-Ru_S NWs, Pd_3Pb-Ru_C NWs, Pd_3Pb-Ru_N NWs, Pd_3Pb NWs, and Pt/C are 31, 40, 45, 47, and 50 mV dec^{-1}, respectively. Interestingly, Pd_3Pb-Ru_S NWs exhibit comparable HER overpotential to Ru-based catalysts reported in previous literature (Figure 6e; Table 2). The Tafel slope value of Pd_3Pb-Ru_S NWs follows the Volmer-Tafel mechanism. The lower overpotential and smaller Tafel slope value of Pd_3Pb-

Ru_S NWs imply enhanced reaction kinetics compared to their counterparts. The HER activity depends on the size of Ru atoms decorated on the intermetallic Pd_3Pb NWs. Single atoms, clusters, and nanoparticles of Ru influenced the overall activities. However, the high dispersion of Ru single atom is the main factor accelerating the HER performance, suggesting that Ru serves as active sites in the HER. Downsizing Ru size leads to an increase in the active sites for HER reactions.[33-35] Additionally, the enhancement of HER activity is attributed to the shape of NWs, providing more active sites due to low-coordination surface atoms.

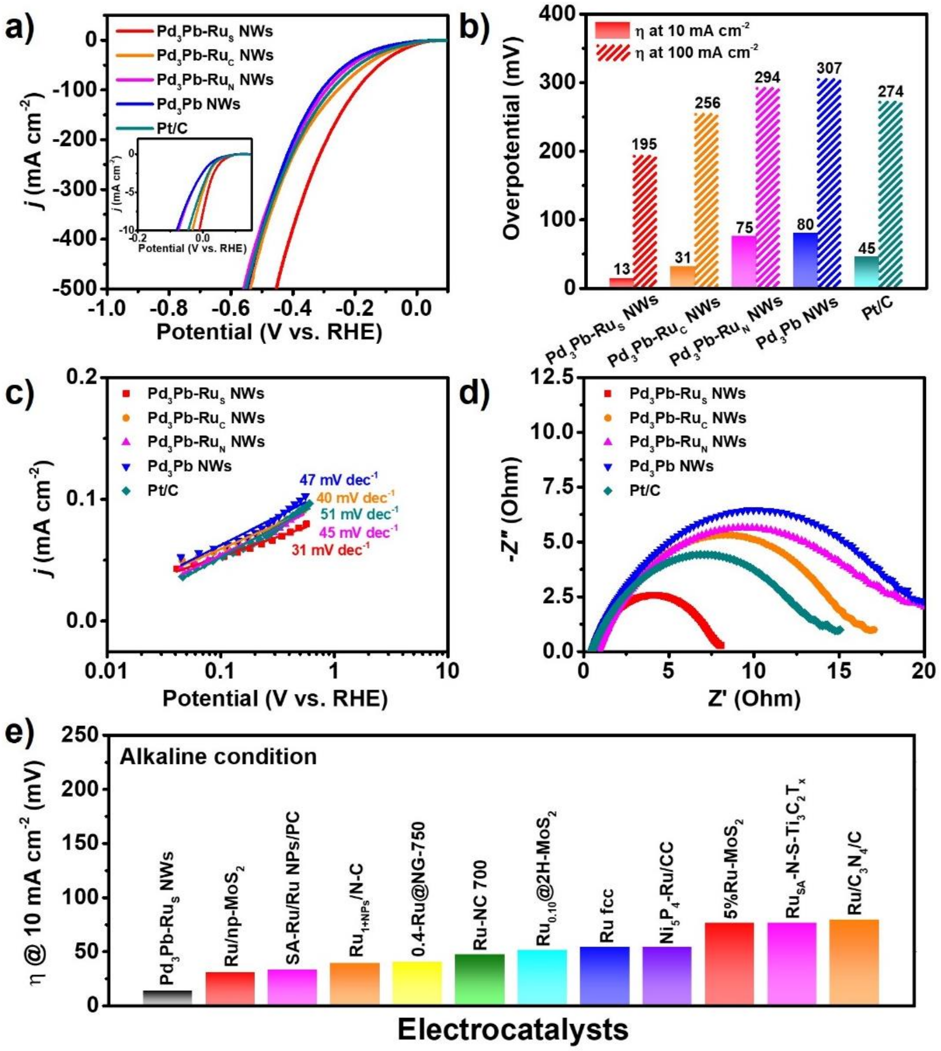

Figure 6. HER polarization curve of all catalysts in 1 M KOH a) at 500 mA cm^{-2}, b) comparing overpotential at 10 and 100 mA cm^{-2} of all catalysts, c) Tafel plots, d) Nyquist plots for various catalysts in 1.0 M KOH at 0.02 V vs RHE, and e) comparing overpotential at 10 mA cm^{-2} of all reported catalysts.

Table 2. The HER catalytic performance comparison between the Pd_3Pb-Ru NWs and previous reports.

No	**Catalysts**	**Overpotential at 10 mA cm^{-2}**	**Tafel slope**	**References**
1	**Pd_3Pb-Ru_S NWs**	13 mV	31 mV dec^{-1}	**This work**
2	**Ru_{SAs}–SnO_2/C**	10 mV	25 mV dec^{-1}	Angew. Chem., 2022, 134, e202209486
3	**Ru@MWCNT**	17 mV	27 mV dec^{-1}	Nat. Commun., 2020, 11, 1278
4	**Ru_1/D–NiFe LDH**	18 mV	29 mV dec^{-1}	Nat. Commun., 2021, 12, 4587
5	**Ru_{SA+NP}/DC**	18.8 mV	35.8 mV dec^{-1}	Adv. Sci., 2021, 8, 2004516
6	**Ru/np–MoS_2**	30 mV	31 mV dec^{-1}	Nat. Commun., 2021, 12, 1687
7	**SA–Ru/Ru NPs/PC**	33 mV	31.8 mV dec^{-1}	J. Mater. Chem. A, 2019, 7, 19531–19538
8	**Ru_{1+NPs}/N–C**	39 mV	27.6 mV dec^{-1}	ACS Appl. Mater. Interfaces, 2022, 14, 15250–15258
9	**0.4–Ru@NG–750**	40 mV	35.9 mV dec^{-1}	ACS Catal., 2019, 9, 9897–9904
10	**Ru–NC 700**	47 mV	14 mV dec^{-1}	Nat. Commun., 2019, 10, 631
11	**$Ru_{0.10}$@2H–MoS_2**	51 mV	64.9 mV dec^{-1}	Appl. Catal. B: Environ., 2021, 298, 120490
12	**Ru fcc**	54 mV	28 mV dec^{-1}	Catal. Sci. Technol., 2022, 12, 3606–3613
13	**Ni_5P_4–Ru/CC**	54 mV	56.7 mV dec^{-1}	Adv. Mater., 2020, 32, 1906972
14	**5%Ru–MoS_2**	76 mV	21 mV dec^{-1}	Small Methods, 2019, 1900653
15	**Ru_{SA}–N–S–$Ti_3C_2T_x$**	76 mV	90 mV dec^{-1}	Adv. Mater., 2019, 31, 1903841
16	**Ru/C_3N_4/C**	79 mV	–	J. Am. Chem. Soc., 2016, 138, 16174

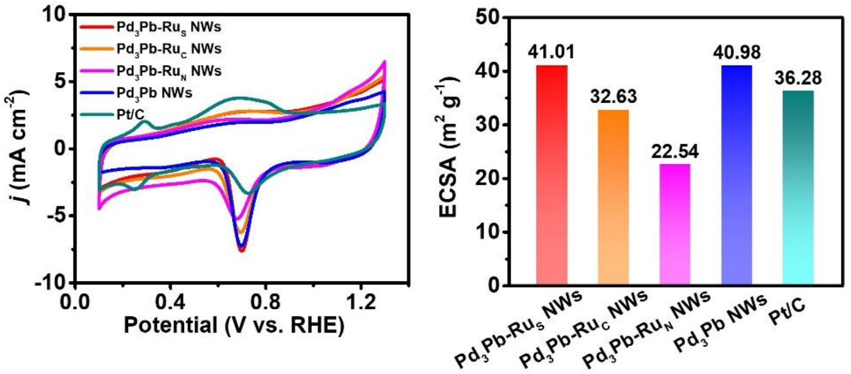

Figure 7. a) CV of all catalysts, and b) ECSA graph of all catalysts.

The electrochemical impedance spectroscopy (EIS) spectra of the catalysts were obtained in N_2-saturated 1.0 M KOH. The charge transfer resistance of Pd_3Pb-Ru_S NWs was significantly lower than that of Pd_3Pb-Ru_C NWs, Pd_3Pb-Ru_N NWs, Pd_3Pb NWs, and Pt/C catalysts, indicating that Pd_3Pb-Ru_S NWs have a faster charge transfer rate to enhance HER activity. These results show that after the incorporation of Ru, the Rct curves decreased, proving that Ru atoms can regulate the charge distribution on intermetallic Pd_3Pb NWs support, hence improving the electronic conductivity on the interface and enhancing the activity of the catalysts.

Furthermore, the electrochemically active surface area (ECSA) of all catalysts, determined by integrating the Coulombic charge for the reduction of oxygen species in cyclic voltammetries (CVs) of the catalysts (Figure 7), showed a decline with increasing Ru size, except for Pt/C, which was determined by the H_{upd} region. The ECSA values for Pd_3Pb-Ru_S NWs, Pd_3Pb-Ru_C NWs, and Pd_3Pb-Ru_N NWs were 40.01, 32.63, and 22.54 m^2 g^{-1}, respectively, indicating that Ru can alter the electronic interaction between Pd, Pb, and Ru. Additionally, the increasing size of Ru blocks the active sites on Pd, leading to a decrease in ECSA. In contrast, the ECSA of Pd_3Pb NWs exhibited a slightly higher value of 40.98 m^2 g^{-1} compared to Pt/C (36.28 m^2 g^{-1}). The variation in ECSA and charge transfer resistance across the different catalysts highlights the crucial role of Ru atom size and distribution in optimizing the electrochemical performance for hydrogen evolution reactions.

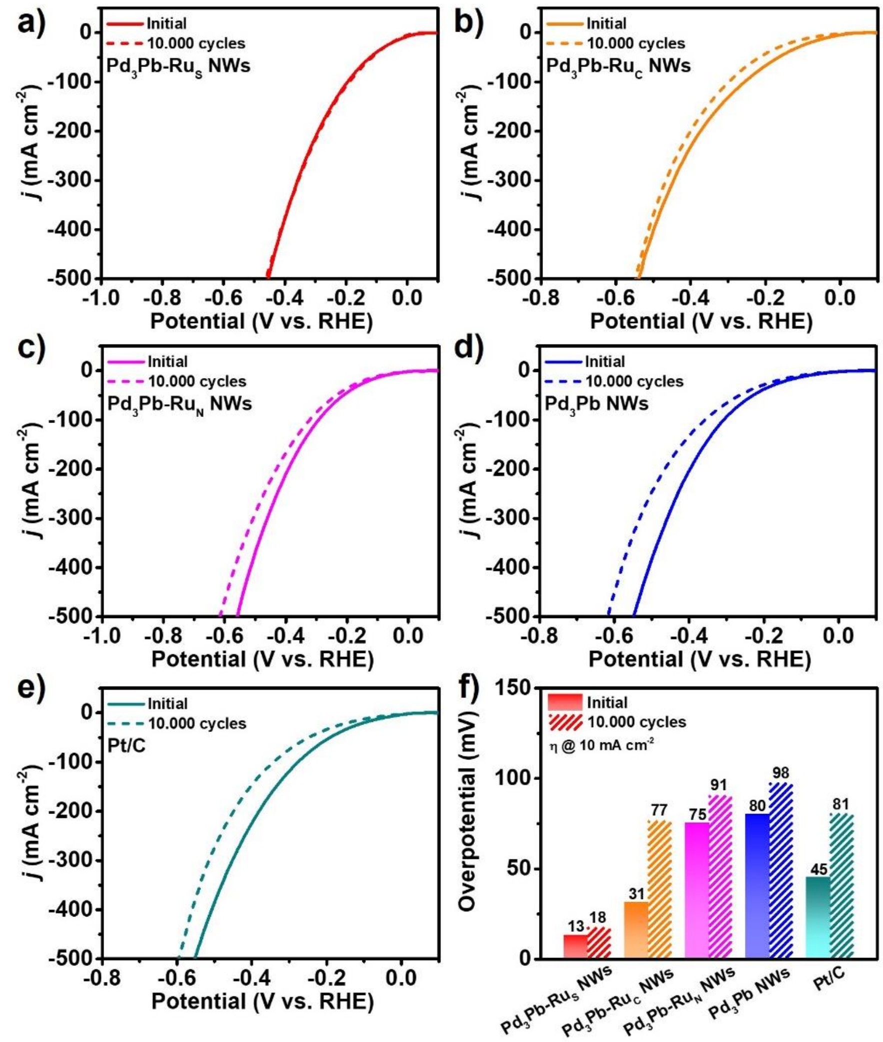

Figure 8. a-e) HER polarization curve of all catalysts in 1 M KOH at 500 mA cm^{-2} initial and after 10.000 cycles of Pd_3Pb-Ru_S NWs, Pd_3Pb-Ru_C NWs, Pd_3Pb-Ru_N NWs, Pd_3Pb NWs, and Pt/C, and f) comparation of overpotential at 10 and 100 mA cm^{-2} of all catalysts from initial and after 10.000 cycles.

Long-term stability, assessed through a 10,000-cycle test, served to identify the optimal electrocatalysts for HER in alkaline conditions. Figure 8 displayed the outstanding durability of size-dependent Ru on Pd_3Pb NWs, with the stability order as follows: Pd_3Pb-Ru_S NWs > Pd_3Pb-Ru_N NWs > Pd_3Pb NWs > Pt/C > Pd_3Pb-Ru_C NWs. Notably, Ru single atom exhibited superior stability compared to both Ru clusters and Ru nanoparticles. This enhanced stability can be attributed to the highly dispersed Ru atoms on Pd_3Pb NWs, which stabilizes the metal-support interaction.[36, 37] This interaction, in turn, can alter the electronic properties of Ru and Pd_3Pb NWs, with Ru single atom being less prone to further aggregation. Based on these findings, underscore the significant role that the size of Ru atoms plays in maintaining stability over prolonged periods. Specifically, both Ru single atoms provide robust metal-support interactions, which can modify the electronic properties and optimize the balance between activity and stability.[12, 35, 38-40] TEM images of Pd_3Pb-Ru NW catalysts post-stability test are presented in Figure 9. The images confirm that Ru single atoms maintain their structure without any aggregation. Figure 9b shows that the Pd_3Pb-Ru_S NWs have a smooth surface, indicative of a strong interaction between the Ru single atom and the Pd_3Pb support. In contrast, Pd_3Pb-Ru_C NWs and Pd_3Pb-Ru_N NWs exhibit Ru clusters and Ru nanoparticles on the surface of the Pd_3Pb NWs, which have slightly aggregated and increased in size, as shown in Figure 9f. Additionally, the atomic ratio of each element before and after 10,000 ADT cycles is presented in Table 3. Ru single atoms can maintain their atomic ratio after stability tests, while the Ru clusters exhibited a doubled increase in At% of Ru. This indicates that the presence of Ru aggregation in Ru clusters leads to an increase in the At% of Ru. For Ru nanoparticles, the At% of Ru decreased, likely due to a leaching process during the stability tests.

The high electrocatalytic activity of size-dependent Ru atoms on Pd_3Pb NWs can be attributed to the morphological, compositional, and synergistic effects of strong metallic interactions between Ru atoms and the intermetallic Pd_3Pb NWs. The NWs structure provides abundant active sites owing to the low-coordinated surface atoms, which can accelerate the adsorption and desorption of reagents and intermediates during HER. Furthermore, a larger size of Ru atoms anchored on intermetallic Pd_3Pb NWs may improve the electron transfer and water dissociation process, which is critical for HER performance. In the Pd_3Pb-Ru_S NWs catalyst, the synergistic effect occurs between the Ru atom, which has a weak binding energy with the OH_{ads}, and Pb, as an oxophilic metal with strong OH_{ads}. Therefore, the interaction between the Ru atom and Pd-Pb substrate is crucial for the optimum binding of adsorption intermediates on the surface of catalysts to enhance HER activity.

Table 3. Atomic ratio of Pd_3Pb-Ru_S NWs, Pd_3Pb-Ru_C NWs, and Pd_3Pb-Ru_N NWs before and after ADT 10.000 cycles.

Catalysts	**Before HER**			**After HER**		
	Pd	**Pb**	**Ru**	**Pd**	**Pb**	**Ru**
Pd_3Pb-Ru_S NWs	72.22	23.55	4.23	73.45	22.07	4.48
Pd_3Pb-Ru_C NWs	71.96	20.49	7.55	67.35	19.31	13.34
Pd_3Pb-Ru_N NWs	61.29	19.72	18.98	67.85	17.96	14.19

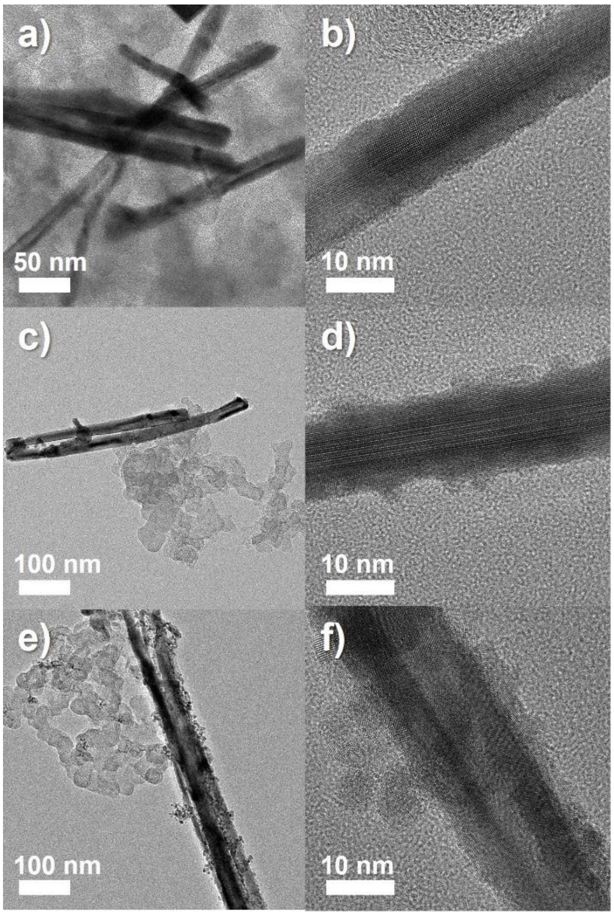

Figure 9. TEM images after stability 10.000 cycles low and high magnification a-b) Pd_3Pb-Ru_S NWs, c-d) Pd_3Pb-Ru_C NWs, and e-f) Pd_3Pb-Ru_N NWs.

3.4 Conclusion

In conclusion, the investigation into size-dependent Ru decorations on Pd_3Pb NWs elucidates a compelling relationship between the size of Ru entities and the electrocatalytic performance, particularly for HER in alkaline conditions. Notably, Ru single atom demonstrate superior activity and stability when compared to their clusters and nanoparticles counterparts. The atomic dispersion of Ru single atoms facilitates a more stable metal-support interaction with the Pd_3Pb NWs, optimizing charge distribution and electronic properties, being less prone to aggregation, and providing more active sites. This balance is vital for their potential application in industrial processes, where long-term reliability is as crucial as efficiency. This study underscores the importance of size and physical state in designing high-performance electrocatalysts for sustainable hydrogen production.

3.5 References

1. Megía, P. J.; Vizcaíno, A. J.; Calles, J. A.; Carrero, A. *Energy & Fuels* **2021,** 35, (20), 16403-16415.

2. Seh, Z. W.; Kibsgaard, J.; Dickens, C. F.; Chorkendorff, I.; Norskov, J. K.; Jaramillo, T. F. *Science* **2017,** 355, (6321), eaad4998.

3. Wang, H.; Abruña, H. D. *The Journal of Physical Chemistry C* **2021,** 125, (13), 7188-7203.

4. Ding, J.; Yang, H.; Zhang, S.; Liu, Q.; Cao, H.; Luo, J.; Liu, X. *Small* **2022,** 18, (52), e2204524.

5. Zhai, W.; Ma, Y.; Chen, D.; Ho, J. C.; Dai, Z.; Qu, Y. *InfoMat* **2022,** 4, (9), e12357.

6. Mahmood, N.; Yao, Y.; Zhang, J. W.; Pan, L.; Zhang, X.; Zou, J. J. *Adv Sci (Weinh)* **2018,** 5, (2), 1700464.

7. Shao, Q.; Lu, K.; Huang, X. *Small Methods* **2019,** 3, (5), 1800545.

8. Li, M.; Duanmu, K.; Wan, C.; Cheng, T.; Zhang, L.; Dai, S.; Chen, W.; Zhao, Z.; Li, P.; Fei, H.; Zhu, Y.; Yu, R.; Luo, J.; Zang, K.; Lin, Z.; Ding, M.; Huang, J.; Sun, H.; Guo, J.; Pan, X.; Goddard, W. A.; Sautet, P.; Huang, Y.; Duan, X. *Nature Catalysis* **2019,** 2, (6), 495-503.

9. Jiao, L.; Liu, E.; Hwang, S.; Mukerjee, S.; Jia, Q. *ACS Catalysis* **2021,** 11, (13), 8165-8173.

10. Zhu, S.; Qin, X.; Xiao, F.; Yang, S.; Xu, Y.; Tan, Z.; Li, J.; Yan, J.; Chen, Q.; Chen, M.; Shao, M. *Nature Catalysis* **2021,** 4, (8), 711-718.

11. Zou, Y.; Kazemi, S. A.; Shi, G.; Liu, J.; Yang, Y.; Bedford, N. M.; Fan, K.; Xu, Y.; Fu, H.; Dong, M.; Al-Mamun, M.; Zhong, Y. L.; Yin, H.; Wang, Y.; Liu, P.; Zhao, H. *EcoMat* **2022,** 5, (1), e12274.

12. Zhu, Y.; Fan, K.; Hsu, C. S.; Chen, G.; Chen, C.; Liu, T.; Lin, Z.; She, S.; Li, L.; Zhou, H.; Zhu, Y.; Chen, H. M.; Huang, H. *Adv Mater* **2023,** 35, (35), e2301133.

13. Li, L.; Tian, F.; Qiu, L.; Wu, F.; Yang, W.; Yu, Y. *Catalysts* **2023,** 13, (12), 1497.

14. Song, H.; Wu, M.; Tang, Z.; Tse, J. S.; Yang, B.; Lu, S. *Angew Chem Int Ed Engl* **2021,** 60, (13), 7234-7244.

15. Zhang, J.; Chen, G.; Liu, Q.; Fan, C.; Sun, D.; Tang, Y.; Sun, H.; Feng, X. *Angew Chem Int Ed Engl* **2022,** 61, (39), e202209486.

16. Sun, X.; Song, Y.; Jiang, G.; Lan, X.; Xu, C. *Science China Materials* **2023,** 67, (1), 1-17.

17. Shen, T.; Wang, S.; Zhao, T.; Hu, Y.; Wang, D. *Advanced Energy Materials* **2022,** 12, (39), 2201823.

18. Zhu, J.; Cai, L.; Tu, Y.; Zhang, L.; Zhang, W. *Journal of Materials Chemistry A* **2022,** 10, (29), 15370-15389.

19. Yan, Y.; Du, J. S.; Gilroy, K. D.; Yang, D.; Xia, Y.; Zhang, H. *Adv Mater* **2017,** 29, (14), 1605997.

20. Guo, J.; Jiao, S.; Ya, X.; Zheng, H.; Wang, R.; Yu, J.; Wang, H.; Zhang, Z.; Liu, W.; He, C.; Fu, X. *Chemistry* **2022,** 28, (69), e202202221.

21. Gamler, J. T. L.; Ashberry, H. M.; Skrabalak, S. E.; Koczkur, K. M. *Adv Mater* **2018**, e1801563.

22. Younan Xia, P. Y., Yugang Sun, Yiying Wu, Brian Mayers, Byron Gates, Yadog Yin, Franklin Kim, and Haoquan Yan. *Adv Mater* **2003,** 15, 353-389.

23. Huo, D.; Kim, M. J.; Lyu, Z.; Shi, Y.; Wiley, B. J.; Xia, Y. *Chem Rev* **2019,** 119, (15), 8972-9073.

24. Huang, H.; Ruditskiy, A.; Choi, S. I.; Zhang, L.; Liu, J.; Ye, Z.; Xia, Y. *ACS Appl Mater Interfaces* **2017,** 9, (36), 31203-31212.

25. Wahidah, H.; Hong, J. W. *Bulletin of the Korean Chemical Society* **2022,** 43, (9), 1111-1117.

26. Guo, J.; Liu, W.; Fu, X.; Jiao, S. *Nanoscale* **2023,** 15, (19), 8508-8531.

27. Chang, Q.; Hong, Y.; Lee, H. J.; Lee, J. H.; Ologunagba, D.; Liang, Z.; Kim, J.; Kim, M. J.; Hong, J. W.; Song, L.; Kattel, S.; Chen, Z.; Chen, J. G.; Choi, S. I. *Proc Natl Acad Sci U S A* **2022,** 119, (11), e2112109119.

28. Yao, H.; Wang, X.; Li, K.; Li, C.; Zhang, C.; Zhou, J.; Cao, Z.; Wang, H.; Gu, M.; Huang, M.; Jiang, H. *Applied Catalysis B: Environmental* **2022,** 312, 121378.

29. Bae, S.-Y.; Mahmood, J.; Jeon, I.-Y.; Baek, J.-B. *Nanoscale Horizons* **2020,** 5, (1), 43-56.

30. Zhang, L.; Jang, H.; Wang, Y.; Li, Z.; Zhang, W.; Kim, M. G.; Yang, D.; Liu, S.; Liu, X.; Cho, J. *Adv Sci (Weinh)* **2021,** 8, (15), e2004516.

31. Gao, T.; Tang, X.; Li, X.; Wu, S.; Yu, S.; Li, P.; Xiao, D.; Jin, Z. *ACS Catalysis* **2022,** 13, (1), 49-59.

32. Li, C.; Kim, S. H.; Lim, H. Y.; Sun, Q.; Jiang, Y.; Noh, H. J.; Kim, S. J.; Baek, J.; Kwak, S. K.; Baek, J. B. *Adv Mater* **2023,** 35, (21), e2301369.

33. Wang, D.; Jiao, D.; Gong, M.; Fan, H.; Chen, Y.; Wang, L.; Fan, J.; Wu, J.; Singh, D. J.; Zhao, J.; Zheng, W.; Cui, X. *Applied Catalysis B: Environmental* **2023,** 325, 122331.

34. Jiang, B.; Zhu, J.; Xia, Z.; Lyu, J.; Li, X.; Zheng, L.; Chen, C.; Chaemchuen, S.; Bu, T.; Verpoort, F.; Mu, S.; Wu, J.; Wang, J.; Kou, Z. *Adv Mater* **2024,** 36, (2), e2310699.

35. Liu, Y.; Wu, J.; Zhang, Y.; Jin, X.; Li, J.; Xi, X.; Deng, Y.; Jiao, S.; Lei, Z.; Li, X.; Cao, R. *ACS Appl Mater Interfaces* **2023,** 15, (11), 14240-14249.

36. Luo, Z.; Zhao, G.; Pan, H.; Sun, W. *Advanced Energy Materials* **2022,** 12, (37), 2201395.

37. Fu, Q.; Lin, L.; Wu, T.; Zhang, Q.; Wang, X.; Xu, L.; Zhong, J.; Gu, L.; Zhang, Z.; Xu, P.; Song, B. *ACS Appl Mater Interfaces* **2022,** 14, (32), 36688-36699.

38. Li, J.; Li, Y.; Wang, J.; Zhang, C.; Ma, H.; Zhu, C.; Fan, D.; Guo, Z.; Xu, M.; Wang, Y.; Ma, H. *Advanced Functional Materials* **2022,** 32, (16), 2109439.

39. Wang, X.; Zhang, J.; Wang, Z.; Lin, Z.; Shen, S.; Zhong, W. *Chinese Journal of Structural Chemistry* **2023,** 42, (4), 100035.

40. Hu, Q.; Li, G.; Huang, X.; Wang, Z.; Yang, H.; Zhang, Q.; Liu, J.; He, C. *Journal of Materials Chemistry A* **2019,** 7, (33), 19531-19538.

Chapter 4. Strain and Ligand Effects Induced by Interstitial Boron in Intermetallic Pd_3Pb Nanowires: An Efficient Electrocatalyst for Ethanol Oxidation Reaction

4.1 Introduction

Direct alcohol fuel cells (DAFCs) have garnered significant interest as a promising alternative to conventional energy conversion systems due to their impressive energy storage capacity, low operating temperature, and renewable nature.[1-4] Nonetheless, developing highly efficient and robust electrocatalysts for alcohol oxidation processes remains a crucial challenge for the practical implementation of DAFCs. Among various alcohols, ethanol has been recognized as a promising fuel for DAFCs due to its high energy density (8.03 $kWh.kg^{-1}$), low toxicity, and abundance. However, the oxidation of ethanol in alkaline media is a challenging task due to the sluggish reaction kinetics and the formation of undesired byproducts.

In recent years, intermetallic compounds have emerged as a promising class of electrocatalysts for ethanol oxidation reactions (EOR) in an alkaline medium. The formation of intermetallic compounds can occur spontaneously, requiring a negative change in Gibbs free energy (ΔG), considering both enthalpy and entropy changes. Intermetallic compounds are characterized by ordered arrangements of atoms and often exhibit distinct properties compared to their constituent metals, such as mechanical strength, magnetic properties, and catalytic activity.[5-7] In particular, Pd-based intermetallic nanocrystals (NCs) have been extensively studied as efficient electrocatalysts for various applications. Bimetallic PdM (M: other metals) with the composition of Pd_3Pb intermetallic NCs has been reported to demonstrate high electrocatalytic activity and stability toward the ethanol oxidation reaction in an alkaline medium.[3,8-10] Their unique properties contribute to reducing surface poisoning intermediates and enhancing stability. Furthermore, lead (Pb), known as an oxophilic metal, can enhance the activity of the ethanol oxidation reaction by providing adsorption sites for OH^- species on Pd sites, thereby reducing the poisoning of CO_{ads} intermediates on the catalyst surface.[11,12] In addition, the morphology of NCs is crucial as surface atoms play a dominant role in electrocatalytic reactions. Therefore, nanowires (NWs) have been chosen as a model for catalysts due to their anisotropic 1D nanostructure, exposing numerous active sites and featuring low-coordinated surface atoms such as kinks, ledges, and step atoms, making them beneficial for electrocatalytic reactions.[13-15]

On the other hand, further improvement in the electrocatalytic performance of Pd_3Pb NCs is still required to meet the practical demands of DAFCs. Numerous research efforts have focused on the incorporation of non-metallic and metalloid elements into Pd-based NCs. Several non-metals and metalloids, including hydrogen, boron, phosphorus, carbon, sulfur, and nitrogen, can modify the electronic structure and geometric properties of metal catalysts to enhance their catalytic activity and selectivity in various reactions.[16-22] Boron, as a metalloid element, has a smaller atomic radius (87 pm) compared to Palladium (137 pm), allowing it to be interstitially doped into the Pd-Pd lattice. Furthermore, regulating the interstitial boron doping content in Pd-based NCs increases the inter-lattice spacing, introduces tensile strain, and enhances the availability of surface electron sites for the adsorption of intermediate species during electrocatalysis. Tensile strain typically induces an upshift in the d-band center, facilitating the adsorption of intermediate species. This phenomenon may strengthen the binding of CO_{ads}, leading to potential poisoning of the catalyst surface. Conversely, a downshift in the d-band center can weaken the binding energy of intermediate species, alleviating the CO poisoning effect. This downshift also accelerates the formation of C1 pathway selectivity.[23] However, it may compromise the facilitation of carbonaceous intermediates, resulting in a decrease in overall catalytic activity. This paradox poses a significant challenge in the design and construction of highly efficient EOR catalysts.

In the C1 pathway, the cleavage of the C–C bond in the CH_3CO^* intermediate species is pivotal for generating CO^* and CHx^*, ultimately resulting in the complete formation of CO_2. The overall reaction involves the consumption of 12 electrons. Considering the C1 selectivity mechanism, orbital hybridization emerges as a potential method for shifting the d-band center position. The incorporation of a p-block element like boron into a d-block metal matrix from Pd can introduce p-d hybridization effects.[23-25] This hybridization might result in the formation of new bonding and antibonding states, which can alter the overall electronic structure and potentially lead to a downshift in the d-band center, as it introduces new electronic states that can modify the position of the d-band relative to the Fermi level. Additionally, the insertion of boron into Pd-based catalysts can accentuate C–C bond cleavage while also inhibiting the formation of CO_{ads} intermediates, thereby accelerating EOR activity. By controlling the tensile strain (strain effect) and ligand effect on the catalyst surface, the intrinsic activity of each active site can be optimized.[26-27]

In this study, we present the synthesis and characterization of interstitial boron in intermetallic Pd_3Pb nanowires (NWs) and investigate their selectivity for C1 products during EOR in an alkaline medium. Pd_3Pd-B NWs demonstrate a higher in activity and C1 product selectivity with FE of C1 product over than 50%. Pd_3Pb-B NWs exhibit the highest mass activity (9037 mA mg^{-1}_{Pd}) compared to Pd_3Pb-B nanocubes (5658 mA mg^{-1}_{Pd}), Pd3Pb NWs (2918 mA mg^{-1}_{Pd}) and Pd/C (1019 mA mg^{-1}_{Pd}). This indicates that the optimized d-band center, attributed to strain and ligand effects, enhances EOR activity. Based on these findings, this study opens a new avenue for developing highly efficient and stable electrocatalysts for EOR in an alkaline medium, with potential practical applications in DAFCs and other energy conversion systems.

4.2 Experimental Section

4.2.1 Chemical and materials

Palladium(II) acetylacetonate ($Pd(acac)_2$, 99%), ammonium bromide (NH_4Br, 99.0%), cetyltrimethylammonium chloride solution (CTAC, 25 wt% in H_2O), hydrazine hydrate (50 - 60%), isopropanol (9.9%) and Nafion perfluorinated resin solution (5 wt%) were obtained from Sigma-Aldrich. Oleylamine (OAm, 50%) was obtained from TCI chemical. Lead(II) 2,4-pentanedionate ($Pb(acac)_2$, 99%), (1-Hexadecyl)trimethylammonium bromide (CTAB, 98%) and commercial Pd/C (30 wt%) were obtained from Alfa aesar. Chloroform ($CHCl_3$) was obtained from Daejung chemical. Potassium hydroxide (KOH, 95.0%) was obtained from Samchun. Other chemicals were reagent grade, and deionized water with a resistivity of greater than 18.3 MΩ·cm was used in the preparation of reaction solutions. Hexane was of technical grade.

4.2.2 Synthesis of Pd_3Pb NWs and Pd_3Pb nanocubes

15 mL of OAm was preheated from RT to 100°C for 30 min (as solution A). In another vial, 0.3 mmol of $Pd(acac)_2$, 0.1 mmol of $Pb(acac)_2$, 125 mg of NH_4Br, and 5 mL of OAm were mixed in a 30 mL vial. The mixture was sonicated until it dissolved, then the glass vial was transferred into the water bath and heated at 80°C for 30 min (as solution B). After 30 min, solution B was rapidly injected into solution A. Temperature was increased from 100°C to 150°C for 30 min and kept reaction at 150°C for 6 h. The solution was washed with a mixture of hexane and ethanol (1:1) several times.

For the synthesis of Pd_3Pb nanocubes, 7.6 mg of $Pd(acac)_2$, 8 mg of $Pb(acac)_2$, 10 mg of NH_4Br, 3 mL of OAm, and 3 mL of ODE were mixed in a 20-mL vial. The mixture was sonicated for 15 min and then heated at 200°C for 12 h.

4.2.3 Boron insertion into Pd_3Pb NWs and Pd_3Pb nanocubes

~30 mg of Pd_3Pb NWs or Pd_3Pb nanocubes, and 8 mL of Borane tetrahydrofuran complex (BH_3.THF) were mixed in a 25 mL Teflon-lined Autoclave stainless steel. The mixture was sonicated until dispersed. Then, heated the mixture at 180°C for 7 days. The product was washed with ethanol several times.

4.2.4 Preparation of catalysts

Catalysts powder was prepared by mixing pure metal of catalysts with carbon support (Vulcan XC 72R) with a ratio of 1:1. Catalyst ink was prepared by dispersing certain amounts of catalysts in a mixture of 2-propanol, deionized water (DIW), and Nafion (5 wt%) with a ratio of 4:1:0.025 to make a catalyst ink of 0.34 μg_{Pd} μL^{-1}.

4.2.5 Electrochemical measurements

Electrochemical measurements were carried out in a three-electrode cell using Bio-Logic EC-Lab SP-300. Graphite carbon and Hg/HgO (1 M NaOH) served as the counter and reference electrodes, respectively. The Pd_3Pb NWs and Pd_3Pb-B NWs were loaded onto a carbon support (Vulcan XC 72R) before assessing their electrocatalytic properties. Catalyst ink was prepared by dispersing specific amounts of catalysts in a mixture of 2-propanol, deionized water (DIW), and Nafion (5 wt.%) with a ratio of 4:1:0.025 to create a catalyst ink of 0.4 μg_{Pd} μL^{-1}. All electrochemical data were obtained at room temperature. The working electrode was a 5-mm diameter glassy carbon electrode (GCE) with 2.5 μL of drop-casted catalyst ink (1 μg of total Pd). The precise amount of Pd loaded on the GCE was determined by inductively coupled plasma-optical emission spectroscopy (ICP-OES). The electrolyte solutions were purged with N_2 gas for 30 min before conducting electrochemical experiments. The dried GCE was electrochemically cleaned by 30 potential cycles between –0.944 and 0.356 V vs Hg/HgO at a scan rate of 50 mV s^{-1} in 1.0-M KOH. The cyclic voltammograms (CVs) of all catalysts were obtained between –0.844 and 0.356 V vs Hg/HgO at a scan rate of 50 mV s^{-1}. For CO-stripping experiments, the surface of the catalysts loaded on the GCE was saturated with CO by purging with CO gas in 1.0-M KOH while holding the working electrode at –0.3 V vs Hg/HgO for 15 min, and then CO dissolved in the electrolyte was removed by purging with N_2 gas for 30 min. EIS measurements were conducted at −1.2 V vs. Hg/HgO over a frequency range from 1 to 10 MHz.

4.2.6 Product analysis

The quantification of potential products from the EOR can be accurately performed using high-performance liquid chromatography (HPLC) coupled with the Faraday's law of electrolysis. Initially, a prolonged current-time (*i*-*t*) test is conducted to accumulate the reaction products for analysis. The concentration of the resulting acetate (CH3COO⁻) is determined based on a pre-established standard curve. For the *i*-*t* test, the catalysts are applied onto a glassy carbon plate electrode (6.25 cm^2) to achieve a metal loading of 32 μg_{Pd} cm^{-2}. The electrolysis is carried out in N_2-saturated 1.0 M KOH solution containing 1.0 M ethanol, using a total volume of 1.5 mL electrolyte in batch cell. The process is conducted under chronoamperometry with different catalysts to collect the total charge (Q) passed through the system. Subsequently, a set of standard solutions for acetic acid (CH_3COOH) is prepared with varying concentrations to construct a standard curve. This curve is derived from the correlation between the integrated HPLC peak areas, detected by Agilent 1260 Infinity II Diode Array Detector HS, and the known concentrations of the standards (Figure S5). Lastly, the Faradaic efficiency for the generated acetic acid is calculated using Faraday's law, based on the total charge and the concentration of acetic acid determined from the HPLC analysis.

$$FE\ C2\ (\%) = \left(\frac{e\ x\ n\ x\ F}{Q}\right) x\ 100$$

Where *e* is the number of electrons transferred to CH_3COOH (*e* = 4), *n* is the total moles of CH_3CHO or CH_3COOH, *F* is the Faraday constant (96485 C mol^{-1}), and *Q* is the total charge.

The FE of the C1 pathway:

$$FE\ C1\ (\%) = 100\ - FE\ C2$$

4.2.7 Characterization

Transmission electron microscopy (TEM) and scanning electron microscopy (SEM) images of the prepared catalysts were obtained by using a JEOL JEM-2100F and a JEOL JEM-7210F, respectively. SEM analysis was done by using (used instrument) at total-period analysis center for Ulsan chemical industry of Korea Basic Science Institute (KBSI). ICP-OES measurement was conducted using a Spectrouble-ICP-OES (Ametek). X-ray diffraction (XRD) measurement was conducted on a Rigaku D/MAX2500V/PC. X-ray photoelectron spectroscopy (XPS) measurements were conducted using a Thermo VG Scientific Sigma Probe spectrometer with Al Kα X-ray (1486.6 eV) as a light source. XPS data were calibrated using the C 1 s peak at 284.5 eV.

4.3 Result and Discussion

4.3.1 Characterization of Pd_3Pb-B NWs

The synthesis method for inserting boron into intermetallic Pd_3Pb NWs is described in Figure 1a. The intermetallic Pd_3Pb NWs were prepared through a two-step wet chemical method using $Pd(acac)_2$ and $Pb(acac)_2$ as metal precursors, OAm as the solvent, and NH_4Br as a shape-directing agent. The as-prepared Pd_3Pb NWs were characterized by scanning electron microscopy (SEM) images, displaying the uniformity of the nanowire product (Figure 2a). To prepare boron-doped Pd_3Pb NWs (Pd_3Pb-B NWs), a boron tetrahydrofuran complex (BH_3.THF) as a boron source was added to the Pd_3Pb NWs using a solvothermal method at 180°C for seven days. The Pd_3Pb-B nanocubes were prepared for comparison in morphology effect (Figure 2b). Inductively coupled plasma optical emission spectroscopy (ICP-OES) revealed the composition of Pd, Pb, and B atoms in Pd_3Pb-B NWs and nanocubes possessed similar atomic ratio (Table 1). The intermetallic structure of Pd_3Pb NCs was characterized by high-angle annular dark-field scanning transmission electron microscopy (HAADF-STEM) images in Figure 1b-d. The atomic-resolution HAADF-STEM image of Pd_3Pb-B NWs shows interplanar distances of 2.35 Å and 2.90 Å, corresponding to the (111) and (110) planes of the Pd-Pb alloy (Figure 1c). This indicates lattice expansion compared to Pd_3Pb NCs (2.34 Å and 2.84 Å) for the (111) and (110) planes, respectively, signifying the successful insertion of boron into the Pd_3Pb NWs.[28] Additionally, the presence of boron was observed using HAADF-STEM combined with energy-dispersive X-ray spectroscopy (EDS) mapping images, clearly depicting the distribution of boron elements in Pd_3Pb NWs (Figure 1e).

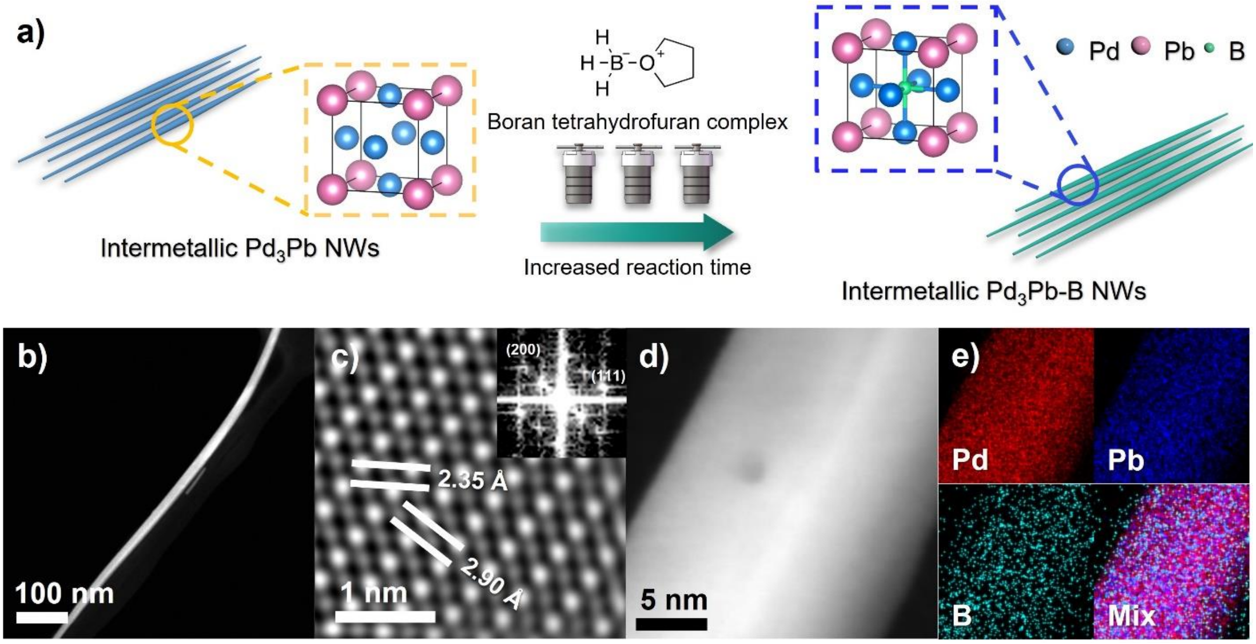

Figure 1. a) Schematic illustration to the formation of Pd_3Pb-B NWs, HAADF STEM image of Pd_3Pb-B NWs b) low magnification, c) atomic resolution of Pd_3Pb-B NWs and inserted FFT image, d) high magnification HAADF-STEM image of Pd_3Pb-B NWs, and e) EDS mapping.

The intermetallic Pd_3Pb NWs exhibit an ordered atomic arrangement that can be enlarged in lattice parameter after the insertion of boron but does not alter the intermetallic structure. The crystal structure, analyzed through X-ray diffraction (XRD) peaks of both Pd_3Pb NWs and Pd_3Pb-B NWs, reveals an fcc structure with the presence of the intermetallic Pd_3Pb phase ($Pm\bar{3}m$, a = 4.035 Å), as illustrated in Figure 3a.[29,30] Tensile strain in Pd_3Pb-B NWs and Pd_3Pb nanocubes were confirmed by a negative shift in the XRD peak compared to the standard Pd_3Pb NCs (JCPDS #50-1631), and the lattice parameter based on the (111) position is summarized in Table 2. The lattice parameter of Pd_3Pb NWs is calculated to be 4.030 Å with approximately 0.10% compressive strain (relative to the standard Pd_3Pb 4.035 Å, #50-1631). Additionally, after the insertion of boron into intermetallic Pd_3Pb NWs, the main peak shifts to a lower degree, resulting in the enlargement of the lattice parameter to 4.098 (Figure 3b). Furthermore, the XRD peaks are well-matched with the Rietveld refinement calculation, confirming the presence of boron in the octahedral site of the Pd-Pb lattice (Figure 3c-d). Similar result was observed in Pd_3Pb-B nanocubes, after boron insertion, XRD peak shifted to lower degree, indicating the successful insertion of boron into nanocubes.

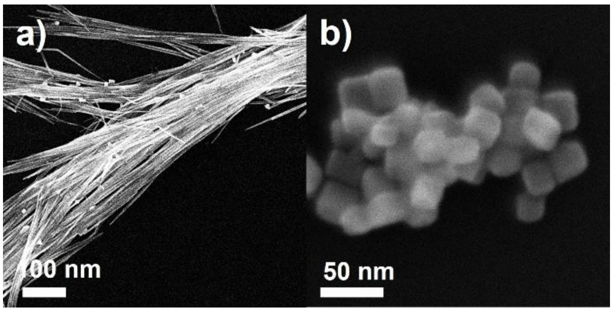

Figure 2. SEM image of a) Pd_3Pb NWs and b) Pd_3Pb nanocubes.

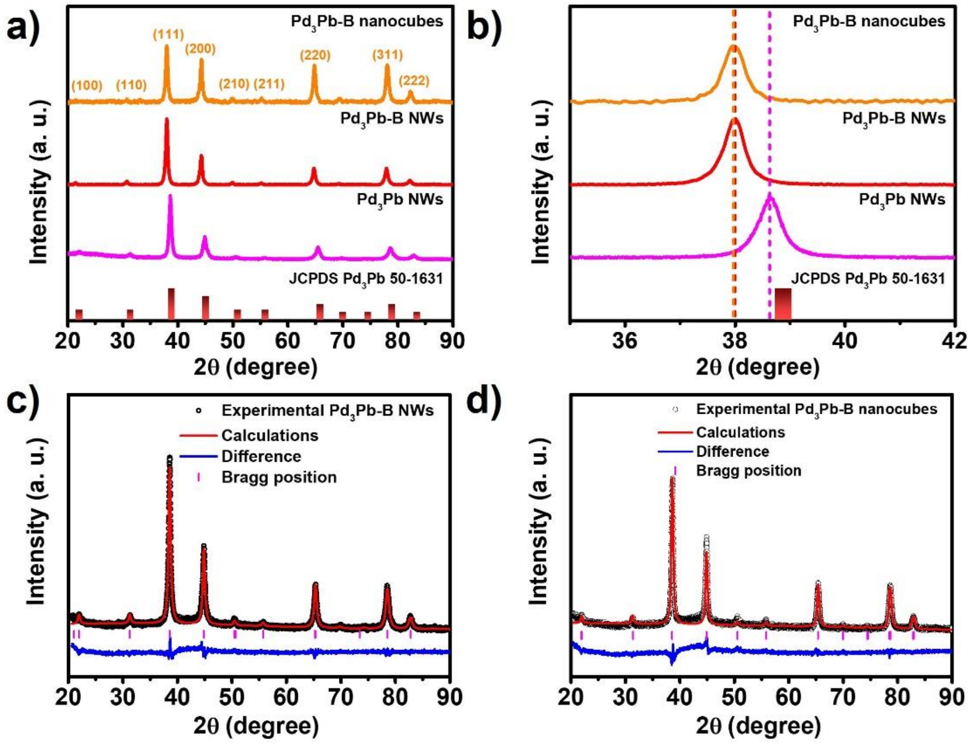

Figure 3. a-b) XRD pattern of Pd_3Pb-B NWs, Pd_3Pb-B nanocubes, Pd_3Pb NWs and high magnification, and c-d) Rietveld refinement on Pd_3Pb-B NWs and Pd_3Pb-B nanocubes.

Table 1. At% of Boron in Pd_3Pb-B NWs, Pd_3Pb nanocubes, and Pd_3Pb NWs determined by ICP–OES.

Catalysts	**At%**			**Ratio**		
	Pd	**Pb**	**B**	**Pd**	**Pb**	**B**
Pd_3Pb-B NWs	60.43	19.86	19.71	3	1	1
Pd_3Pb-B nanocubes	60.41	20.01	19.58	3	1	1
Pd_3Pb NWs	74.20	25.80	/	3	1	/

X-ray photoelectron spectroscopy (XPS) was utilized to examine the surface electronic states of Pd, Pb, and B atoms in Pd_3Pb-B NWs, comparing them with Pd_3Pb-B nanocubes, Pd_3Pb NWs and Pd NWs (Figure 4a-c). The Pd 3d XPS peaks, indicative of Pd^0 in Pd_3Pb-B NWs and Pd_3Pb-B nanocubes, exhibited a shift to higher binding energies relative to Pd_3Pb NWs and Pd NWs. A similar trend was observed in the Pb 4f spectrum, where Pb^0 in Pd_3Pb-B NWs and Pd_3Pb-B nanocubes showed a positive shift compared to Pd_3Pb NWs. Indicating that incorporation of boron into Pd-Pb lattice can alter the electronic properties both in Pd_3Pb nanowires and nanocubes.[10,31] In the B 1s spectrum of Pd_3Pb-B, peaks at 188.56 and 191.92 eV correspond to B^0 and B-^{i}, respectively. The detection of the metallic B^0 state aligns with metal-boron interactions (Pd-B or Pb-B) reported in other studies, while the B^{-i} peak is attributed to a B^{3+} state.[18] These results indicate that the interstitial incorporation of boron into Pd_3Pb NWs and Pd_3Pb nanocubes alters the surface electronic state of the intermetallic Pd_3Pb NCs, which can be beneficial for optimizing the removal or further oxidation of poisoning ethoxy intermediates and eventually improving the electrocatalytic EOR activity and stability.

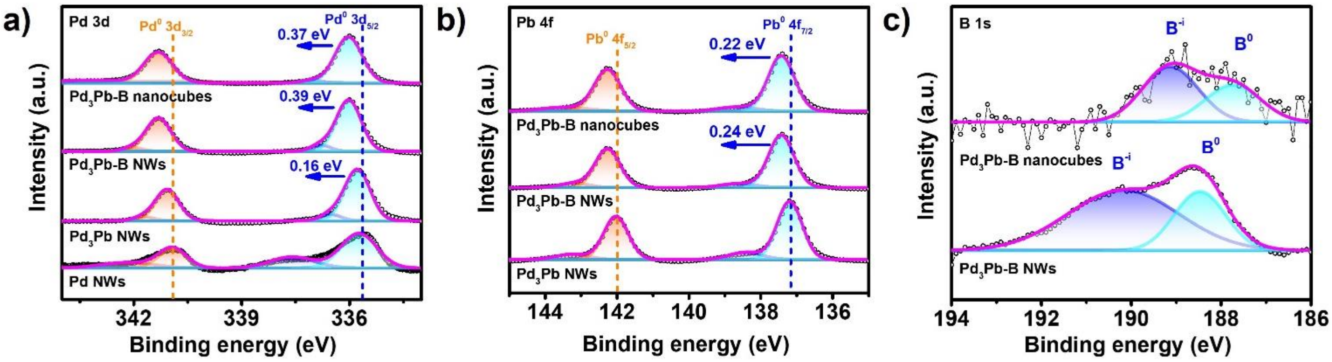

Figure 4. XPS of Pd 3d, Pb 4f, and B 1s of Pd_3Pb-B NWs compared to Pd_3Pb-B nanocubes, Pd_3Pb NWs, and Pd NWs.

4.3.2 Application of Pd_3Pb-B NWs for EOR

The electrocatalytic performance of intermetallic Pd_3Pb NWs, Pd_3Pb-B NWs, and Pd_3Pb-B nanocubes was evaluated in an anodic EOR to explore the influence of boron insertion, strain effect, and morphological effect on catalytic activity. Commercial Pd/C was prepared as a reference catalyst for comparison. Before evaluating the electrochemical performance, as-prepared Pd_3Pb NWs, Pd_3Pb-B NWs, Pd_3Pb-B nanocubes, and Pd_3Pb nanocubes were loaded on carbon black (Vulcan XC-72R) to form Pd_3Pb NWs/C, Pd_3Pb-B NWs/C, Pd_3Pb-B nanocubes/C and the actual Pd content was measured by ICP-OES (Table 1). The mass activity of all catalysts was evaluated under cyclic voltammetry in N_2-saturated 1.0 M KOH, and 1.0 M ethanol are displayed in Figure 5a. The Pd_3Pb-B NWs exhibited a mass activity of 9037 mA mg^{-1}_{Pd}, which is 1.6 times higher than Pd_3Pb-B nanocubes (5658 mA mg^{-1}_{Pd}), 3.0 times higher than Pd_3Pb NWs (2918 mA mg^{-1}_{Pd}), 3.6 times higher than Pd_3Pb nanocubes (2227 mA mg^{-1}_{Pd}), and 5.6 times higher than commercial Pd/C (1019 mA mg^{-1}_{Pd}).

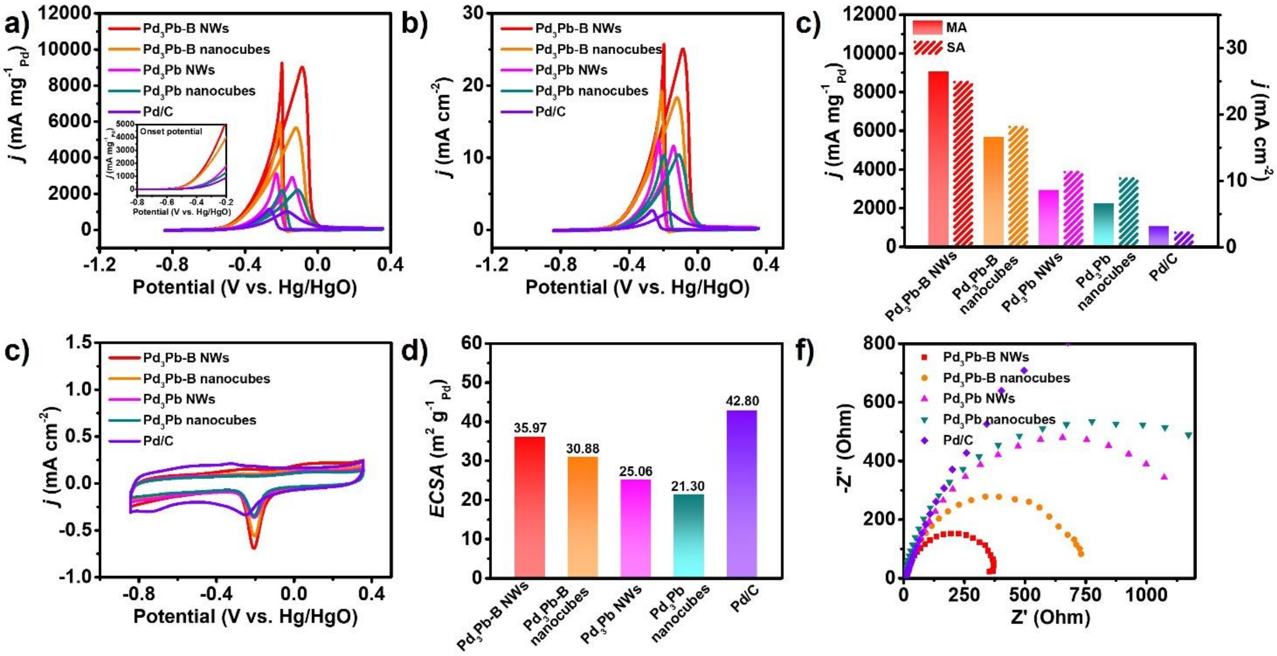

Figure 5. CVs of various catalysts on GCE a) in 1 M KOH and 1 M EtOH solution, inset figure in 4a) onset potential, b) specific activity of all catalysts, and c) mass and specific activity of all catalysts, d) CVs of various catalysts on GCE in 1.0 M KOH, e) ECSA of all catalysts, and f) Nyquist plots for various catalysts in 1.0 M KOH at -0.12 V.

The onset potential of Pd_3Pb-B NWs appeared at −0.400 V, whereas that of Pd_3Pb-B nanocubes, Pd_3Pb NWs, Pd_3Pb nanocubes, and Pd/C catalysts appeared at −0.388, −0.267, −0.236, and −0.183 V, respectively (inset Figure 5a). The Pd_3Pb-B NWs possessed a negative potential compared to their counterparts, indicating faster kinetics in beginning catalyzing the ethanol oxidation. The analogous trend was also observed in the specific activity (Figure 5b-c). In addition, the electrochemical impedance spectroscopy (EIS) spectra of the catalysts were obtained in N_2-saturated 1.0 M KOH (Fig. 5f). The charge transfer resistance of Pd_3Pb-B NWs was significantly lower than that of Pd_3Pb nanocubes, Pd_3Pb NWs and Pd/C catalysts, indicating that after insertion of boron into intermetallic Pd_3Pb NWs can enhance faster charge transfer rate and the presence of low-coordinated surface atom in nanowires can accelerate the mass transport, resulting in the enhancement of EOR activity.[3] To assess the active sites of the catalysts, the electrochemically active surface areas (ECSAs) were determined by integrating the Coulombic charge associated with the reduction of oxygen species in the cyclic voltammograms (CVs) of the catalysts (Fig. 5c-d). The ECSA values for Pd_3Pb-B NWs, Pd_3Pb-B nanocubes, Pd_3Pb NWs, Pd_3Pb nanocubes, and Pd/C were estimated to be 35.97, 30.88, 25.06, 21.30, and 42.80 $m^2\ g^{-1}$, respectively.

The electrochemical stabilities of all catalysts were assessed through chronoamperometry (CA) measurements. The CA test was performed for 5400 seconds at −0.120 V versus Hg/HgO in a N_2-saturated 1.0 M KOH and 1.0 M ethanol solution. As shown in Fig. 6a, Pd_3Pb-B NWs demonstrated a significantly higher current density during long-term operations compared to other catalysts, indicating enhanced stability under prolonged electrochemical conditions. Furthermore, in Figure 6b-e, the accelerated durability test (ADT) after 10,000 cycles was evaluated for all catalysts. The ADT revealed that Pd_3Pb-B NWs exhibited only a loss in mass activity of 13.09%, while Pd_3Pb-B nanocubes, Pd_3Pb NWs, Pd_3Pb nanocubes, and Pd/C showed losses of about 14.68, 36.88, 41.35 and 56.64%, respectively. These findings indicate the superior catalytic stability of Pd_3Pb-B, suggesting that boron insertion and the induced tensile strain contribute to the catalyst's robustness, preventing degradation over extended operation times. Moreover, to evaluate the CO adsorption capability on the catalyst's surface, CO-stripping measurement was applied. The main peak and onset potential of CO were shifted to a more negative potential (–0.102 V) in Pd_3Pb-B NWs, while the Pd_3Pb-B nanocubes, Pd_3Pb NWs, Pd_3Pb nanocubes and Pd/C exhibited –0.095, –0.093, –0.087 and –0.076 V, respectively (Figure 7a). This indicates that an introduction of boron and nanowires morphology have better desorption capability for CO_{ads} compared to Pd_3Pb nanocubes, Pd_3Pb NWs and Pd/C, highlighting the superior performance of Pd_3Pb-B NWs.

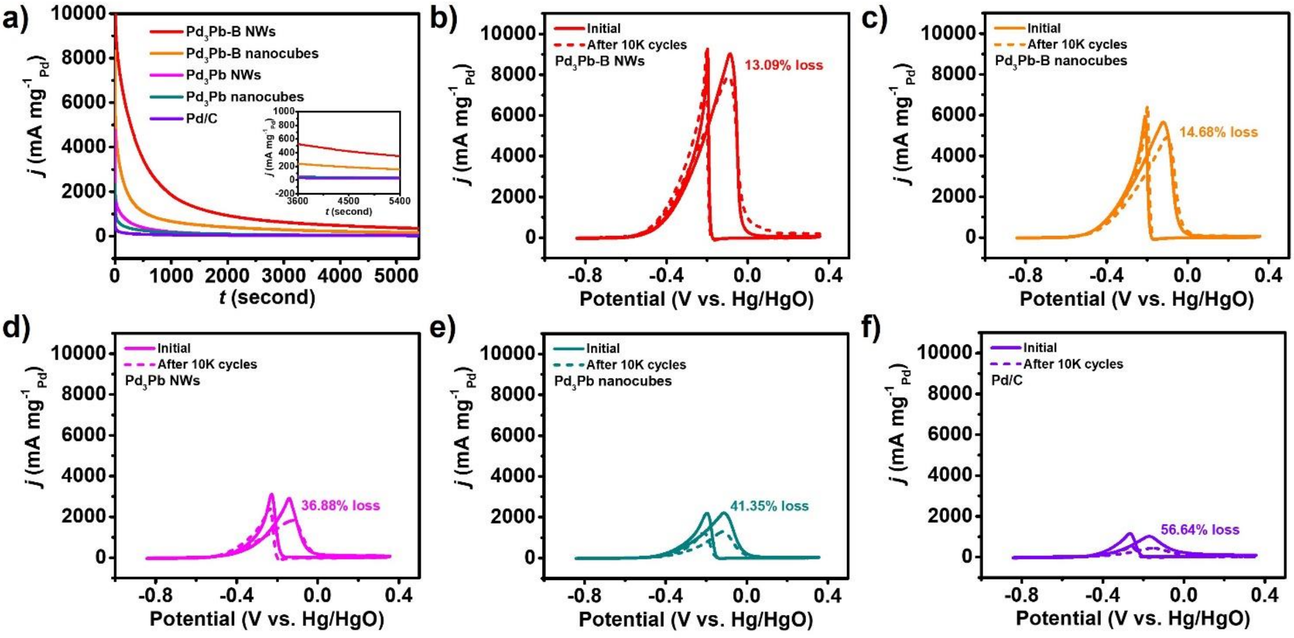

Figure 6. a) Chronoamperometric curve of all catalysts in 1.0 M KOH and 1.0 M ethanol at −0.12 V and the inset figure in part (a) is CA from 2500 to 5400 s, Cyclic voltammograms for ethanol electro-oxidation to evaluate the durability initial and after 10.000 cycles of b) Pd_3Pb-B NWs, c) Pd_3Pb-B nanocubes, d) Pd_3Pb NWs, and e) Pd/C catalysts.

4.3.3 Mechanism of C1 pathway selectivity in Pd_3Pb-B NWs

In the context of EOR, the mechanisms underlying product formation can be broadly categorized into C1 and C2 pathways, as illustrated in Figure 8. The C1 pathway is distinguished by the direct conversion of ethanol to CO_2, a process requiring the involvement of 12 electrons and characterized by the cleavage of the C–C bond, followed by the oxidation of CO^* (the rate-determining step in the C1 pathway).[32-34] On the other hand, the C2 pathway operates through a more conservative electron requirement, involving only 4 electrons, with acetaldehyde serving as the key intermediate in the reaction process. This dichotomy in the reaction pathways underscores the complexity of EOR and highlights the intricate interplay of molecular transformations that govern the efficiency and selectivity of the reaction.

Furthermore, the incorporation of boron into Pd_3Pb NCs has been observed to modify the hybridization between adjacent Pd and B atoms, thereby influencing the selectivity towards C1 products.[23]

Interestingly, while tensile strain typically leads to an upshift in the d-band center, the presence of boron induces p-d orbital hybridization, which contributes to a downshift in the d-band center, as depicted in Figure 7b. The d-band center position of Pd_3Pb-B NWs (−4.56 eV) was lower than those of Pd_3Pb-B nanocubes (−4.26 eV), Pd_3Pb NWs (−4.35 eV), Pd_3Pb nanocubes (−4.17 eV) and Pd/C catalysts (−3.97 eV), indicating that the binding strength of $(CO)_{ads}$ with the surface of Pd_3Pb-B NWs is weaker than its counterparts. This downshift is associated with weakened CO adsorption and a reduced poisoning effect, enhancing the catalyst's performance. The Faradaic efficiency (FE) for C1 and C2 products was quantified through high-performance liquid chromatography (HPLC) analysis. The Pd/C catalyst demonstrated a higher FE for C2 products, approximately 96.51%, and exhibited a mere 3.49% for C1 products, indicating a selective preference towards the formation of acetaldehyde and acetic acid. Conversely, after the introduction of boron, there was a notable decrease in the FE for C2 products alongside an increase in C1 selectivity. Specifically, the Pd_3Pb-B NWs showed a significant presence of C1 products at 78.96% and C2 products at 21.04%. As well as Pd_3Pb-B nanocubes displayed 70.27% for C1 products, while C2 products were recorded at 29.73. The Pd_3Pb NWs and Pd_3Pb nanocubes without boron insertion exhibited a higher FE for C1 products 54.07 and 48.83% than for C2 products of 45.93, and 51.17%, respectively (Figure 7c).

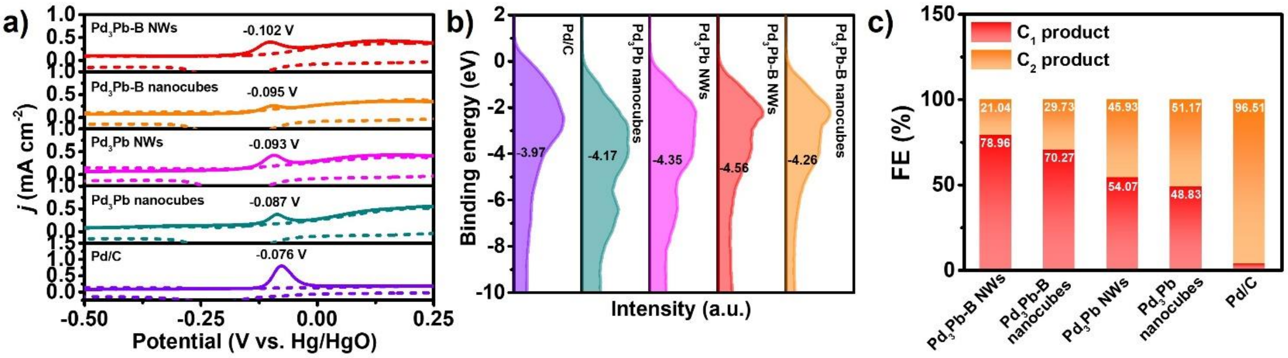

Figure 7. a) CO-stripping voltammogram of Pd_3Pb-B NWs, Pd_3Pb NWs, and Pd/C in 1.0 M KOH at a scan rate of 20 mV s^{-1}, b) the valence band spectra of all catalysts, and c) Faradaic efficiency of C_1 and C_2 product from all catalysts.

Moreover, the ratio of C1 to C2 products was assessed to determine the catalysts' selectivity towards these products. The ratio of C1/C2 products in Pd_3Pb-B NWs was found to be 3.75, indicating a higher selectivity towards C1 products compared to the other catalysts. These results demonstrate that incorporating boron into Pd_3Pb modifies the p-d orbital hybridization via a ligand effect, significantly increasing selectivity for C1 product formation.[35-38] Such alterations in electronic structure boost catalytic activity, underscoring the efficacy of engineered nanocrystal catalysts in optimizing ethanol oxidation reactions. This investigation emphasizes the critical role of catalyst composition and structure in realizing preferred reaction outcomes, illustrating the potential of boron insertion into Pd_3Pb NCs to enhance both efficiency and selectivity in ethanol oxidation processes.

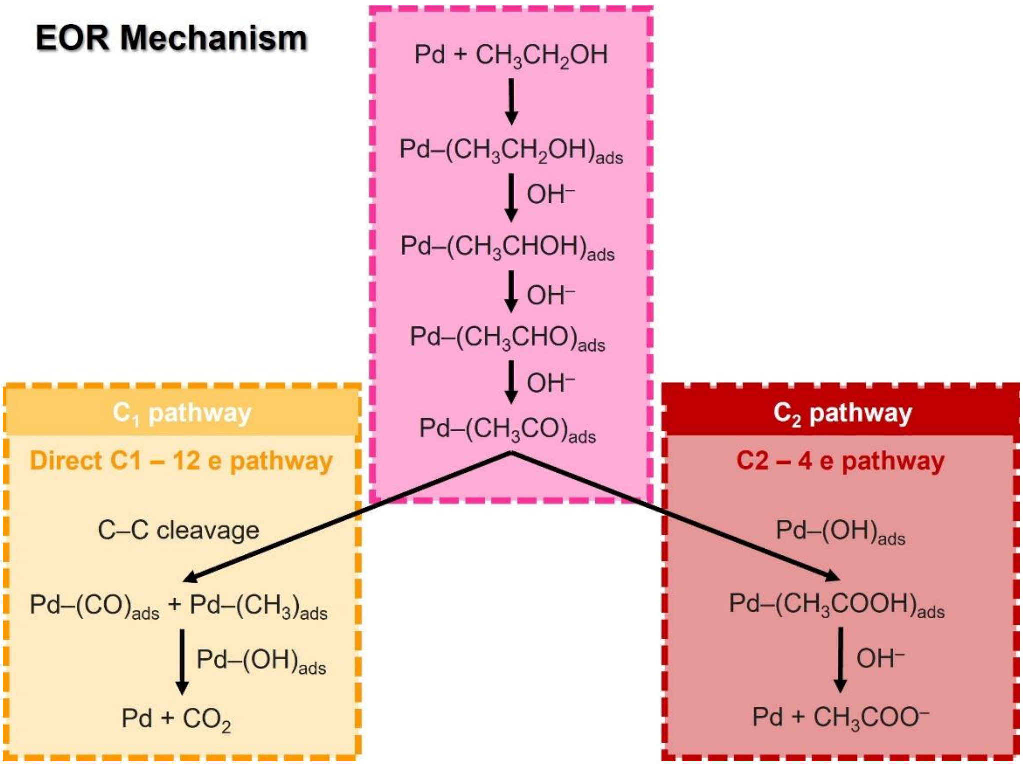

Figure 8. EOR mechanism of C_1 and C_2 pathway in alkaline medium.

4.4 Conclusion

This study focuses on the development of boron doped Pd_3Pb NWs for their use in the EOR. By incorporating boron into Pd_3Pb NWs via a solvothermal method, possessed lattice expansion and modifications to the electronic states of Pd and Pb, indicating successful boron doping. The introduction of boron significantly improved the EOR performance of Pd_3Pb-B NWs, leading to a mass activity surpassing that of Pd_3Pb-B nanocubes, undoped Pd_3Pb NWs, Pd_3Pb nanocubes, and commercial Pd/C catalysts. This improvement was attributed to the boron-induced alterations in electronic states and enhanced charge transfer rates and the presence of low-coordinated surface atoms in nanowires structure compared to nanocubes, which enhanced the catalytic activity toward EOR. Additionally, the strain effect contributed to better catalytic stability and CO desorption capabilities, emphasizing the role of structural and electronic tuning in catalyst performance. The study also highlighted a preference for the C1 pathway in ethanol oxidation of Pd_3Pb-B NWs and Pd_3Pb nanocubes, suggesting a direct conversion to CO_2 facilitated by boron doping. This selectivity is tied to electronic structure modifications, particularly the influence of boron on p-d orbital hybridization and the resultant downshift in the d-band center, which weakens CO adsorption and reduces poisoning effects. Overall, this research demonstrates the importance of compositional and structural adjustments in creating more efficient and stable catalysts for EOR. The insights gained from the boron doping effects on Pd_3Pb nanowires offer a promising approach to enhancing catalyst performance for energy conversion applications, contributing to the development of advanced materials for sustainable energy technologies.

4.5 References

1. Claudio Buanchini, P. K. S. *Chemical Reviews* **2009,** 109, (9), 4183-4206.

2. Fu, X.; Wan, C.; Huang, Y.; Duan, X. *Advanced Functional Materials* **2022,** 32, (11), 2106401.

3. Lestarini, D. T.; Hong, J. W. *Applied Surface Science* **2023,** 610, 155311-155319.

4. Singha, T.; Tomar, S.; Chakraborty, S.; Das, S.; Satpati, B. *Small* **2024**, e2309736.

5. Furukawa, S.; Komatsu, T. *ACS Catalysis* **2016,** 7, (1), 735-765.

6. Li, J.; Sun, S. *Acc Chem Res* **2019,** 52, (7), 2015-2025.

7. Xiao, W.; Lei, W.; Gong, M.; Xin, H. L.; Wang, D. *ACS Catalysis* **2018,** 8, (4), 3237-3256.

8. Bu, L.; Shao, Q.; Pi, Y.; Yao, J.; Luo, M.; Lang, J.; Hwang, S.; Xin, H.; Huang, B.; Guo, J.; Su, D.; Guo, S.; Huang, X. *Chem* **2018,** 4, (2), 359-371.

9. Bu, L.; Tang, C.; Shao, Q.; Zhu, X.; Huang, X. *ACS Catalysis* **2018,** 8, (5), 4569-4575.

10. Yao, Y.; Gu, X. K.; He, D.; Li, Z.; Liu, W.; Xu, Q.; Yao, T.; Lin, Y.; Wang, H. J.; Zhao, C.; Wang, X.; Yin, P.; Li, H.; Hong, X.; Wei, S.; Li, W. X.; Li, Y.; Wu, Y. *J Am Chem Soc* **2019,** 141, (51), 19964-19968.

11. Wu, X.; Jiang, Y.; Yan, Y.; Li, X.; Luo, S.; Huang, J.; Li, J.; Shen, R.; Yang, D.; Zhang, H. *Adv Sci (Weinh)* **2019,** 6, (24), 1902249.

12. Gunji, T.; Noh, S. H.; Tanabe, T.; Han, B.; Nien, C. Y.; Ohsaka, T.; Matsumoto, F. *Chemistry of Materials* **2017,** 29, (7), 2906-2913.

13. Li, S.; Jin, H.; Wang, Y. *Nanoscale* **2023,** 15, (6), 2488-2515.

14. Wang, Y.; Lv, H.; Sun, L.; Guo, X.; Xu, D.; Liu, B. *ACS Appl Mater Interfaces* **2021,** 13, (15), 17599-17607.

15. Xu, D.; Liu, X.; Han, M.; Bao, J. *Chem Commun (Camb)* **2016,** 52, (88), 12996-12999.

16. Jiang, K.; Xu, K.; Zou, S.; Cai, W. B. *J Am Chem Soc* **2014,** 136, (13), 4861-4.

17. Li, J.; Chen, J.; Wang, Q.; Cai, W.-B.; Chen, S. *Chemistry of Materials* **2017,** 29, (23), 10060-10067.

18. Chen, T.; Ellis, I.; Hooper, T. J. N.; Liberti, E.; Ye, L.; Lo, B. T. W.; O'Leary, C.; Sheader, A. A.; Martinez, G. T.; Jones, L.; Ho, P. L.; Zhao, P.; Cookson, J.; Bishop, P. T.; Chater, P.; Hanna, J. V.; Nellist, P.; Tsang, S. C. E. *J Am Chem Soc* **2019,** 141, (50), 19616-19624.

19. Lv, H.; Xu, D.; Sun, L.; Henzie, J.; Suib, S. L.; Yamauchi, Y.; Liu, B. *ACS Nano* **2019,** 13, (10), 12052-12061.

20. Babu, P.; Mohanty, S.; Naik, B.; Parida, K. *ACS Applied Energy Materials* **2018,** 1, (11), 5936-5947.

21. Liu, J.; Jia, J.; Li, S.; Chang, Y.; Guo, S.; Yue, T.; Jia, M. *Journal of Alloys and Compounds* **2023,** 948, 169779.

22. Guo, F.; Li, X.; Sun, J.; Ji, S.; Li, Q.; Duan, X.; Ma, J.-f. *International Journal of Hydrogen Energy* **2024,** 53, 273-279.

23. Zhang, G.; Hui, C.; Yang, Z.; Wang, Q.; Cheng, S.; Zhang, D.; Cui, P.; Shui, J. *Applied Catalysis B: Environmental* **2024,** 342, 123377.

24. Kong, F.; Liu, X.; Song, Y.; Qian, Z.; Li, J.; Zhang, L.; Yin, G.; Wang, J.; Su, D.; Sun, X. *Angew Chem Int Ed Engl* **2022,** 61, (42), e202207524.

25. Shen, H.; Wang, Y.; Chakraborty, T.; Zhou, G.; Wang, C.; Fu, X.; Wang, Y.; Zhang, J.; Li, C.; Xu, F.; Cao, L.; Mueller, T.; Wang, C. *ACS Catalysis* **2022,** 12, (9), 5275-5283.

26. Chattot, R.; Asset, T.; Bordet, P.; Drnec, J.; Dubau, L.; Maillard, F. *ACS Catalysis* **2016,** 7, (1), 398-408.

27. Li, H.; Shin, K.; Henkelman, G. *J Chem Phys* **2018,** 149, (17), 174705.

28. Guo, J.; Gao, L.; Tan, X.; Yuan, Y.; Kim, J.; Wang, Y.; Wang, H.; Zeng, Y. J.; Choi, S. I.; Smith, S. C.; Huang, H. *Angew Chem Int Ed Engl* **2021,** 60, (19), 10942-10949.

29. Feng, Y.; Bu, L.; Guo, S.; Guo, J.; Huang, X. *Small* **2016,** 12, (33), 4464-70.

30. Luo, S.; Tang, M.; Wu, X.; Ou, Y.; Wang, Z.; Jian, N.; Li, X.; Lin, Y.; Yan, Y.; Huang, J.; Zhang, H.; Yang, D. *CrystEngComm* **2019,** 21, (2), 290-296.

31. Sun, L.; Lv, H.; Wang, Y.; Xu, D.; Liu, B. *J Phys Chem Lett* **2020,** 11, (16), 6632-6639.

32. Lao, X.; Liao, X.; Chen, C.; Wang, J.; Yang, L.; Li, Z.; Ma, J. W.; Fu, A.; Gao, H.; Guo, P. *Angew Chem Int Ed Engl* **2023,** 62, (31), e202304510.

33. Fang, Y.; Guo, S.; Cao, D.; Zhang, G.; Wang, Q.; Chen, Y.; Cui, P.; Cheng, S.; Zuo, W. *Nano Research* **2022,** 15, (5), 3933-3939.

34. Lao, X.; Sun, T.; Zhang, X.; Pang, M.; Fu, A.; Guo, P. *ACS Sustainable Chemistry & Engineering* **2022,** 10, (20), 6843-6852.

35. Wang, Y.; Zheng, M.; Li, Y.; Ye, C.; Chen, J.; Ye, J.; Zhang, Q.; Li, J.; Zhou, Z.; Fu, X. Z.; Wang, J.; Sun, S. G.; Wang, D. *Angew Chem Int Ed Engl* **2022,** 61, (12), e202115735.

36. Ai, X.; Zou, X.; Chen, H.; Su, Y.; Feng, X.; Li, Q.; Liu, Y.; Zhang, Y.; Zou, X. *Angew Chem Int Ed Engl* **2020,** 59, (10), 3961-3965.

37. Gao, L.; Li, X.; Yao, Z.; Bai, H.; Lu, Y.; Ma, C.; Lu, S.; Peng, Z.; Yang, J.; Pan, A.; Huang, H. *J Am Chem Soc* **2019,** 141, (45), 18083-18090.

38. Ji, L.; Che, H.; Qian, N.; Li, J.; Luo, S.; Li, X.; Wu, X.; Xu, Q.; Gong, X.; Cui, X.; Zhang, H.; Yang, D. *Applied Catalysis B: Environmental* **2023,** 328, 122521.

Chapter 5. Controlling the Morphology of High-Entropy Alloys Nanoparticles

5.1 Introduction

Over the last several years, high-entropy alloys (HEAs) have garnered significant interest for their application in nanotechnology, particularly for water electrolysis.[1-5] HEAs are generally composed of five or more elements, each present in a relatively high concentration ranging from 5 to 35 atomic percent, within a solid solution phase. The distinctive attributes of HEAs, such as the high-entropy effect, lattice distortion effect, sluggish diffusion effect, and the cocktail effect, provide excellent prospects for the development of innovative catalysts.

The high-entropy effect is thought to contribute to the formation of simple solid solution structures (e.g., face-centered cubic (FCC), body-centered cubic (BCC), or hexagonal close-packed (HCP) structures) rather than the complex structures that are typically favored in lower-entropy alloys.[6-8] The presence of multiple principal elements of different atomic sizes, HEAs exhibit significant lattice distortion. This distortion affects the mechanical properties of the alloy, such as strength and hardness, by impeding dislocation motion through the lattice. Lattice distortion can also impact other properties like electrical and thermal conductivity. The sluggish diffusion effect occurs from diverse atomic sizes and the complex microstructure in HEAs. This can enhance the high-temperature stability of HEAs, making them resistant to grain growth and phase separation at elevated temperatures. Sluggish diffusion is beneficial for maintaining the alloy's microstructural stability and mechanical properties under thermal exposure. The cocktail effect allows for the tailoring of alloys with specific properties for various applications, leveraging the strengths of each constituent element. These characteristic properties make high-entropy alloys promising materials for a wide range of applications, including aerospace, automotive, defense, and energy sectors, where materials are required to operate under extreme conditions of stress, temperature, and corrosive environments.[9-12]

The synthesis strategy for fabricating HEAs originates from a complex methodology. This complexity, inherent in multicomponent alloys, often leads to inhomogeneous compositions and challenges the creation of single-phase HEAs. With the advent of nanotechnology, there has been an increase in research efforts aimed at developing fabrication techniques for innovative functional materials at the nanoscale. Recently, solution-phase synthesis methods have become promising for generating HEA nanostructures with varied morphologies, including nanowires, nanosheets, nanoribbons, and nanoplates. However, despite these advancements, such methods, encompassing both one-pot and galvanic-reaction-induced syntheses, encounter limitations due to their narrow scope of application and the challenges in achieving uniform element distribution within the HEAs.[13-15]

Wet-chemistry synthesis, a category of facile synthetic strategies, emerges as a potent solution to this challenge. This approach allows for the precise manipulation of the composition and morphology of HEAs at the nanoscale, facilitating the enhancement of their catalytic performance. By employing wet-chemistry techniques, researchers can control the nucleation and growth processes of HEAs, enabling the formation of nanoparticles, nanowires, or other nanostructures with specific surface properties and active sites optimized for HER.[16-20] In this study, the control over HEAs's morphology through wet-chemistry methods to form nanosheets and nanowires with similar composition was achieved. Additionally, using wet-chemistry methods not only paves the way for improved catalytic activity and stability but also opens up new avenues for the design of efficient and durable catalysts for hydrogen production. As the demand for sustainable and green energy solutions intensifies, the development of facile synthetic strategies for tailoring the properties of HEAs represents a significant step forward in the quest for advanced materials capable of driving the hydrogen economy.

5.2 Experimental Methods

5.2.1 Chemical and materials

Palladium(II) acetylacetonate ($Pd(acac)_2$, 99.9%), platinum(II) acetylacetonate ($Pt(acac)_2$, 99.9%), iron(III) acetylacetonate ($Ir(acac)_3$, 99,9%), cobalt(III) acetylacetonate ($Co(acac)_3$, 99.9%), nickel(II) acetylacetonate ($Ni(acac)_2$, 95%), ruthenium(III) acetylacetonate ($Ru(acac)_3$, 97%), molybdenum hexacarbonyl ($Mo(CO)_6$, 99.9%), ammonium bromide (NH_4Br, 99.9%), propionic acid ($C_3H_6O_2$, 99.5%), sodium borohydride ($NaBH_4$, 99%), isopropanol (9.9%) and Nafion perfluorinated resin solution (5 wt%) were obtained from Sigma-Aldrich. D-glucose ($C_6H_{12}O_6$, 99-100%) was purchased from Thermo Fisher Scientific. Oleylamine (OAm, 50%) was obtained from TCI chemical. Potassium hydroxide (KOH, 95.0%) was obtained from Samchun. Other chemicals were reagent grade, and deionized water with a resistivity of greater than 18.3 MΩ·cm was used in the preparation of reaction solutions. Hexane was of technical grade.

5.2.2 Synthesis of PdPtFeCoNi HEA Nanosheets

0.01 mmol of $Pd(acac)_2$, 0.01 mmol of $Pt(acac)_2$, 0.028 mmol of $Fe(acac)_3$, 0.038 mmol of $Co(acac)_3$, 0.027 mmol of $Ni(acac)_2$, 0.0125 mmol of $Ru(acac)_3$, 0.037 mmol of $Mo(CO)_6$, 0.510 mmol of NH_4Br, 0.334 mmol of D-glucose, and 5 mL of OAm were mixed in a 30 mL vial. The mixture was sonicated until it dissolved, then the glass vial was transferred into the water bath and heated from room temperature to 200^{o}C for 5-hour 30 min. The solution was washed with a mixture of hexane and ethanol (1:1) several times.

5.2.3 Synthesis of PdPtFeCoNi HEA Nanowires

0.01 mmol of $Pd(acac)_2$, 0.01 mmol of $Pt(acac)_2$, 0.028 mmol of $Fe(acac)_3$, 0.038 mmol of $Co(acac)_3$, 0.027 mmol of $Ni(acac)_2$, 0.0125 mmol of $Ru(acac)_3$, 0.037 mmol of $Mo(CO)_6$, 2.11 mmol of $NaBH_4$, 100 µL of propionic acid, 0.334 mmol of D-glucose, and 5 mL of OAm were mixed in a 30 mL vial. The mixture was sonicated until it dissolved, then the glass vial was transferred into the water bath and heated from room temperature to 200^{o}C for 5-hour 30 min. The solution was washed with a mixture of hexane and ethanol (1:1) several times.

5.2.4 Synthesis of PdPtFeCoNi HEA Nanoparticles

0.01 mmol of $Pd(acac)_2$, 0.01 mmol of $Pt(acac)_2$, 0.028 mmol of $Fe(acac)_3$, 0.038 mmol of $Co(acac)_3$, 0.027 mmol of $Ni(acac)_2$, 0.0125 mmol of $Ru(acac)_3$, and 5 mL of OAm were mixed in a 30 mL vial. The mixture was sonicated until it dissolved, then the glass vial was transferred into the water bath and heated from room temperature to 200^{o}C for 5-hour 30 min. The solution was washed with a mixture of hexane and ethanol (1:1) several times.

5.2.5 Electrochemical measurement

Electrochemical measurements were carried out using EC-Lab Biologic Model SP-300 electrochemical workstation in a standard three-electrode system. Graphite was employed as the counter electrode and a Hg/HgO (1 M KOH) electrode served as the reference electrode. The PdPtFeCoNi HEA nanosheets, nanowires and nanoparticles were loaded onto a carbon support (Vulcan XC 72R) before estimating their electrocatalytic properties. Catalyst ink was prepared by dispersing certain amounts of catalysts in a mixture of 2-propanol, deionized water (DIW), and Nafion (5 wt.%) with a ratio of 4:1: 0.025 to make a catalyst ink of 4 $\mu g_{metal}\ \mu L^{-1}$. For the preparation of the working electrode, 10 μL of catalyst ink was applied to carbon electrode (1 cm^2) and allowed to dry naturally at room temperature. The precise amount of metal loaded on the carbon plate elecrode was determined by inductively coupled plasma-optical emission spectroscopy (ICP-OES). All potentials were converted with respect to a reversible hydrogen electrode (RHE) in Ar-saturated 1.0 MKOH. Prior to recording LSV curves, CV was conducted at scan rates of 50 mVs^{-1}, ranging from 0.1 to 1.3 V (vs. RHE) until CV curves were stabilized. For HER experiments, LSV curves were obtained at a scan rate of 5 mVs^{-1}. EIS measurements were conducted at –200 mV (vs. RHE) over a frequency range from 1 to 10 MHz.

5.2.6 Characterizations

Transmission electron microscopy (TEM) and scanning electron microscopy (SEM) images of the prepared catalysts were obtained by using a JEOL JEM-2100F and a JEOL JEM-7210F, respectively. SEM analysis was done by using (used instrument) at total-period analysis center for Ulsan chemical industry of Korea Basic Science Institute (KBSI). ICP-OES measurement was conducted using a Spectrouble-ICP-OES (Ametek). X-ray diffraction (XRD) measurement was conducted on a Rigaku D/MAX2500V/PC. X-ray photoelectron spectroscopy (XPS) measurements were conducted using a Thermo VG Scientific Sigma Probe spectrometer with Al Kα X-ray (1486.6 eV) as a light source. XPS data were calibrated using the C 1 s peak at 284.5 eV.

5.3 Result and Discussion

5.3.1 Synthesis and Characterization of PdPtFeCoNi HEA NSs and HEA NWs

The PdPtFeCoNi HEA was produced using a facile one-pot synthetic strategy. Figure 1 presents a schematic illustration of the fabrication process for PdPtFeCoNi HEA NSs, NWs, and nanoparticles (NPs). The metal precursors, consisting of Pd(acac)$_2$, Pt(acac)$_2$, Fe(acac)$_3$, Co(acac)$_3$, and Ni(acac)$_2$, were chosen for the composition of the HEA catalysts. Specific reductants, surfactants, and shape-directing agents play crucial roles in forming various HEA morphologies. For the synthesis of PdPtFeCoNi HEA NSs, Mo(CO)$_6$, NH$_4$Br, and D-glucose were used. In contrast, the formation of PdPtFeCoNi HEA NWs employed propionic acid, NaBH$_4$, and D-glucose. However, the production of PdPtFeCoNi HEA NPs did not involve any surfactant or reductant, utilizing only oleylamine. The structural composition of the PdPtFeCoNi HEA NSs and NWs was characterized through high-resolution transmission electron microscopy (HR-TEM). Figure 2a displays the morphology of PdPtFeCoNi HEA NSs formed as hexagonal sheets with an average diameter of 70.99 ± 9.38 nm. The elemental mapping images obtained by HR-TEM, combined with energy-dispersive X-ray spectroscopy (HR-TEM-EDS), revealed that the composition of PdPtFeCoNi HEA NSs includes Pd, Pt, Fe, Co, and Ni elements (Figure 2c). Additionally, the crystal structure of the PdPtFeCoNi HEA NSs exhibits a face-centered cubic (fcc) lattice, as characterized by X-ray diffraction (XRD) (Figure 3a). For the PdPtFeCoNi HEA NWs, the morphology of the nanowires exhibits a thickness of around 6.38 ± 1.66 nm with a longer dimension (Figure 4a). The EDS mapping image of the PdPtFeCoNi HEA NWs also revealed the presence of Pd, Pt, Fe, Co, and Ni elements. Furthermore, a similar fcc structure was confirmed for the PdPtFeCoNi HEA NWs, as displayed in Figure 3b. However, the XRD peaks exhibited broadening, indicating the formation of a high-entropy alloy. The atomic ratio of each element was determined by EDS mapping and presented in Table 1. The PdPtFeCoNi HEA NPs were fabricated for morphology comparison in applications toward hydrogen evolution reaction (Figure 5).

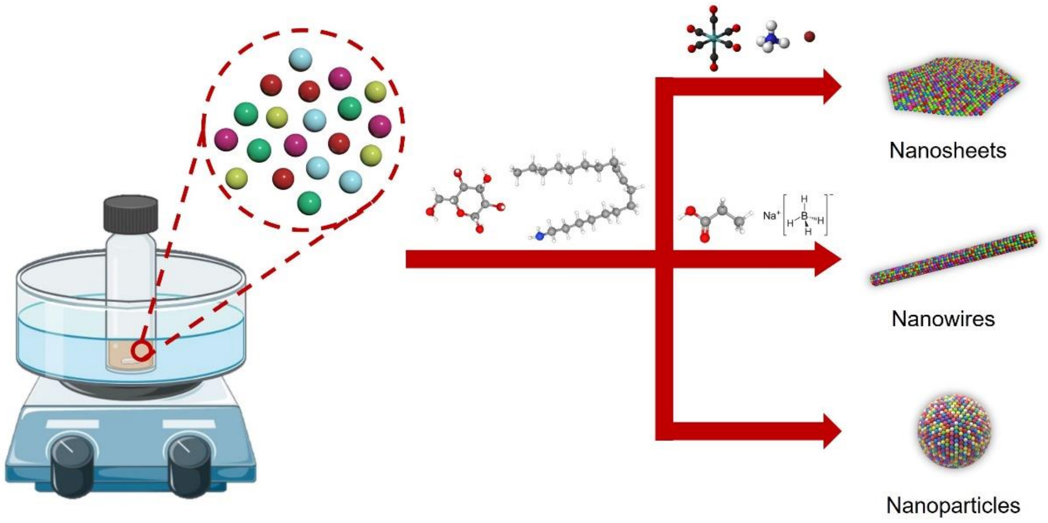

Figure 1. Schematic illustration to the formation of PdPtFeCoNi HEA nanostructures.

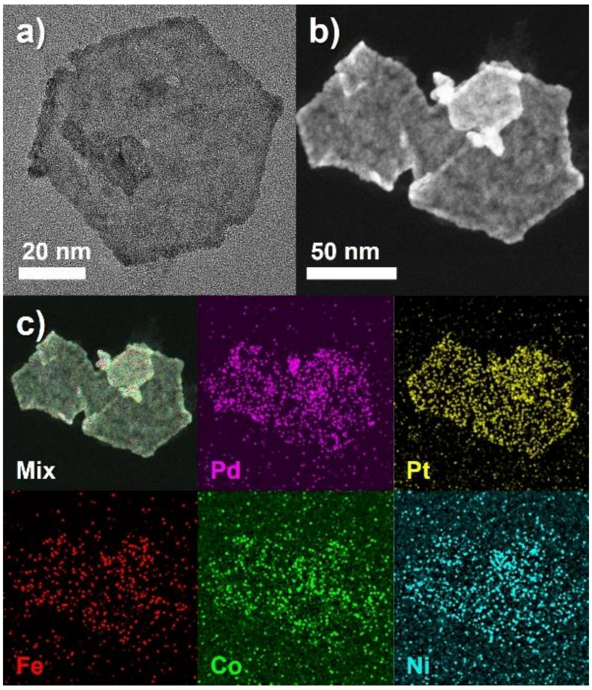

Figure 2. a) TEM image, b) HR-TEM image, c) HR-TEM-EDS elemental mapping images of PdPtFeCoNi HEA NSs.

Table 1. Atomic percentage of Pd, Pt, Fe, Co, and Ni elements of PdPtFeCoNi HEA NSs, NWs, and NPs measured by HR-TEM-EDS.

Element	**Atomic %**		
	PdPtFeCONi HEA NSs	**PdPtFeCONiHEA NWs**	**PdPtFeCONiHEA NPs**
Pd	28.93	13.56	21.21
Pt	30.90	19.45	22.96
Fe	15.91	20.43	21.45
Co	10.29	38.40	22.08
Ni	13.97	8.16	12.30

To elucidate the formation mechanism of PdPtFeCoNi HEA NSs, the structural evolution process was explored by examining the effects of varying concentrations of shape-directing agents such as NH_4Br, and $Mo(CO)_6$. NH_4Br is crucial for the formation of well-defined nanosheets. Without NH_4Br, only nanoparticles were produced, highlighting NH_4Br is critical role in nanosheet synthesis. Although increasing NH_4Br concentrations from 51 to 204 mM facilitated the growth of nanosheets, there were no significant changes in their size, even with elevated concentrations of NH_4Br. 102 mM of NH_4Br was used as the standard method. This finding indicates that while NH_4Br is necessary for nanosheet formation, its concentration does not significantly impact their size. Furthermore, $Mo(CO)_6$ played a crucial role in determining the structural dimensions of the nanosheets (Figure 6e-h). In experiments devoid of $Mo(CO)_6$, no nanosheets were produced; only nanoparticles were observed. Conversely, increasing the concentration of $Mo(CO)_6$ from 3.78 to 37.80 mM led to a decrease in the size of the nanosheets, demonstrating its pivotal role in controlling the dimensions of these structures. $Mo(CO)_6$ generates CO, which can absorb onto the surface of Pd or Pt, influencing the nucleation rate. 7.50 mM of $Mo(CO)_6$ was used as the standard method. In contrast, D-glucose served as a reducing agent that influenced the growth rate and morphology of the nanosheets (Figure 7). In the absence of D-glucose, nanosheets with a porous structure were formed. However, as the concentration of D-glucose increased from 33 to 555 mM, the nanosheets became more well-defined and larger in size, indicating a direct relationship between D-glucose concentration and nanosheet size (Table 2). A higher concentration of D-glucose can influence the reduction rate, which can accelerate the growth rate in the nucleation stage, leading to the production of larger nanosheets. 66 mM of D-glucose was used as the standard method. Based on these finding, the different lateral size of PdPtFeCoNi HEA NSs was evaluated for HER. This comprehensive study of the effects of shape-directing agents and reducing agent provides critical insights into the tailored synthesis of PdPtFeCoNi HEA NSs, highlighting the importance of each component in achieving desired nanosheet characteristics.

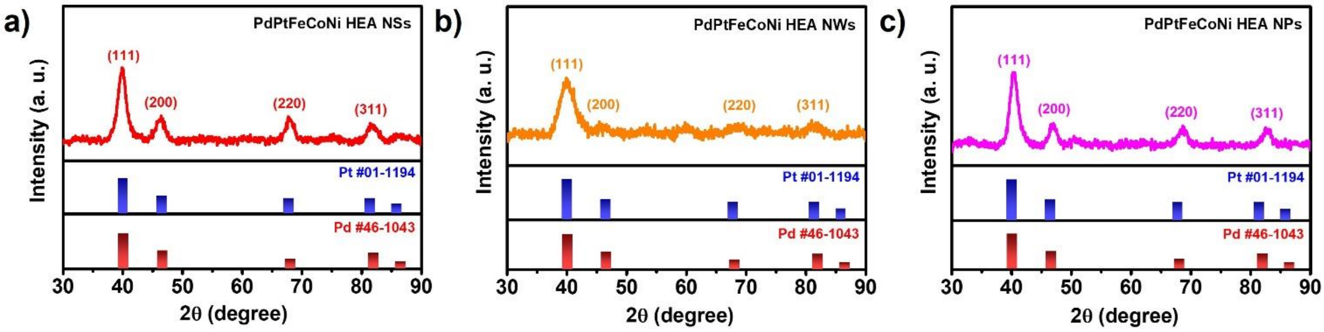

Figure 3. XRD pattern of a) PdPtFeCoNi HEA NSs, b) a) PdPtFeCoNi HEA NWs, and c) PdPtFeCoNi HEA NPs.

Building on these insights, further experimentation was conducted to understand the influence of the metal precursors Pd(acac)$_2$ and Pt(acac)$_2$ on nanosheet formation. The control morphology was evaluated using 1-, 3-, and 5-mM concentrations of Pd and Pt precursors. It was found that the presence of Pd(acac)$_2$ is indispensable for the synthesis of nanosheets. In its absence, only nanoparticles were observed, underscoring Pd is critical role in initiating nanosheet morphology (Figure 8a). However, increasing the concentration of Pd(acac)$_2$ from 1 to 5 mM did not further influence the morphology, indicating that its primary role is in the nucleation phase rather than growth modulation (Figure 8b-d). On the other hand, Pt(acac)$_2$ demonstrated less sensitivity to concentration changes (Figure 8e-h). Nanosheets were successfully synthesized across a spectrum of low to high Pt(acac)$_2$ concentrations, suggesting that while Pt is supportive of the nanosheet structure, it is not as critical as Pd in driving the initial morphological development. These observations indicate that Pd plays a more catalytic-like role in the nanosheet formation, essential for nucleation, whereas Pt may contribute more to the growth and stabilization phases.[21-24] Additionally, the ability to form nanosheets using various combinations of three or four different metallic elements highlights the robust nature of the high-entropy alloys, where the synergy between different elements facilitates the maintenance of desired structural properties without compromising the quality or morphology of the nanosheets (Figure 9). This adaptability is crucial for applications requiring specific nanostructures, offering a pathway for tailored material synthesis that can be optimized for unique applications in nanotechnology.

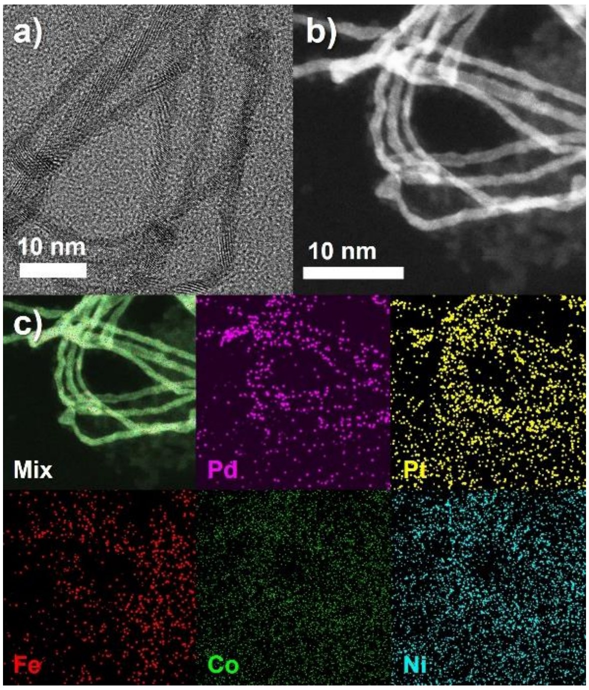

Figure 4. a) TEM image, b) HR-TEM image, c) HR-TEM-EDS elemental mapping images of PdPtFeCoNi HEA NWs.

To understand the formation mechanisms of PdPtFeCoNi HEA NWs and the influence of different types of acids on their synthesis were evaluated. The experiments revealed significant differences in the yield and morphology of the resulting nanomaterials based on the type of acid used. Propionic acid, with its intermediate chain length (three carbon atoms), was found to facilitate a high yield of HEA NWs. In contrast, acetic acid (with two carbon atoms) and hexanoic acid (with six carbon atoms) predominantly produced smaller nanoparticles rather than the desired nanowires (Figure 10a-c). Furthermore, in Figure 10d-f, when the pH of the solutions was adjusted to 2.07 for all three types of acids such as acetic, propionic, and hexanoic acid, the formation of nanowires became the dominant morphology. This uniform pH level likely mitigates some of the intrinsic differences in the acid properties by equalizing the protonation state and the charge environment around the metal ions. This pH adjustment could enhance the acids's ability to coordinate with the metal ions, similarly, promoting a more uniform nucleation and elongation process necessary for nanowire growth.

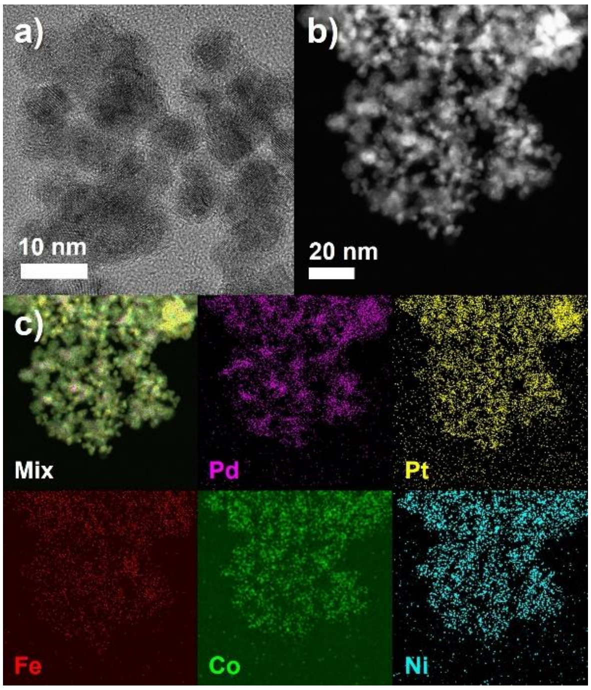

Figure 5. a) TEM image, b) HR-TEM image, c) HR-TEM-EDS elemental mapping images of PdPtFeCoNi HEA NPs.

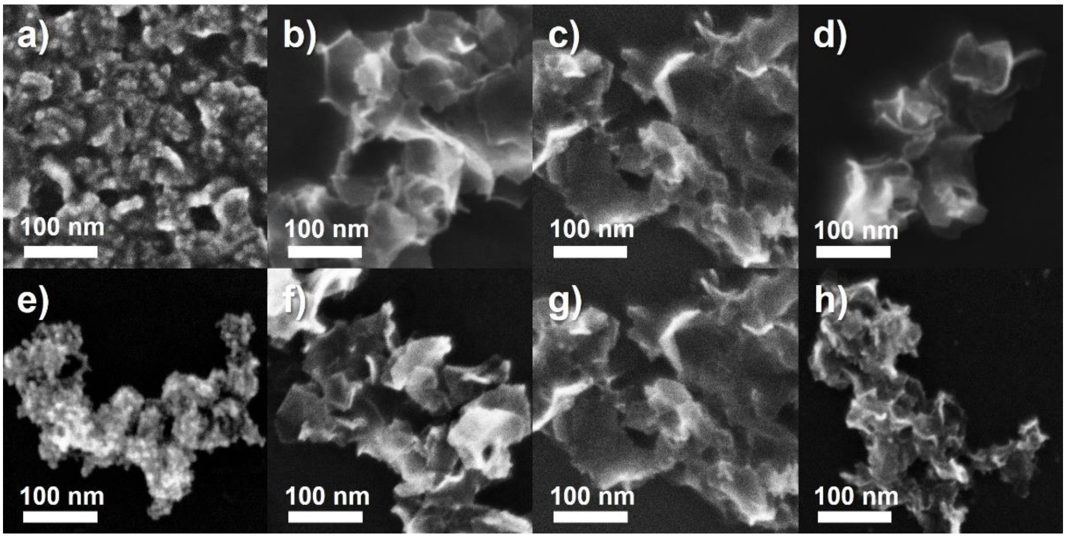

Figure 6. SEM images of PdPtFeCoNi HEA NSs produced in reaction mixture with a) 0, b) 51, c) 102, and d) 204 mM of NH_4Br, e) 0, f) 3.78, g) 7.50, and h) 37.80 mM of $Mo(CO)_6$.

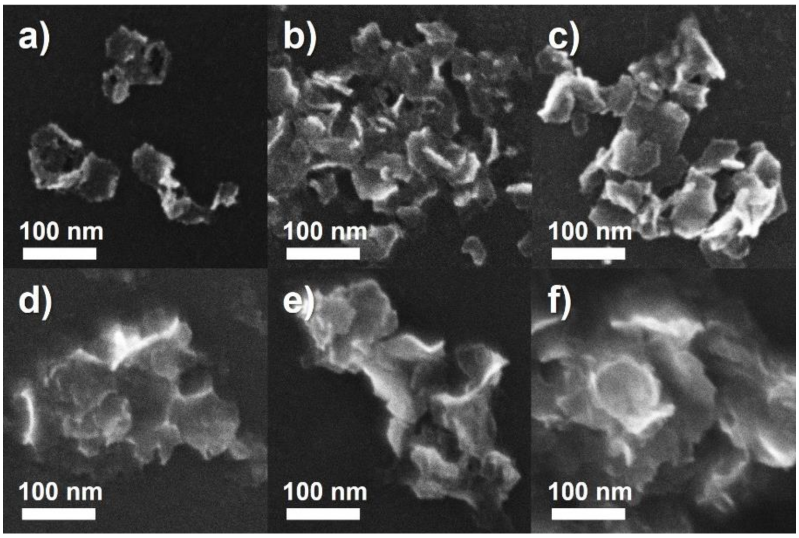

Figure 7. SEM images of PdPtFeCoNi HEA NSs produced in different concentration of D-glucose a) 0, b) 33, c) 66, d) 133, e) 266, and f) 555 mM.

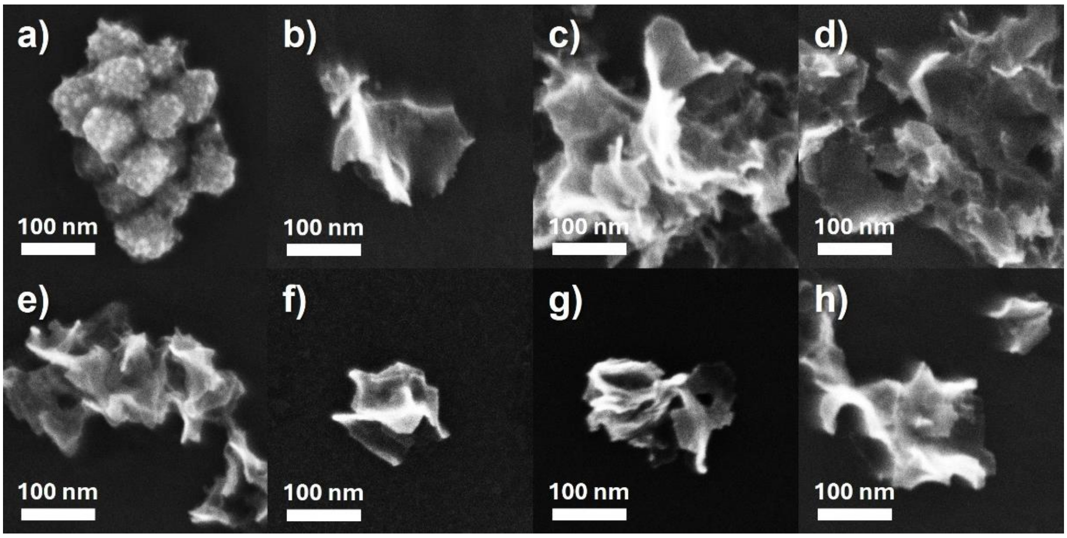

Figure 8. SEM images of PdPtFeCoNi HEA NSs produced in reaction mixture with a) 0, b) 1, c) 3, and d) 5 mM of Pd(acac)$_2$, e) 0, f) 1, g) 3, and h) 5 mM of Pt(acac)$_2$.

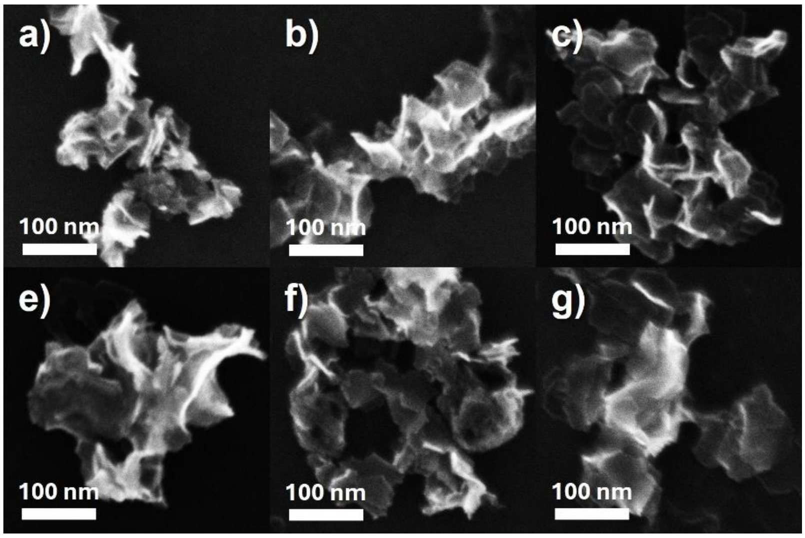

Figure 9. SEM images of elemental composition in HEA NSs with a) PdPtFe, b) PdPtCo, c) PdPtNi, d) PdPtFeCo, e) PdPtFeNi, and f) PdPtCoNi.

To elucidate the role of $NaBH_4$, and propionic acid in the formation of PdPtFeCoNi HEA NWs, their effects as reductants and surfactants were systematically investigated, building upon the understanding of acid-mediated synthesis. $NaBH_4$ is a strong reducing agent, crucial for the reduction of metal precursors to their metallic states. In the absence of $NaBH_4$, no reduction occurs, preventing the formation of metallic nanowires; instead, the metal salts may persist as unreacted precursors or form other types of aggregates. Increasing concentrations of $NaBH_4$ from 211, 422, and 845 mM can accelerate the reduction process, providing more electrons that facilitate the nucleation and growth of nanowires (Figure 11a-d). 422 mM of $NaBH_4$ was used as the standard method. The increased availability of reduced metal atoms encourages the formation of elongated structures, as there is a sustained reduction driving the directional growth necessary for nanowire formation. Furthermore, Propionic acid acts primarily as a pH adjustment and shape-directing agent in this synthesis. In 0 mM of propionic acid leads to the formation of smaller nanoparticles due to the lack of directional growth control and stabilization of the nanowire morphology. With an optimal amount of propionic acid (268 mM), the acid molecules likely orient themselves along the growing nanowires, effectively capping and guiding their growth (Figure 11e-h). This results in a higher yield of well-defined nanowires. However, excessive amounts of propionic acid could oversaturate the reaction mixture, potentially leading to competitive adsorption at the nanowire surfaces. This might inhibit further growth or lead to the formation of disordered structures rather than well-defined nanowires. In addition, D-glucose, while a milder reductant compared to $NaBH_4$, plays a multifaceted role to regulate different thickness of nanowires. In its absence, less effective reduction of metal ions leads predominantly to the formation of nanoparticles, where the reduction might be incomplete or inconsistent. Adding D-glucose and increasing its concentration from 33, 66, 133, 266, and 555 mM can improve the reduction process, offering a more controlled and sustained release of electrons (Figure 12). Interestingly, the addition of D-glucose into the synthetic method leading to increase the thickness of PdPtFeCoNi HEA NWs (Table 3). 66 mM of D-glucose was used as the standard method. This aids in a steady growth phase, fostering the elongation of structures into nanowires. D-glucose may also impact the viscosity and surface tension of the solution, affecting the mobility of ions and the stabilization of the growing nanowire structures.

From these finding, the different thickness of PdPtFeCoNi HEA NWs was evaluated for HER. Taken together, these observations underscore the intricate balance and interplay between the chemical reagents used in the synthesis. The coordination of reducing power and surface activity directly influences the nucleation and elongational growth of PdPtFeCoNi HEA NWs, highlighting the importance of carefully controlling each component's concentration to achieve desired nanostructures.

Table 2. Average diameter of PdPtFeCoNi HEA NSs with different concentration of D-glucose.

Concentration of D-glucose	Average diameter
33 mM	52.06 ± 9.68 nm
66 mM	70.99 ± 9.38 nm
133 mM	75.31 ± 14.55 nm
266 mM	89.91 ± 14.49 nm
555 mM	126.03 ± 18.84 nm

Table 3. Average diameter of PdPtFeCoNi HEA NWs with different concentration of D-glucose.

Concentration of D-glucose	Average thickness
33 mM	5.33 ± 1.18 nm
66 mM	6.38 ± 1.66 nm
133 mM	8.57 ± 1.92 nm
266 mM	8.66 ± 1.49 nm
555 mM	10.29 ± 2.32 nm

Based on these findings, the study comprehensively demonstrates the critical influence of reductants and shape-directing agents on the synthesis of PdPtFeCoNi HEA NSs and NWs. The delicate balance between these components is crucial for achieving optimal synthesis conditions, thus enabling precise control over the morphology and size of the high-entropy alloy nanostructures. This study not only sheds light on the nuanced roles of these chemical agents in nanomaterial synthesis but also provides a foundation for tailoring the properties of HEA NSs and NWs for specific applications in catalysis.

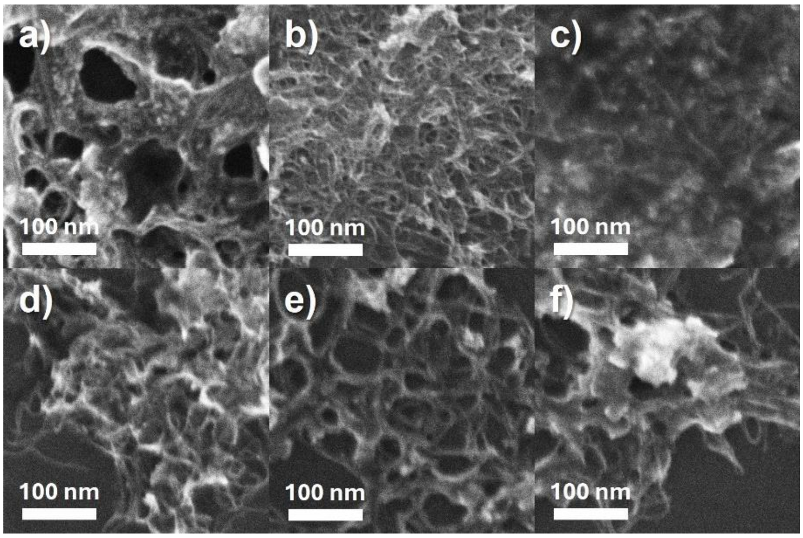

Figure 10. SEM images of PdPtFeCoNi HEA NWs produced in reaction mixture with a) acetic acid, b) propionic acid, c) hexanoic acid, and similar pH of ~2.07 from different type of acid d) acetic acid, e) propionic acid, and f) hexanoic acid.

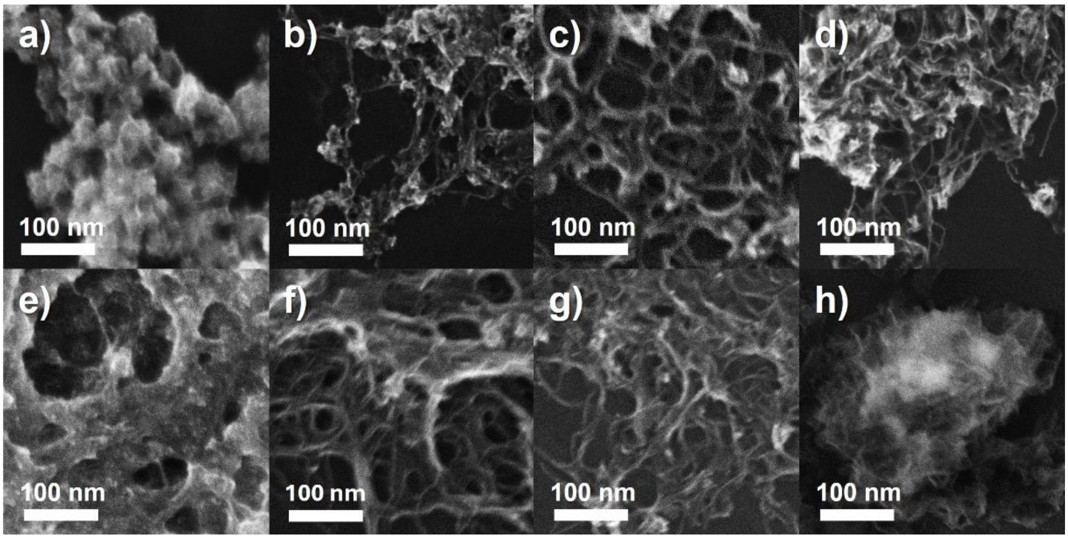

Figure 11. SEM images of PdPtFeCoNi HEA NSs produced in reaction mixture with a) 0, b) 211, c) 422, and d) 845 mM of $NaBH_4$, e) 0, f) 134, g) 268, and h) 1340 mM of propionic acid.

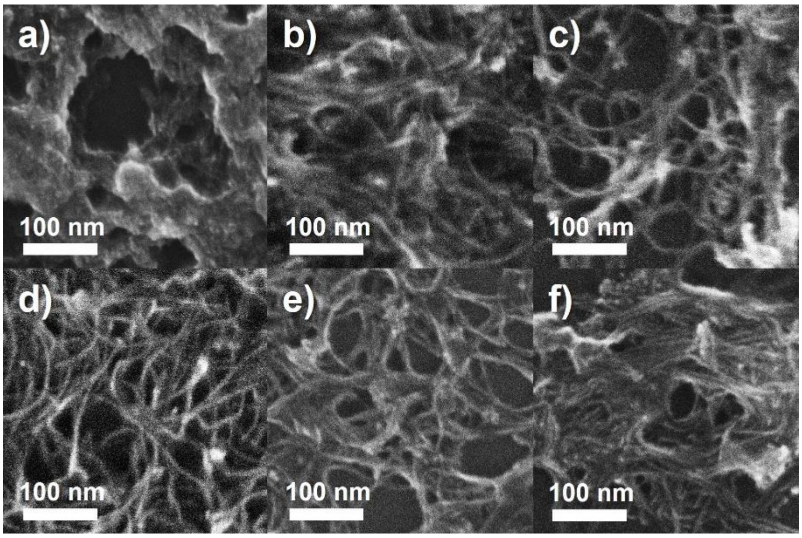

Figure 12. SEM images of PdPtFeCoNi HEA NWs produced in different concentration of D-glucose a) 0, b) 33, c) 66, d) 133, e) 266, and f) 555 mM.

5.3.2 Application of PdPtFeCoNi HEA NSs and NWs for HER

The electrochemical performance of PdPtFeCoNi HEA NSs, NWs, and NPs was assessed for HER to explore the influence of morphology on catalytic activity. The electrocatalytic HER performances of the catalysts were evaluated in a typical three-electrode system with N_2-saturated 1.0 M KOH as the electrolyte. The PdPtFeCoNi HEA NSs were first evaluated to check the influence of the lateral size of the nanosheets on the HER catalytic activity. Linear sweep voltammetry (LSV) curves and Tafel slope for different concentrations of D-glucose are shown in Figure 13. The increasing concentration of glucose led to an increase in the size of the nanosheets; consequently, it was observed that an increase in size led to lower activity. Meanwhile, 33 mM of D-glucose possessed higher activity compared to other concentrations (Table 4). Smaller nanosheets typically have a higher surface area-to-volume ratio, providing more active sites for the hydrogen evolution reaction. This increase in active sites can enhance the catalytic efficiency as more reaction sites are available per unit of mass. Additionally, smaller nanosheets may facilitate better electron transport and reduce diffusional limitations, leading to faster reaction kinetics. This is particularly beneficial in electrocatalytic processes like HER, where the speed and efficiency of electron transfer are crucial for high performance.

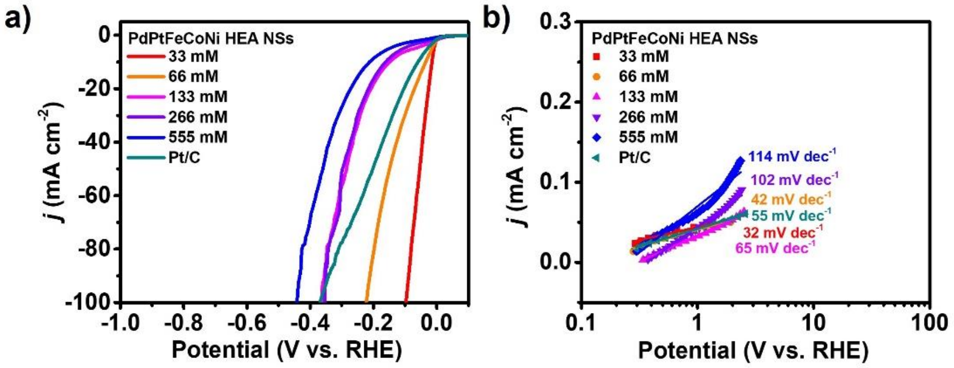

Figure 13. a) HER polarization curve of PdPtFeCoNi HEA NSs with different D-glucose concentrations in 1 M KOH, and b) Tafel plots of all catalysts.

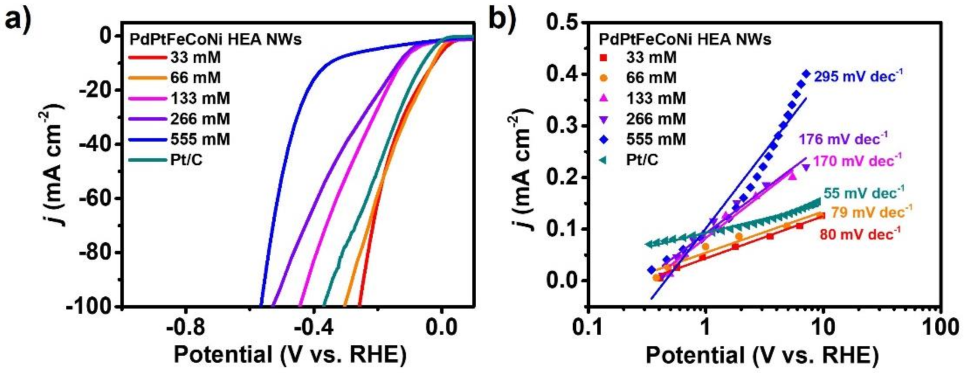

Figure 14. a) HER polarization curve of PdPtFeCoNi HEA NWs with different D-glucose concentrations in 1 M KOH, and b) Tafel plots of all catalysts**.**

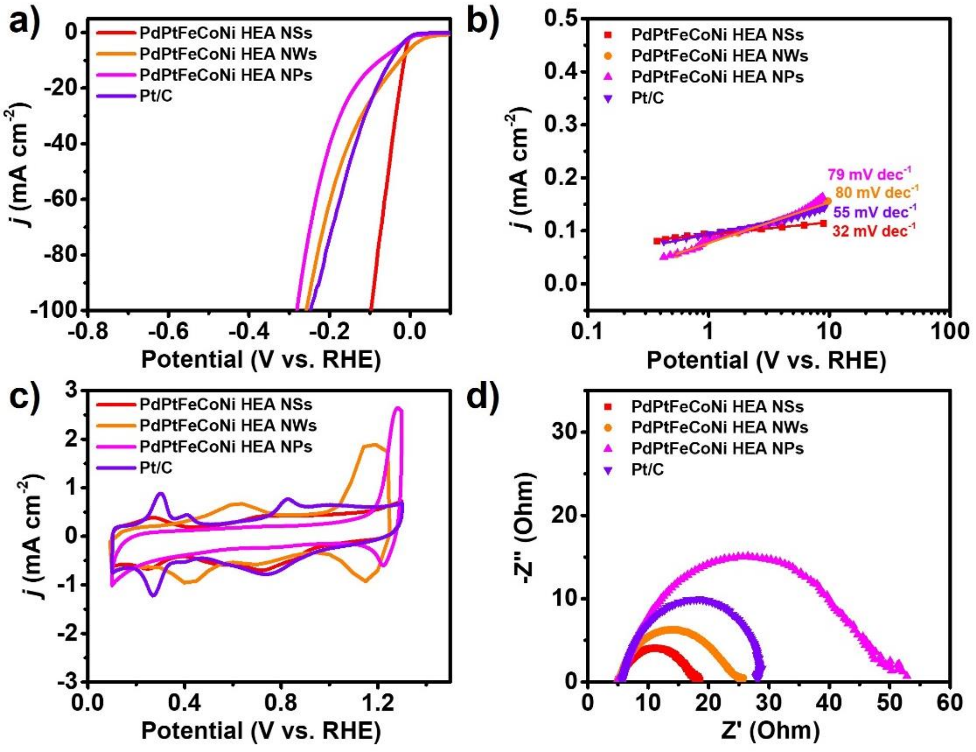

Figure 15. a) HER polarization curve of all catalysts in 1 M KOH, b) Tafel plots of all catalysts, c) CV of all catalysts, and d) Nyquist plots for various catalysts in 1.0 M KOH at 0.02 V vs RHE.

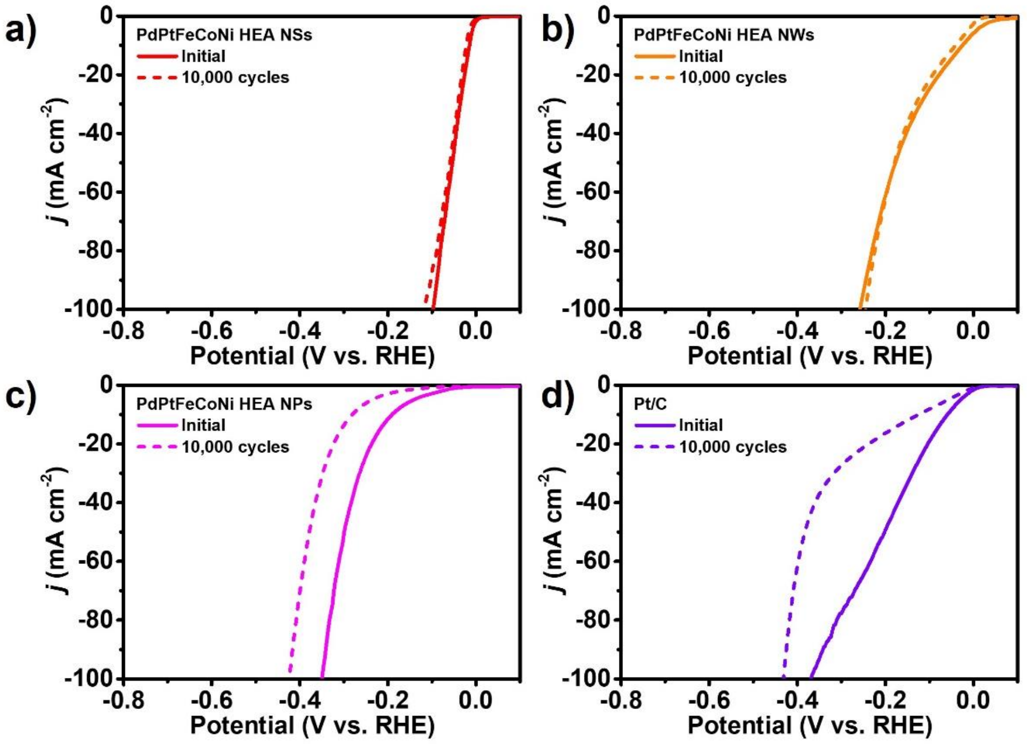

Figure 16. a-d) HER polarization curve of all catalysts in 1 M KOH at 50 mA cm^{-2} initial and after 10.000 cycles of PdPtFeCoNi HEA NSs, PdPtFeCoNi HEA NWs, PdPtFeCoNi HEA NPs, and Pt/C.

Table 4. HER performance of PdPtFeCoNi HEA NSs with different concentration of D-glucose.

Concentration of D-glucose	Average diameter	Overpotential at -10 mA cm^{-2}	Tafel slope
33 mM	46.46 ± 8.55 nm	14 mV	32 mV dec^{-1}
66 mM	70.99 ± 9.38 nm	34 mV	42 mV dec^{-1}
133 mM	75.31 ± 14.55 nm	149 mV	65 mV dec^{-1}
266 mM	89.91 ± 14.49 nm	162 mV	102 mV dec^{-1}
555 mM	126.03 ± 18.84 nm	212 mV	114 mV dec^{-1}
Pt/C	/	60 mV	55 mV dec^{-1}

Table 5. HER performance of PdPtFeCoNi HEA NWs with different concentration of D-glucose.

Concentration of D-glucose	Average thickness	Overpotential at -10 mA cm^{-2}	Tafel slope
33 mM	5.33 ± 1.18 nm	26 mV	80 mV dec^{-1}
66 mM	6.38 ± 1.66 nm	26 mV	79 mV dec^{-1}
133 mM	8.57 ± 1.92 nm	125 mV	170 mV dec^{-1}
266 mM	8.66 ± 1.49 nm	135 mV	176 mV dec^{-1}
555 mM	10.29 ± 2.32 nm	349 mV	295 mV dec^{-1}
Pt/C	/	60 mV	55 mV dec^{-1}

Table 6. HER performance of PdPtFeCoNi HEA nanostructures.

Catalysts	**η at -10 mA cm^{-2}**	**η at -10 mA cm^{-2} after 10K**	**Tafel slope**	**ECSA**
PdPtFeCoNi HEA NSs	14 mV	23 mV	32 mV dec^{-1}	52.91 m^2 g^{-1}
PdPtFeCoNi HEA NWs	26 mV	40 mV	80 mV dec^{-1}	46.54 m^2 g^{-1}
PdPtFeCoNi HEA NPs	76 mV	279 mV	79 mV dec^{-1}	20.53 m^2 g^{-1}
Pt/C	60 mV	124 mV	55 mV dec^{-1}	47.56 m^2 g^{-1}

The PdPtFeCoNi HEA NWs were evaluated to determine the influence of nanowire thickness on the HER catalytic activity. LSV curves for different concentrations of D-glucose are shown in Figure 14. An increase in the concentration of glucose led to an increase in the thickness of the nanowires; as a result, it was observed that increased thickness resulted in lower activity. Notably, a lower concentration of D-glucose, which produced nanowires with smaller thickness, exhibited higher activity compared to higher concentrations (Table 5). Smaller-thickness nanowires generally offer higher surface area-to-volume ratios, which increases the availability of active sites for the hydrogen evolution reaction. This increase in accessible active sites per unit mass enhances the overall catalytic efficiency, as more areas are available for the reaction to occur. Additionally, thinner nanowires can potentially offer better electronic conductivity and shorter paths for electron transport, reducing the overall resistance and enhancing the electrocatalytic activity. These factors are crucial in electrocatalytic applications like HER, where rapid and efficient electron transfer is essential for high-performance catalysis.

Furthermore, the HER performance of PdPtFeCoNi HEA NSs and PdPtFeCoNi HEA NWs was compared with that of PdPtFeCoNi HEA NPs to evaluate their morphological features. The LSV curve, shown in Figure 15, indicates that the PdPtFeCoNi HEA NSs and PdPtFeCoNi HEA NWs exhibit higher catalytic activity than the PdPtFeCoNi HEA NPs. The overpotential at 10 mA cm^-2 for PdPtFeCoNi HEA NSs is lower (14 mV) than that of PdPtFeCoNi HEA NWs (26 mV), PdPtFeCoNi HEA NPs (76 mV), and Pt/C (47 mV). The Tafel slopes for PdPtFeCoNi HEA NSs, PdPtFeCoNi HEA NWs, PdPtFeCoNi HEA NPs, and Pt/C are 32, 80, 79, and 55 mV dec^-1, respectively (Figure 15b). These results clearly demonstrate the critical role of nanostructure morphology in influencing the electrocatalytic properties of the materials.

In addition, electrochemical impedance spectroscopy (EIS) measurements provided further insights into the intrinsic kinetic properties of these catalysts. Notably, the Nyquist plots for PdPtFeCoNi HEA NSs and PdPtFeCoNi HEA NWs showed smaller semicircles compared to those of PdPtFeCoNi HEA NPs and commercial Pt/C catalysts, indicating lower charge-transfer resistances (R_ct) during the HER process (Figure 11d). This reduction in R_ct suggests more efficient electron transfer processes at the interface between the electrode and the electrolyte, which is crucial for enhancing HER performance. Moreover, CV measurements of PdPtFeCoNi HEA nanostructures were obtained to calculate the electrochemically active surface area (ECSA). The ECSAs for PdPtFeCoNi HEA NSs, PdPtFeCoNi HEA NWs, PdPtFeCoNi HEA NPs, and Pt/C are 52.91, 46.54, 20.53, and 47.56 m^2 g^{-1}, respectively. A higher ECSA for PdPtFeCoNi HEA NSs was attributed to the morphological benefits of nanosheets, which, possessing a larger surface area and high-entropy composition, can provide abundant active sites compared to their counterparts. Furthermore, the stability of PdPtFeCoNi HEA nanostructures was measured by an accelerated durability test (ADT) of CV up to 10,000 cycles in 1.0 M KOH (Figure 16). As shown in Figure 16a, the stability of the PdPtFeCoNi HEA NSs after 10,000 cycles remained unchanged. Conversely, the HER performance of PdPtFeCoNi HEA NWs, PdPtFeCoNi HEA NPs, and Pt/C decreased. The overpotentials at 10 mA cm^{-2} after the ADT for PdPtFeCoNi HEA NSs, PdPtFeCoNi HEA NWs, PdPtFeCoNi HEA NPs, and Pt/C were 23, 40, 279, and 124 mV, respectively. Based on these results, the catalytic activity of PdPtFeCoNi HEA NSs was remarkable compared to the other PdPtFeCoNi HEA nanostructures. These findings underscore the potential of PdPtFeCoNi HEA NSs as highly stable and efficient catalysts for hydrogen evolution reaction applications.

The superior performance of HEA NSs and NWs can be attributed to several key factors inherent to their morphology and surface properties. i) Increased Active Surface Area: The extended surface areas of NSs and NWs provide more active sites for the HER. Unlike NPs, which typically expose a limited surface area to the reactant, the flat, wide surfaces of NSs and the elongated surfaces of NWs increase the accessibility of catalytically active sites. ii) Optimized Hydrogen Adsorption: The morphology of NSs and NWs may facilitate more favorable hydrogen adsorption-desorption dynamics, which are critical steps in the HER process. The specific crystal facets exposed by these morphologies might possess optimal binding energies for hydrogen atoms, thereby enhancing the overall reaction kinetics. iii) Enhanced Mass Transport: The unique structures of NSs and NWs could potentially offer lower diffusional barriers to reactants and products, streamlining the transport processes at the electrode-electrolyte interface. This feature is particularly advantageous in dynamic electrochemical environments like those encountered in HER. iv) Structural Stability: The robust crystalline structures of NSs and NWs may confer better stability under operational conditions, resisting morphological degradation that can plague nanoparticles, thus maintaining catalytic activity over longer durations. Based on the results, the morphology of PdPtFeCoNi HEA significantly impacts their catalytic performance in HER. Nanosheets and nanowires provided large active surfaces and favorable structural characteristics, outperform conventional nanoparticulate forms and even established catalysts like Pt/C. This study underscores the importance of nanoengineering in the development of efficient and durable electrocatalysts for sustainable energy applications, particularly in hydrogen production.

5.4 Conclusion

In conclusion, the study successfully synthesized and characterized PdPtFeCoNi HEA nanostructures (NSs, NWs, and NPs) using a facile one-pot synthetic strategy. The morphological differences were achieved through variations in chemical reagents such as metal precursors, reductants, surfactants, and shape-directing agents. These nanostructures displayed distinct morphologies and crystalline structures confirmed by HR-TEM, HR-TEM-EDS, and XRD. The nanostructures were then evaluated for their electrochemical performance in HER, where NSs and NWs exhibited significantly superior catalytic activity compared to NPs due to their increased active surface area, favorable hydrogen adsorption-desorption dynamics, enhanced mass transport, and structural stability. These findings highlight the critical influence of nanostructure morphology on catalytic performance and emphasize the importance of tailored synthetic strategies for developing advanced catalytic materials for sustainable energy applications.

5.5 References

1. Ren, J. T.; Chen, L.; Wang, H. Y.; Yuan, Z. Y. *Chem Soc Rev* **2023,** 52, (23), 8319-8373.

2. Raj, G.; Nandan, R.; Kumar, K.; Gorle, D. B.; Mallya, A. B.; Osman, S. M.; Na, J.; Yamauchi, Y.; Nanda, K. K. *Mater Horiz* **2023,** 10, (11), 5032-5044.

3. Tomboc, G. M.; Kwon, T.; Joo, J.; Lee, K. *Journal of Materials Chemistry A* **2020,** 8, (30), 14844-14862.

4. Chida, Y.; Tomimori, T.; Ebata, T.; Taguchi, N.; Ioroi, T.; Hayashi, K.; Todoroki, N.; Wadayama, T. *Nat Commun* **2023,** 14, (1), 4492.

5. Luo, W.; Wang, Y.; Luo, L.; Gong, S.; Li, Y.; Gan, X. *Applied Surface Science* **2022,** 606, 154808.

6. Yamabe-Mitarai, Y.; Yanao, K.; Toda, Y.; Ohnuma, I.; Matsunaga, T. *Journal of Alloys and Compounds* **2022,** 911, 164849.

7. Tracy, C. L.; Park, S.; Rittman, D. R.; Zinkle, S. J.; Bei, H.; Lang, M.; Ewing, R. C.; Mao, W. L. *Nat Commun* **2017,** 8, 15634.

8. Chen, W.; Hilhorst, A.; Bokas, G.; Gorsse, S.; Jacques, P. J.; Hautier, G. *Nat Commun* **2023,** 14, (1), 2856.

9. George, E. P.; Raabe, D.; Ritchie, R. O. *Nature Reviews Materials* **2019,** 4, (8), 515-534.

10. Liu, J.; Lee, C.; Hu, Y.; Liang, Z.; Ji, R.; Soo, X. Y. D.; Zhu, Q.; Yan, Q. *SmartMat* **2023,** 4, (4), e1210.

11. Yang, X.; Guo, R.; Cai, R.; Ouyang, Y.; Yang, P.; Xiao, J. *International Journal of Hydrogen Energy* **2022,** 47, (28), 13561-13578.

12. Al Zoubi, W.; Putri, R. A. K.; Abukhadra, M. R.; Ko, Y. G. *Nano Energy* **2023,** 110, 108362.

13. An, K.; Somorjai, G. A. *ChemCatChem* **2012,** 4, (10), 1512-1524.

14. Kim, Y.; Lee, Y. W.; Lee, S.; Gong, J.; Lee, H. S.; Han, S. W. *ACS Appl Mater Interfaces* **2021,** 13, (38), 45538-45546.

15. Yang, Y.; Liu, J.; Fu, Z. W.; Qin, D. *J Am Chem Soc* **2014,** 136, (23), 8153-8159.

16. Zhan, C.; Xu, Y.; Bu, L.; Zhu, H.; Feng, Y.; Yang, T.; Zhang, Y.; Yang, Z.; Huang, B.; Shao, Q.; Huang, X. *Nat Commun* **2021,** 12, (1), 6261.

17. Fu, X.; Zhang, J.; Zhan, S.; Xia, F.; Wang, C.; Ma, D.; Yue, Q.; Wu, J.; Kang, Y. *ACS Catalysis* **2022,** 12, (19), 11955-11959.

18. Li, M.; Huang, C.; Yang, H.; Wang, Y.; Song, X.; Cheng, T.; Jiang, J.; Lu, Y.; Liu, M.; Yuan, Q.; Ye, Z.; Hu, Z.; Huang, H. *ACS Nano* **2023,** 17, (14), 13659-13671.

19. Sun, Y.; Zhang, W.; Zhang, Q.; Li, Y.; Gu, L.; Guo, S. *Matter* **2023,** 6, (1), 193-205.

20. Ling, X.; Ao, Y.; Zheng, J.; Han, M.; Xu, D. *Chempluschem* **2024**, e202400010.

21. Sun, Y.; Huang, L.; Shan, Q.; Li, G.; Zheng, Z.; Jiang, Q.; Jiang, Y.; Xie, Z. *ACS Applied Energy Materials* **2022,** 5, (9), 10907-10914.

22. Hu, M.; Li, J.; Wu, Z.; Du, Y. *Surfaces and Interfaces* **2024,** 44, 103755.

23. Ao, Y.; Ling, X.; Zheng, J.; Han, M.; Xu, D. *Surfaces and Interfaces* **2024,** 45, 103928.

24. Li, J.; Wang, C.; Zhang, Y.; Hata, S.; Zhang, K.; Ye, C.; Shiraishi, Y.; Du, Y. *Journal of Energy Chemistry* **2023,** 85, 430-438.

Acknowledgement

Pursuing a Ph.D. degree and writing a dissertation is not just an individual experience, and it's not just one significant achievement for myself. In this regard, I would like to express my gratitude to the people who have assisted me throughout this study process.

First and foremost, I extend my heartfelt gratitude to Professor Jong Wook Hong, my supervisor. I am profoundly appreciative of the opportunity to participate in the Ms-PhD program in the Energy Nanomaterials lab. His kindness, patience, motivation, and support have been invaluable throughout my education. He expertly guided me through my graduate studies and shared in the excitement during my tenure at the University of Ulsan. Without his mentorship and guidance, completing this dissertation would not have been possible.

I also wish to sincerely thank the members of my dissertation committee: Professor Min Hyung Lee, Professor Jaehoon Jung, Professor Dongho Lee, and Professor Seok Min Yoon. Their continual suggestions, comments, reviews, and the enriching discussions greatly aided the development of this dissertation.

Additionally, I am grateful to Professor Ivandini Tribidasari A. for her assistance in securing a PhD scholarship at the University of Ulsan and for her enduring support and guidance during my time in the Department of Chemistry at Universitas Indonesia.

My thanks also go to my colleagues at the Energy Nanomaterial Lab—Ghufran Aulia, Hafida, Kevin, Ji Eun, Mitha, and Su Bin. Their support and collaboration made the lab a delightful and dynamic environment.

Lastly, but most importantly, I must acknowledge my family. My mother, Rubiyah, my brother, Eko Widodo, my husband, Adji Baskoro Dwi Nugroho, and my uncle, Widi Basuki, have all provided unwavering prayers, attention, motivation, and support, enabling me to complete this dissertation. Without their profound support, I would not have been able to stand as strong on my own.